ACTUATING SURFACE ATTACHED POSTS AS SENSORS FOR MICROFLUIDIC APPLICATIONS

Robert Judith

A dissertation submitted to the faculty at the University of North Carolina at Chapel Hill in partial fulfillment of the requirements for the degree of Doctor of Philosophy in the Department of Physics.

Chapel Hill
2016

Approved by:

Richard Superfine

Michael Falvo

Chris Clemens

Roberto Camassa

Steve Soper

ABSTRACT

Robert Judith: ACTUATING SURFACE ATTACHED POSTS AS SENSORS FOR MICROFLUIDIC APPLICATIONS
(Under the direction of Richard Superfine)

Cilia are hair-like projections from cells that act as sensors and micro-actuators. They are around 250 nm in diameter and range in length from a few microns to hundreds of microns and beat in complex shapes to generate fluid flow. Cilia are found across the entire eukaryotic tree, essentially unchanged, suggesting that they are extremely efficient fluid flow generators and sensors. At this micro scale fluids behave differently, viscous forces and surface tension become dominant, and gravity and inertial forces become minor forces. Biomimetic actuators that mimic biological cilia have been developed to act as pumps, mixers, and potentially sensors at the micron scale for applications in microfluidics. This dissertation focuses on understanding how these micro-actuators operate. I begin with trying to understand how biological cilia function. I will show experimental results demonstrating that the structural elements of the cilium, microtubules, are highly curved when isolated from the axoneme and that this curvature is protein dependent. I will then propose a new model for cilia actuation that takes this curvature into account, and show that it could account for some of the missing force in the cilium. In the rest of the dissertation, I focus on developing a model for describing the motion of biomimetic nickel poly-dimethylsiloxane (PDMS) composite actuating surface attached post arrays (ASAP) that were developed previously in our lab. This model of the ASAP arrays takes into account the magnetics, the transmitted light by the array, and the post fluid structure interaction. In the last sections of the dissertation, I will demonstrate that the model can be used to describe the post motion in viscous fluids and blood clots, which allows the biomimetic ASAP arrays to be used as sensors. The results of this dissertation shows that ASAP arrays have the potential to be effective sensors along as well as pumps and mixers in micro-fluidic systems.

ACKNOWLEDGEMENTS

A PhD dissertation is a long journey that can not be undertaken alone. Before diving into my dissertation, I would like to take a moment and thank all the people that have helped me along the way.

I would like to start with my advisors Richard Superfine and Michael Falvo. Both of their support and advice helped me get through the more challenging times of my graduate career. I would also like to thank Sean Washburn, for his help with data analysis and teaching me to think on my feet while giving a talk. Russel Taylor, for all his help with software and analysis. He is truly a computer wizard and the lab is poorer without him.

Next, I would also like to thank all my lab mates: Jeremy, Jerome, Jo, Kellie, Suzy, Nadira, Bethany, Briana, Luke and anyone else that I forgot to list here. Not only were you always a source of advice, support and encouragement but you made the lab a home. I will always be grateful to you all for making my time in the lab so enjoyable.

Last, I would like to thank my friends and family, who have supported me non-stop throughout my life. Out of my friends, I want to thank Ricky O'Steen and Scott Schrieber for letting me vent during the hard times and keeping me sane. I would like to thank my mom, dad, and sister for all their support through the years, especially my mom, who home-schooled me for the first 8-9 years of my education. And finally I would like to thank Megan, my wife. We survived graduate school together. You make the hard times okay and the good times great. I love you.

TABLE OF CONTENTS

LIST OF FIGURES

LIST OF ABBREVIATIONS AND SYMBOLS

α	Normalized Length
χ_a	Magnetic Susceptibility
$\dot{\gamma}$	Shear
η	Viscosity
γ	Drag Term
μ_0	Permeability of Free Space
ν	Poisson Ratio
ω	Angular Frequency
ϕ	Angle Correction for Intensity
ϕ	Magnetic Field Angle
ψ	Magnetic Moment Angle
ρ	Density
σ	Surface Stress
τ	Torque
a	Nickel Length
A	Occluded Area From a Post
B	Magnetic Flux Strength
b	Nickel Diameter
b	Post Diameter
C	Contrast Ratio Between the Nickel and PDMS
D	Post Diameter
D_{ni}	Nickel Drag

E	Elastic Modulus
e	Magnetic Potential Energy
F	Force
f	Frequency
H	Magnetic Field Strength
h	Post Hieght
I	Second Moment of Inertia
I	Transmitted Intensity
I_{ax}	Second Moment of Inertia for Axoneme
I_{db}	Second Moment of Inertia for a MTD
I_{off}	Transmitted Intensity with Magnets Off
I_{on}	Transmitted Intensity with Magnets On
L	Length of ASAP Post
L_{ni}	Nickel Portion Length
L_{PDMS}	PDMS Portion Length
L_t	Total Post Length
M	Magnetic Moment or Applied Moment
M	Moment
M_{ax}	Moment Over the Entire Axoneme
M_{dm}	Moment Across an MTD
m_s	Saturation moment
N	Number of Posts in a Field of View
$n_{x,y,z}$	Demagnetization Factors

R_c	Radius of Curvature
Re	Reynolds Number
s	Arc Length
s	Average Post Spacing
S	Shear Force
Sp	Sperm Number
t	Thickness
T	Torque
u	Fluid Velocity
v	Nickel Volume
v	Poisson Ratio
v	Velocity
w	Post Deflection
w	Width
W	Work of Adhesion
$\|H\|_{sat}$	Saturation Magnetic Field
AFM	Atomic Force Microscopy
ALI	Air Liquid Interface
ASAP	Actuated Surface Attached Posts
ATP	Adenosine Triphosphate
BDF	Backward Differentiation Formula
HBE	Human Bronchial Epithelial Cell
IDA	Inner Dynein Arm

LED	Light Emitting Diode
MEMS	Microelectromechanical Systems
MTD	Microtubule Doublet
ODA	Outer Dynein Arm
PBS	Phosphate Buffered Saline
PCTE	Poly-carbonate Track Etched
PDMS	Poly-dimethylsiloxane
RS	Radial Spoke
SEM	Scanning Electron Microscope
TEG	Thromboelastography
TEM	Transmission Electron Microscope
VHA	Viscoelastic Hemostatic Assay

CHAPTER 1: Introduction

The micro scale world is a fascinating and fundamentally different place. It is a world where our every day intuition of physics and motion breaks down. Gravity and inertia, which dominate our everyday life, become only minor forces and forces that are merely corrections or even non apparent. At the macro scale drag forces and surface effects dominate.

This dissertation is about a specific class micro-actuators in fluids at this small scale. These actuators, whether they are biological (cilia) or man-made (actuating surface attached post arrays (ASAP)), are slender filaments, roughly the aspect ratio of a yard stick, that beat to generate fluid flow. At this scale, the fluid flow generated by these micro-actuators is very different than flow at the macro scale. Inertial forces are nearly non existent and forces are in the quasi-static regime making it impossible for symmetrical motion to generate fluid flow or enable a micro-scaled swimmer to swim. Purcell in his famous talk on swimming at the micro-scale called this phenomena the scallop theorem (132). To generate fluid flow or swim, the motion of the actuator must be non-symmetric in time. This can be done by actively driving the beat in a non-symmetrical manner or by taking advantage of the interaction between the elastic forces of the actuator and the fluid drag on the actuator. It turns out that this ratio of the internal elastic forces to the viscous drag forces in the actuator determines how these micro actuators function (Chapter 4).

Cilia are conserved across the entire eukaryotic tree, which suggests that cilia are optimized micro-actuators. These hair-like projections from eukaryotic cells are roughly 250 nm in diameter and are between a few microns (human airway cilia) (141) to hundreds of microns (sea urchin sperm) in length (69). They come in two varieties: passive cilia act as sensors to their local mechanical and chemical environment, and active cilia beat in complex patterns to generate fluid flow in addition to their sensing functions. Every active cilia contains thousands of molecular motors that coordinate to drive the cilium and generate their complex beat shapes. These beat shapes enable single-celled organisms to swim (e.g, *Chlamydomonas* or sperm), and generate fluid flow (e.g, mucus clearance.) As a complex molecular machine on the micro scale the cilium is unequaled.

Section 1.1: Artificial micro-actuators and microfluidics

Biological cilia are an inspiration for man made actuators at the micron scale, (46; Fiser et al.; 168). Biomimetic cilia are arrays of slender rods or flaps that are driven by an external force, electrostatic, magnetic,

optical, etc. These biomimetic cilia have applications in micro-fluidics that also operate at at the micron scale (184).

In many cases, the features of fluid flow on the micro-scale are desirable and have lead to new technologies such as extremely accurate chemical gradients for cell culture (186; 195), or rheometers that match the pressure across multiple fluids in laminar flow (29); however, these features can also pose challenges. Because of laminar flow, mixing becomes extremely difficult at the micro scale (122; 184) and pumps that can be integrated into these small devices are often complex and difficult to create (145). Biomimetic cilia systems have the potential to address these problems.

Many novel and efficient solutions to engineering problems have been discovered by studying nature. The classic example of biomimicry is the development of velcro, which was inspired by burrs plants attaching to fur and clothing. More recent examples include super-hydrophobic surfaces based off of the lotus leaf micro structure (179), microscopic air flow sensors that mimic cricket hairs (87), or shatter resistant glass (113). In nature, cilia are efficient pumps and mixers. Cilia clear mucus and particulates out of the lung, generate the fluid flow responsible for left right asymmetry in the embryo (140), and help micro-organisms overcome the diffusion limit for feeding by enhancing mass transport (149). Biomimetic cilia have already been shown to be effective pumps and mixers (168; 151; 169).

Section 1.2: Overview of the thesis

This thesis is about both understanding how biological cilia function and how we can use biomimetic cilia arrays as sensors. In Chapter 2, I will focus on biological cilia. I will describe the biological cilium structure, the current theories of how it operates, and present experimental results demonstrating that the structural elements of the cilium (microtubule doublets) are curved and this curvature is dependent on protein binding. I will then present a new model of how the cilium actuates that incorporates this curvature and shows that this new model is complementary to the current models.

The rest of the thesis will focus on biomimetic actuating surface attached posts (ASAP). In Chapter 3, I will describe the biomimetic cilia arrays that our lab has developed as well as the manufacturing process. In chapter 4, I will develop a comprehensive mathematical model of the ASAP system. The model will include a model of how the transmitted intensity relates to the post deflection, the magnetic response of the post arrays, and the fluid structure interactions. The fluid structure model will ultimately depend heavily on a dimensionless parameter called the sperm-number, which came about from studying biological systems and is named after sperm cilia (189; 91).

In the last two chapters, 5 and 6, I will focus on using the posts as sensors for two different applications.

These chapters will use the model developed in chapter 4 to calculate the material properties of fluids by monitoring the post response under a known drive signal. In chapter 5, I will confirm the model developed in chapter 4 by using the posts as a rheometer for Newtonian fluids. In chapter 6, I show that the posts can also be used as an elastomer to measure the elasticity of blood clots as they form. I will show that the ASAP system correlates well with a commercial thromboelastographer (TEG) for identifying dilutional coagulopathy, which is relevant for trauma victims.

CHAPTER 2: The biological cilium

Section 2.1: Introduction

Cilia are hair-like projections from cells that act as sensors and beat to produce fluid flow. Found in all forms of eukaryotic cells, from single celled organisms to humans, cilia are one of nature's most amazing and complex molecular machines. Each cilium is a complex structure with thousands of molecular motors that coordinate to produce complex beat patterns. The current theory is that there is a single mechanism to provide bending. The molecular motors generate shear stress between the structural elements causing bending. =I will show that the structural elements of the cilium, i.e. the microtubule doublets (MTD), are significantly curved, 0.8 $1/\ \mu m$ radius, compared to the curvature seen in the beats, 0.5 $1/\ \mu m$ radius (147), when isolated from the cilium, and that this curvature depends on protein binding. The protein attachments to the MTDs are dynamic over a single beat which suggests the bending observed in isolated MTD could also be dynamic. I will show that this new model of producing curvature in the cilium can generate forces on the correct scale to bend the cilium, and that the forces are complementary to the forces that the motors produce.

Section 2.2: Overview of cilia in biology

Cilia are slender, hair-like organelles that project from eukaryotic cells, pictured in scanning electron microscope (SEM) images in Figure 2.1 (114; 141). They are roughly 200 nm in diameter and range in length from a couple microns, for human airway cilia, to hundred of microns, for sea-urchin sperm. These cell projections perform two vital roles. First, they enable single-celled organisms to swim (e.g, *Chlamydomonas* or sperm) and multicellular organisms to generate internal fluid flows (e.g, mucus clearance). Second, they act as sensors for the cell's local chemical and mechanical environment (141). Cilia are found across all branches of the eukaryotic tree, and while they differ in length between species, they all are composed of the same basic structure. This ubiquity suggests that cilia developed early in the eukaryotic tree, around one billion years ago (Figure 2.2). The fact that they have existed relatively unchanged for so long suggests they are well-suited solutions to the problems of generating fluid flows and sensing the local environment (114).

Cilia come in two varieties: passive cilia which act as sensors to the local environment, and active cilia which generate fluid motion. Passive cilia are both mechanically sensitive to stimuli and also contain protein

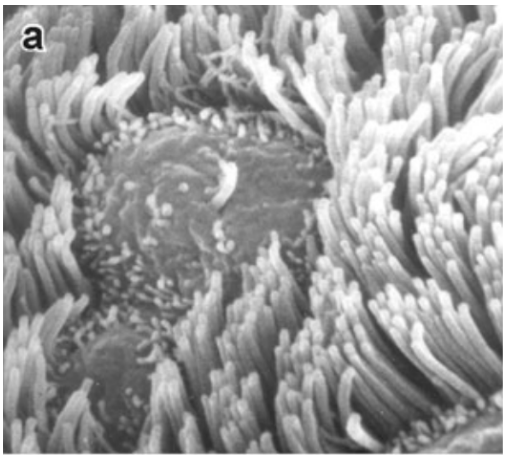

(a) Oviduct Cilia (141)

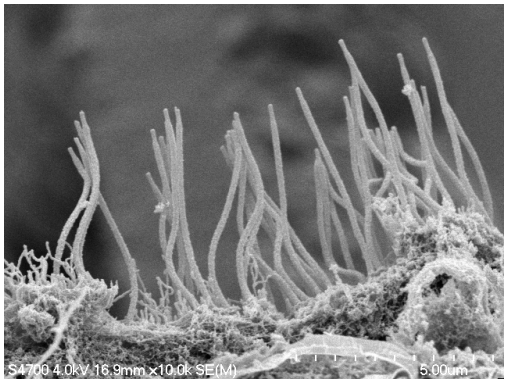

(b) Human Airway Cilia

Figure 2.1: SEM images of biological cilia. a) is a example of human oviduct cilia, which help transport the egg to the uterus. b) is an example of human airway cilia. In the airway cilia help transport mucus out of the lung and into the stomach for sterilization. (Image taken by Jerome Carpenter.)

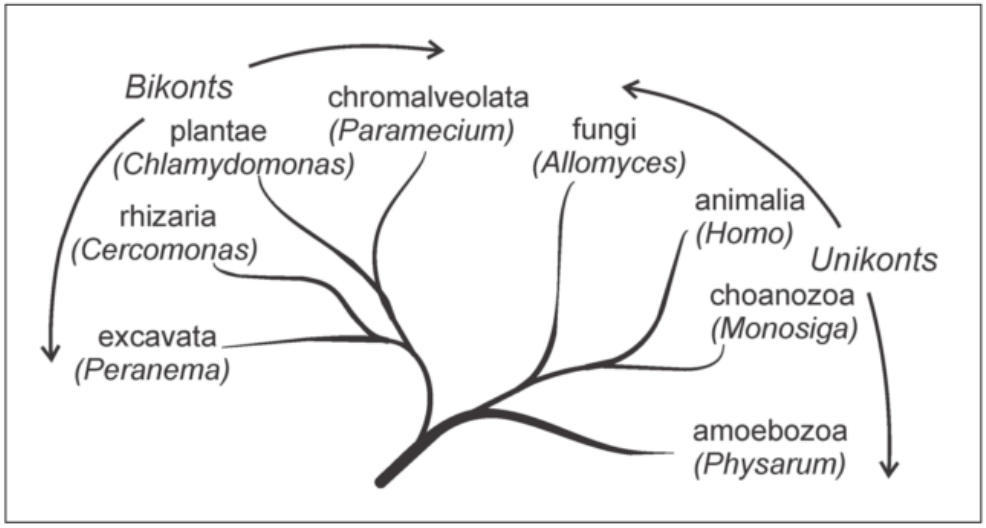

Figure 2.2: This diagram shows the two main branches of the eukaryotic tree: Bikonts and Unikonts. Motile cilia with the basic 9+2 microtubule structure are found across all branches indicating that cilia originated from a common ancestor at the beginning of the eukaryotic tree roughly a billion years ago. Source (114)

receptors in their membranes that allow them to sense chemicals in the surrounding environment (141). Active cilia —the focus of this chapter and referred to as cilia from now on— share passive cilia's sensing functionality but also oscillate and generate fluid flows in their respective environment (142; 114). These cilia beat in complex beat shapes depending on their role. Nodal cilia, formed in mammalian embryos, beat off axis in a circular beat pattern, sperm flagella beat in a helical pattern, and human airway cilia and *Chlamydomonas* cilia beat in a planar shape (100).

Mostly the initial understanding of how cilia function came from studying diseases caused by cilia defects. People with dysfunctional cilia, reduced mobility or immobile, develop the same set of problems, which are indicative of the important roles cilia perform in the body. Chronic infections in their mucous membranes can cause bronchitis or other respiratory diseases due to poor mucociliary clearance. Male patients are almost always infertile because their sperm are incapable of moving without functioning cilia, and female patients are often sub-fertile because cilia help transport eggs along the fallopian tubes (64). There are slight differences in brain structure that are thought to compensate for the lack of water propelling cilia in the brain (2; 141). By studying transmission electron microscopy (TEM) images of cilia from people with defective cilia, the initial understanding of the cilium as a molecular machine was developed.

Section 2.3: The cilium is a complex molecular machine

All cilia have the same basic underlying structure across the entire eukaryotic tree despite having varying beat shapes and functions (55; 66). Cilia have nine microtubule doublets (MTDs) arranged in a 220 nm diameter ring (124; 125). These MTDs are structures unique to the cilium. Each MTD consists of a complete circular microtubule, called the A tubule, connected to an incomplete slightly larger microtubule, the B tubule (163), Figure 2.3(b). A protein complex called the nexin link attaches each MTD to its neighbor (124; 55). Most cilia have an additional pair of singlet microtubules, known as the central pair, in their center. This structure of nine microtubule doublets plus a central pair is known as the basic 9+2 structure, Figure 2.3. Most passive cilia do not have the central microtubule pair and all active cilia missing the central pair beat helically (97). The central pair are connected to the nine outer MTDs through protein complexes called radial spokes (125; 124). Finally, cilia have thousands of dyneins (molecular motors) between the outer MTDs, which according to the accepted model generate the force that bends the cilium. The pattern of proteins repeats every 96 nm along the cilium length, and is known as the 96 nm repeat (Figure 2.4) (125). The entire structure of proteins, without the membrane, is called the axoneme. Not all species have the same number or type of proteins in the 96 nm repeat. Human cilia, for example have, a single radial spoke per MTD per 96 nm repeat while *Chlamydomonas* has two radial spokes (130), see Figure 2.4.

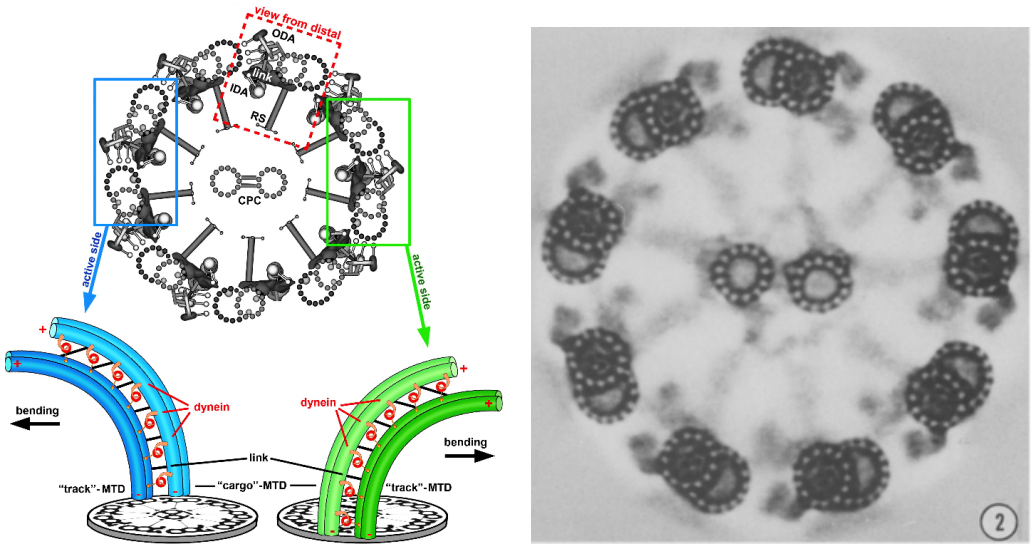

(a) Cilia Diagram (66)

(b) TEM Cross-section

Figure 2.3: a) Diagram of cilia. Top section shows a cross section of the cilia axoneme. The 9 microtubule doublets circle around the central pair of singlet microtubules. The outer microtubule doublets are connected to the central pair by a protein complex known as the radial spokes, labeled RS. Dynein motors are attached to one microtubule doublet and walk along their nearest neighbor. The dyneins are labeled IDA the inner dyneins, and ODA for the outer dyneins. The sub-figure below shows how dynein motors cause bending in the axoneme by generating a sliding motion between the microtubule doublets. Because the doublets are fixed at the base the sliding motion in converted into curvature.(66) b) TEM cross-section of a cilium. The protein structures diagram in (a) can be seen in the TEM.

Each dynein complex consists of an arm, which permanently attaches to the A tubule in the MTDs, a motor domain, which generates the motion, and a stalk and binding domain, which connects transiently to the neighboring MTD. Each dynein arm will have one or more motor domains, which hydrolyze adenosine triphosphate (ATP) and generate movement (125) (84; 72; 154; 23). Axonemal dynein is arranged in two rows along the A microtubule of the MTD, an inner row and an outer row. Outer dynein arms are thought to control the beat frequency and are all the same (61; 125). Inner dynein arms have multiple varieties in the same organism, which repeat with the 96 nm repeat (125). The inner dynein arms are currently thought to be critical for the beat shape (61; 100).

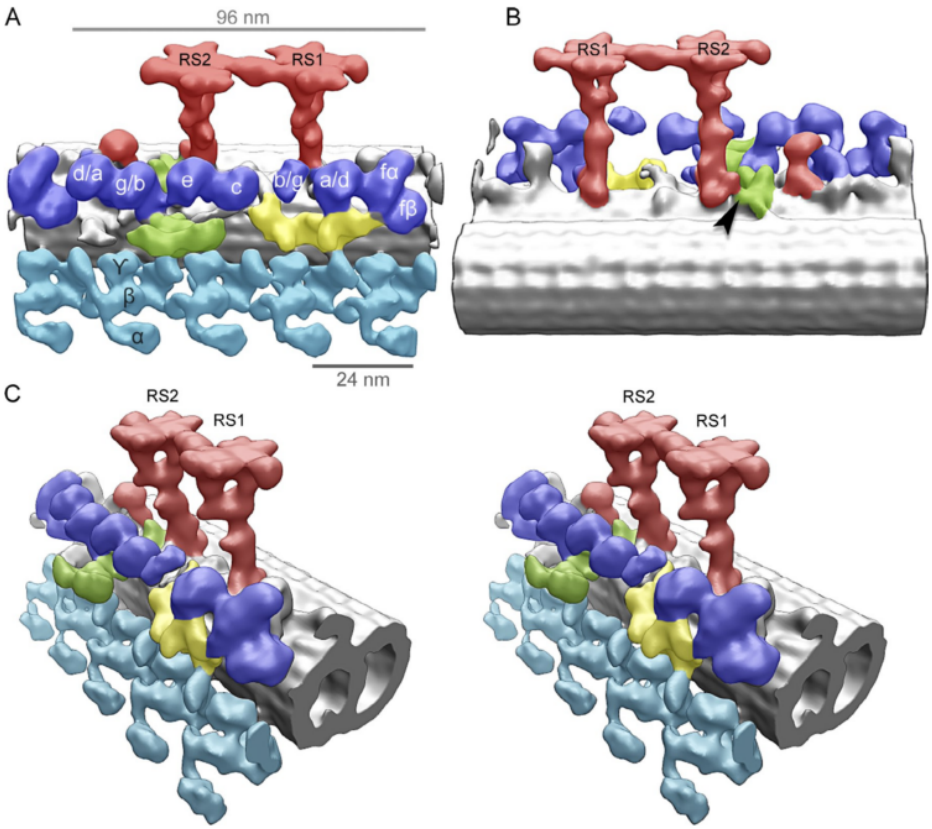

Figure 2.4: Four views of the 96 nm repeat. The 3D surface was created using cryoelectron tomography of *Chlamydomonas* axonemes. The radial spokes are shown in red, the inner dynein arms are shown in dark blue, the outer dynein arms are shown in light blue, and the MTD is shown in gray. Human cilia have only a single radial spoke per 96 nm repeat, while the *Chlamydomonas* axoneme shown here has two radial spokes. Reproduced from (130).

Section 2.4: Actuation theories

The currently accepted curvature mechanism in the axoneme is the sliding theory of curvature proposed by Peter Satir in 1965 (139). Gibbons performed experiments that confirmed the sliding of microtubules in

cilia where the axonemes were partially digested with trypsin, Figure 7 (164). Trypsin is an enzyme that cleaves proteins and preferentially digests the radial spokes and nexin links in the axoneme (164). These partially-digested axonemes were exposed to ATP, activating the dynein motors. Gibbons and Summers found that, in these damaged cilia, MTDs slid past one another and the axoneme disintegrated, Figure 2.5. This has been a key piece of evidence for the sliding theory of curvature. In the axoneme, all microtubules are oriented with their minus ends located at the base of the cilium. Dynein motors are minus directed motors, which always generate force towards the minus end of the microtubule. In the axoneme, this causes microtubules to slide towards the base of the cilium. This motion causes the axoneme to slide apart in damaged axonemes, Figure 2.5, but in an intact axoneme the nexin links, radial spokes, and basal body all prevent the sliding motion and convert it into bending, Figure 2.3. In order to generate a consistent beat pattern, dynein motors on opposite sides of the cilium must coordinate. During the power stroke, dynein motors on one side of the cilium must be active, while on the opposite side, the dyneins remain detached or in a sliding state. When the recovery stroke begins, the sides must switch roles. Therefore, according to sliding theory, only one side of the axoneme can generate force at a time. This model of ciliary function is known as the "switch point hypothesis" as it requires a point where the active and passive sides of the axoneme switch roles.

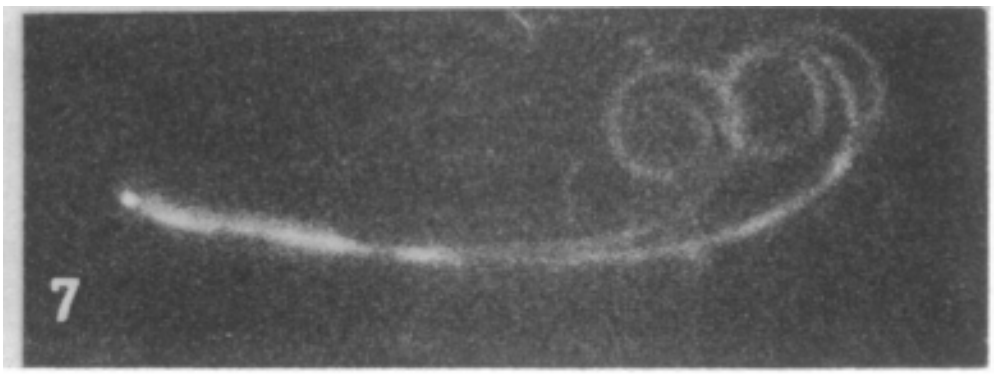

Figure 2.5: Dark field imaging of a cilia axoneme disintegrating after being treated with trypsin and being dosed with ATP. These original images established that dynein caused sliding in the axoneme and led to the original hypothesis that dynein causes bending by causing shear between the microtubule doublets. The radius of curvature in this image is very similar to the radius of curvature we measure using the AFM. (164)

How dynein motors coordinate so that only one side of the axoneme is active at a time is currently up for debate. The most popular theory is that local curvature of the microtubule doublets is sensed by the dyneins mechanically, and the curvature controls the dynein activity. This local curvature control method was proposed by Brokaw in the 1970s (18), who showed that if you input curvature dependent probability curves for the dynein activity into computer models you could get oscillations similar to actual cilia. Brokaw continued to expand his model to increasingly realistic simulation conditions, 3D, and multiple dynein types

(14; 15; 17; 16). Brokaw's postulated model of curvature control is entirely phenomenological: it assumes a relationship between dynein activity and the local MTD curvature. Lindemann developed a 't-force' model, which attempts to provide a mechanism to Brokaw's model. In Lindemann's model, as the axoneme bends, the cross-section of the axoneme distorts moving MTDs closer and further apart in the axoneme. Lindemann proposed that these transverse forces control the dynein activity, and showed in computer models that a 't-force' model is capable of simulating realistic cilia beats (98; 97). Both Brokaw and Lindemann cite experiments and previous calculations where inactive cilia can be activated by inducing a curvature as evidence for their theories (71).

However a less popular theory, has to do with the central pair. It has been observed in some organisms, such as *Chlamydomonas* and *Paramecium*, that the orientation of the central pair change over the cilia beat, (185; 126). This observation, combined with the fact that organisms with defects in the radial spokes do not have functioning cilia (92; 191), have led to the proposal that the central pair might act as a 'distributor' and control dynein activity (185; 126). It has also been suggested that the central pair might contribute to the asymmetric beat pattern by changing its stiffness over the course of a cilium's beat (7). One common theme among these models is that one side of the axoneme is active and has shear stress generated by active dyneins, while the other side is passive and has the dyneins either detached or sliding.

With only one side of the cilium generating force at a time, there has been considerable interest in the roll of twsting in the cilium's beat. Lindemann and Brokaw's early models ignore the possibility of twisting in the cilium and the asymmetric forces generated is not even calculated. This assumption is justified by experimental evidence that the structure does not twist (192), and early theoretical work that suggests that the twist due to the dynein motors is negligible (70). Later models included twisting and suggested that it plays a minor roll in the beat (16) Other models suggested that twisting plays a significant role in the cilium's beat (67), and the question of how much twisting plays a roll in the cilium is still up for debate.

There is also a question whether or not the dyneins can generate enough force to explain the beats currently seen. Experimental studies that measured the force found roughly 5-6 pN of force per dynein on the active side of the cilium in bull and human airway axonemes (143; 68). This number is within the measured range for the force generated from a single axonemal dynein head of $\tilde{6}$ pN (154). However this requires that all the dynein heads to be activated simultaneously (143), which runs counter to other experiments that suggest the outer dynein arm duty ratio is 0.1 or lower (148; 60). Schmitz and Lindemann even remarked at the end of their paper:

> "Moreover, we must insist that all of the dynein heads must contribute force, not just one per dynein arm. This runs counter to the conception that only a small fraction of the heads are

> active at a given time (Johnson, 1986; Hamasaki et al., 1995). However, if we do not accept this assertion, then we are left with the equally difficult proposition that the intact arms must be much more powerful than can be justified by the *in vitro* data on isolated dynein. These are surprising but unavoidable conclusions."

where they measured the forces generated by the cilia in a bull sperm (143).

In our own lab, we have measured the force generated by a single human airway cilia (68), and came to the same result that every single dynein head must be activated near their max force in order to match the experimental results. If dyneins operate as experiments suggests, with a duty ratio below 0.1 (148; 60) and a maximum force of $\tilde{6}$ pN (154), then there is an order of magnitude of force missing in the cilium.

Section 2.5: Microtubule mechanical properties

To calculate these forces, the mechanical properties of the MTDs are key components of the model. If our understanding of the MTD properties is wrong, then the force calculations will be wrong as well. Currently, the material properties of the MTDs are inferred from their geometry and the mechanical properties of singlet microtubules. The problem is that microtubule mechanical properties are known to vary depending on their measurement conditions and the presence of microtubule-associated proteins (63). The assumption that the microtubule doublets, which have numerous additional proteins, post-translational modifications, and a unique structure, will have similar mechanical properties to their singlet counterparts is not trivial (163; 41; 53).

Since the 1970s, it has be known that MTDs extruded from the axoneme curl up, Figure 2.5 (164). This curvature was of interest in the late 1970s and early 1980s, but interest has since wained (112; 165; 111; 199). It was even postulated that this curvature had something to do with the cilia beating, but this lost favor as the sliding model gained traction (32).

I will show that isolated MTDs from human airway cilia are inherently curved and that this curvature is dependent on protein binding even for single isolated microtubules. Because the sliding model cannot curve an isolated MTD, this suggests an alternative mechanism for curvature generation in the cilium.

2.5.1: Methods

To study the mechanical properties of MTDs. Cilia axonemes were harvested from Human Bronchial Epithelial cells, acquired from the UNC Cystic Fibrosis Center. Axonemes were then partially digested using trypsin and supplied ATP, similar to the Gibbons procedure, resulting in MTD sliding. After the sliding procedure, there are free MTDs in solution. MTDs were then either immediately mounted on substrates for

imaging or treated with a salt solution to remove the outer dynein arms (62). We performed atomic force microscopy (AFM) and transition electron microscopy (TEM) on the samples and analyzed the images for curvature. See Appendix 6.5, for a complete description of all the procedures.

2.5.2: Single MTDs show dynein dependent curvature

The cilia isolation procedure was confirmed with AFM images, Figure 2.6A. Protein determination on the resulting solution of axonemes determined that the protein concentrations were on the order of 50 $\mu g/mL$. AFM images of the MTDs from the isolated axoneme showed consistent curvature of $0.80 \pm .03 \quad 1/\mu m$ (Figure 2.6). TEM images of similarly prepared MTDs show that the dynein arms are on the outside of the curvature (Figure 2.7).

A silver staining gel of the salt-extracted axonemes show a near complete removal of the protein bands, corresponding to one of the outer dynein arm heavy chains (Figure 2.8). This chain binds the outer dynein arms permanently to the A microtubule in the MTD. Without this arm the dyneins cannot attach to the MTD. This heavy chain shows up in the solution's supernatant indicating that the outer dynein arms are removed as we believe (Figure 2.8). The fact that the band is completely missing from the axoneme solution in the silver staining gel confirms that a majority of the outer dynein arms are removed (62). MTDs that have undergone the salt treatment procedure show a reduction of curvature, and a broader distribution of curvatures. After salt extraction, a reduction in the average curvature is seen, $.20 \pm .01 \quad 1/\mu m$, as well as a broadening of the curvature distributions (Figure 2.6B,D).

Section 2.6: Protein-attachment model of microtubule curvature

As mentioned before this curvature is seen in the literature, Figure 2.5, and is consistently in the range of 0.5-0.9 $1/\mu m$. This value is remarkably similar to our value of $.80 \pm .03$ $1/\mu m$. Because removal of the outer dynein arms changes the microtubule curvature, i.e. straightens the MTDs, we propose that this curvature is caused by the asymmetric binding along the MTD. Proteins bound to the microtubule doublet could introduce curvature through multiple mechanisms, e.g steric interactions with their neighbors, electro-static interactions, protein deformation at the binding site (116).

We will use a thermodynamic surface stress model to investigate the plausibility of our hypothesis. This model is not unique but simply postulates that protein binding cause a change in the surface stress on microtubule surface. The surface stress difference between the inner and outer surfaces causes the microtubule doublet to bend, Figure 2.9.

This model has been used to understand how AFM cantilevers bend when proteins attach to a func-

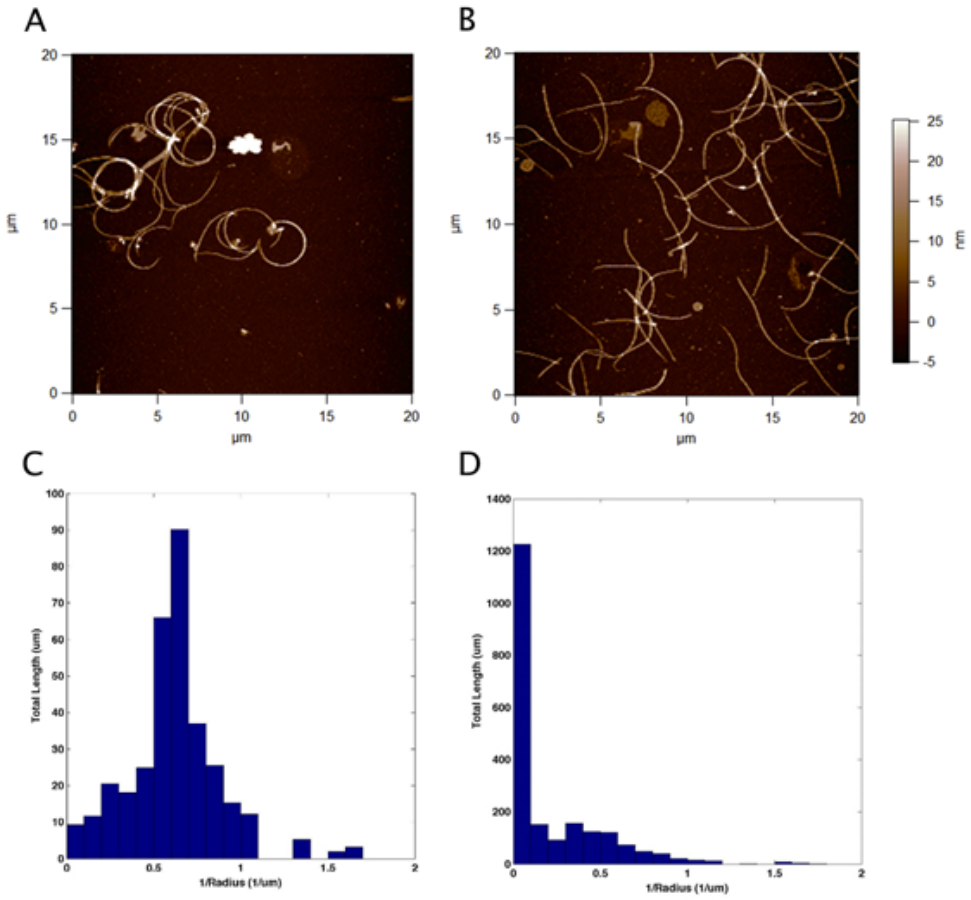

Figure 2.6: A) AFM image of frayed cilia axonemes. Images show that the microtubule doublets are curved. B) Image of frayed cilia axonemes, after salt treatment. Salt treatment removes the outer dynein arms from the cilia axonemes. C) Histogram of the radius of 1/Radius of curvature for the untreated doublets. D) Histogram of 1/Radius of the salt-treated axonemes. There is a shift to lower levels of curvature after the salt treatment.

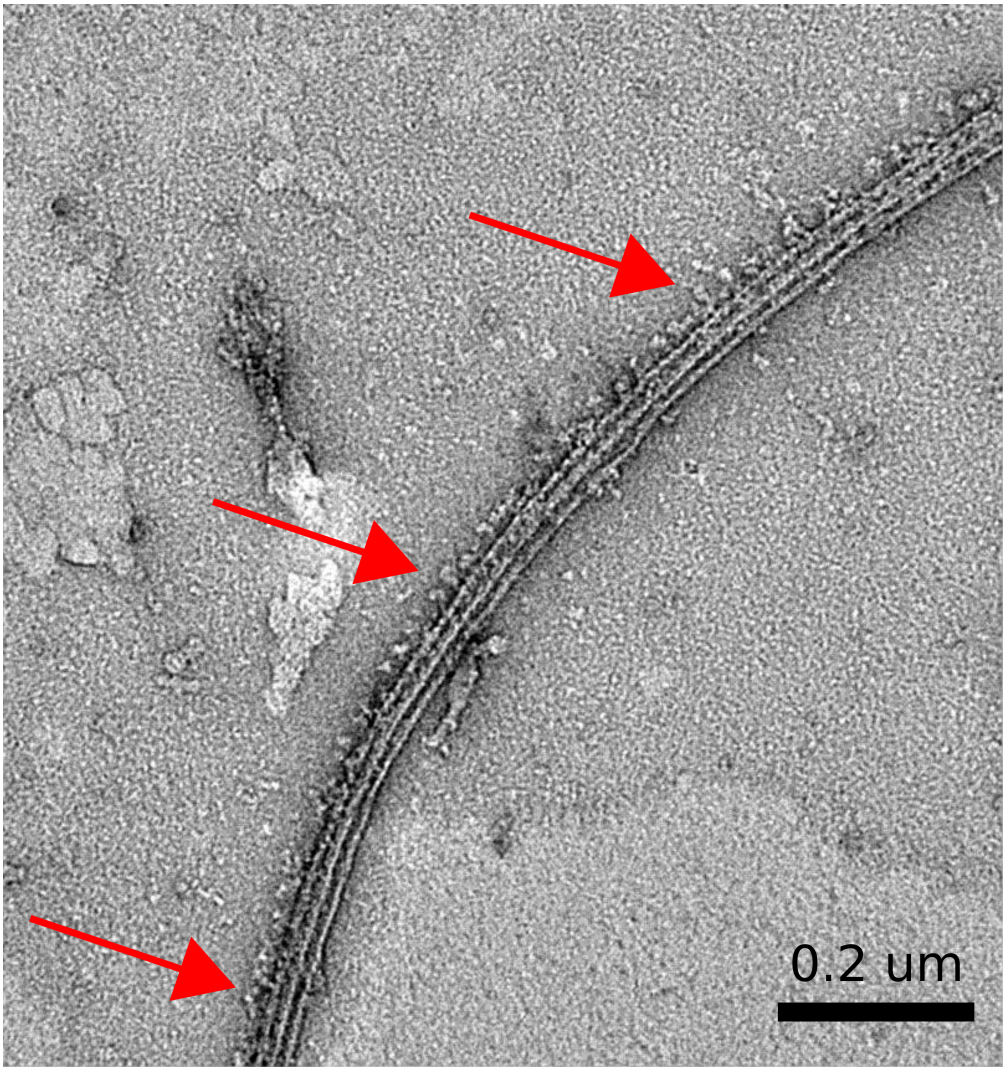

Figure 2.7: TEM image of a curved microtubule doublet. The dynein motors can clearly be seen along the outer edge of the MTD, labeled with the red arrow.

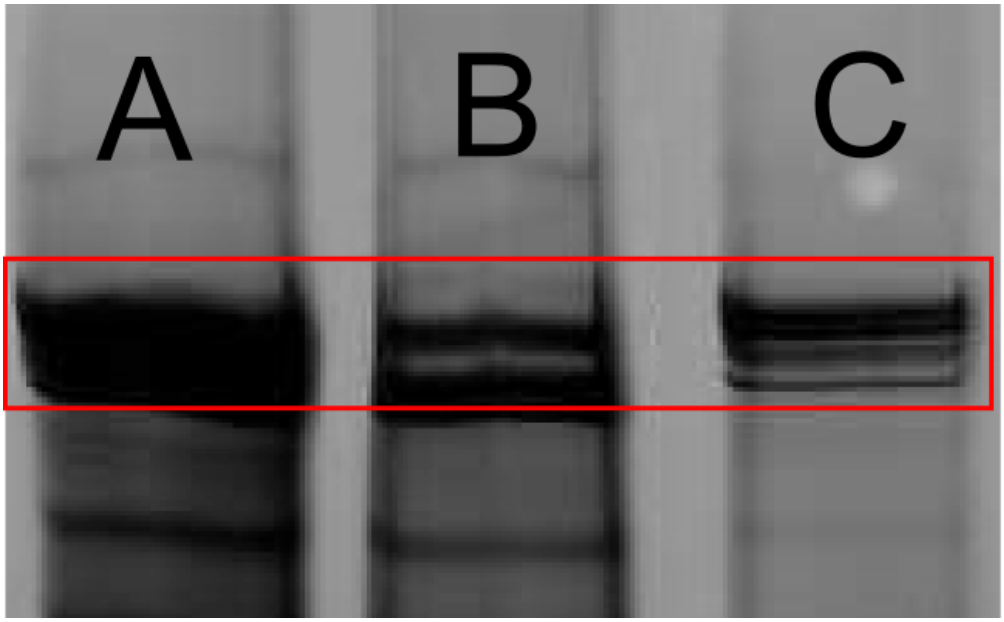

Figure 2.8: A silver staining gel, showing the proteins in the cilia axoneme, by molecular weight. The arrow points out the band representing the outer dynein arms. A) Solution containing the extracted axonemes. B) Axonemes after the salt extraction. The missing bands are from the extracted dynein outer arms. C) Supernatant from the salt extraction. The bands representing the dynein arms are present in the salt extraction as expected. Additional bands represent proteins that were removed unintentionally removed or faint remnants of axonemes.

tionalized surface, and it has been used to study surface stress affects due to thin films, electrochemical interactions, and biomolecules. (134; 117; 193; 161; 57) The ability of proteins to introduce a surface stress upon binding has been used as the basis for highly sensitive biosensors (57; 22; 116). These techniques calculate the change in surface stress by measuring the deflection of a cantilever. This deflection can be translated into a change in surface stress using the Stoney equation, eq 2.1 (4).

$$\Delta\sigma = \frac{Et^2}{6R_c} \tag{2.1}$$

where, $\Delta\sigma$ is the surface stress difference between the top and bottom of the cantilever, E is the elastic modulus, t is the thickness of the cantilever, R_c is the radius of curvature of the cantilever. Often with cantilevers, E is replaced with the biaxial modulus $E/(1-\nu)$, where ν is the Poisson ratio of the material which accounts for counter-bending that occurs in thin plates. Because we model the MTDs as beams, we will stick with the original form of the equation above, Figure 2.1, but we will need to generalize to non-rectangular cross sections.

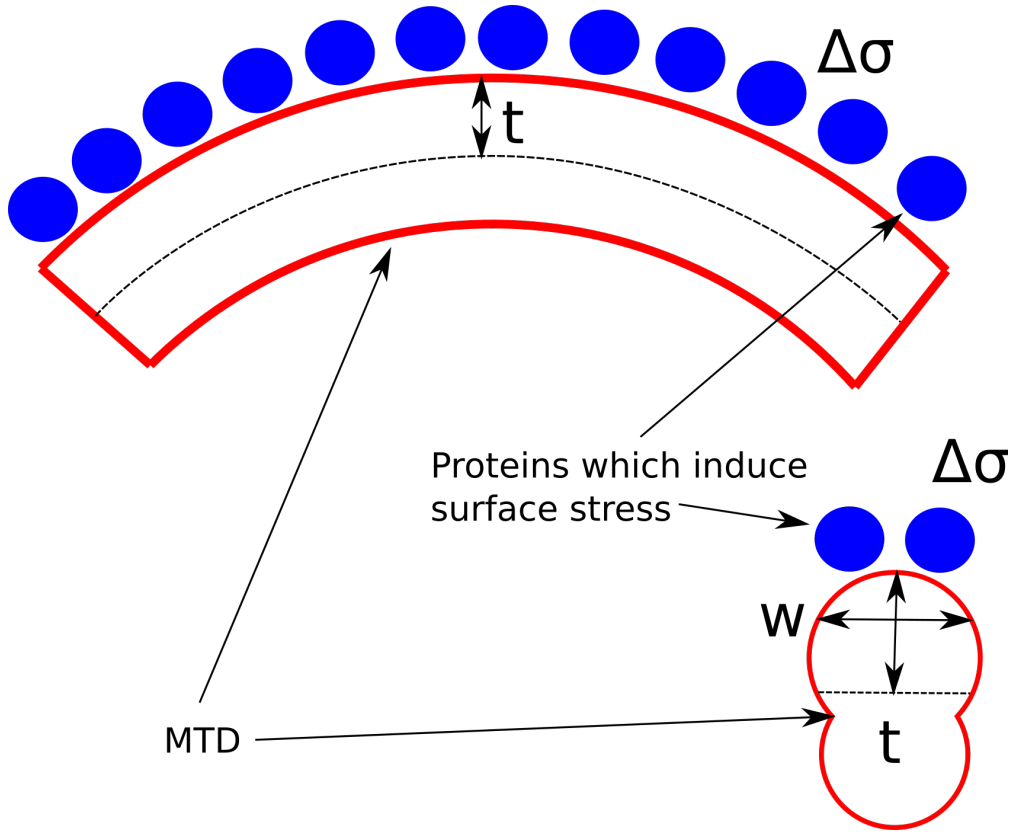

Figure 2.9: A diagram outlining the surface stress model of MTD curvature. Proteins, blue bind to one side of the microtubule, red, and generate a surface stress $\Delta\sigma$. The surface stress acts across the entire width of the MTD, w, and generates a force which acts with a lever arm of t on the MTD. From this we get the Stoney equation, eq. 2.1

We will take the Stoney equation 2.1 and multiply both sides by the thickness times the width:

$$\Delta\sigma wt = \frac{Et^2}{6R_c}wt \tag{2.2}$$

Using the second moment of inertia for a square beam, $w * t^3/12$, we can now write the surface stress as a function of the second moment of inertia generalizing this equation to beams of different cross sections:

$$\Delta\sigma wt = \frac{2Et^3w}{12R_c} \tag{2.3}$$

$$\Delta\sigma = \frac{2EI}{R_c wt} \tag{2.4}$$

where w is the width over which the proteins are binding, and t is the thickness of the microtubule in the bending plane, i.e. the length of the level arm the surface stress has. Eq. 2.3 makes physical sense because the surface stress times the width gives the force, while the thickness of the MTD is the lever arm for the generated moment, Figure 2.9.

Using the approximate modulus of microtubules from the literature, 600 MPa (63), a calculated second moment of inertia for the MTD, 7.5e-8 μm^4 (68), a width and thickness for the MTD, 25.8 nm to 38.2 nm (163), and our measured radius of curvature of 1.25 μm , we can calculate an approximate surface stress difference using the Stoney equation, equation 2.3. From this calculation we get the required surface stress difference, $\Delta\sigma$, is 0.06 N/m. This is well within the changes in surface stress caused by protein binding in AFM experiments, 0.02-0.2 N/m (116; 135; 22) and other biological molecules (161). Therefore, it is reasonable that the surface stress we see in the MTDs is caused by protein binding and that protein binding is causing the curvature in the MTDs.

This curvature should be taken into account in models of cilia actuation. At a minimum it suggests significant pre-stress in the structure, and because during a cilium beat the protein binding along the MTDs is dynamic, it suggests a new method to generate force in the cilium. To give insight on how protein-attached curvature could be critical for actuating the cilium, I would like to describe this alternate model of force generation. In this model, the dynein motors walk simply to maintain attachment to the MTD. The cilia actuation is entirely controlled by changes in surface stress along the structure as dynein motors attach and detach from the MTDs. In this model, the active and passive sides of the cilium switch. The side with the detached dynein motors generates force due to the asymmetric protein binding along the MTD, while the bound dynein motors on the opposite side balance out the surface stress on the MTD and does not generate force.

We sum up the moments generated by each of the "passive" side microtubules in a similar manner to

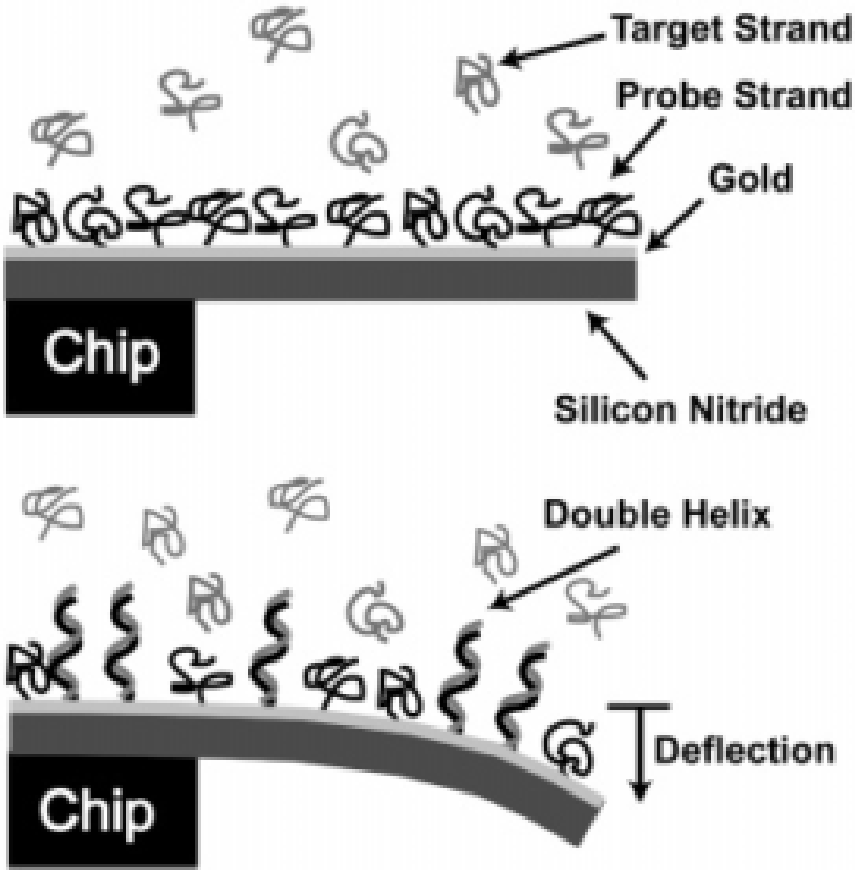

Figure 2.10: Experiments with hybridizing DNA on cantilevers show that absorption of biomolecules on surfaces asymmetrically can contribute significant stress, tens of mJ/m^2 (161)

calculations that calculated force generation for the sliding model (68). Using the stiffness of the entire axoneme, $I_{\mathrm{ax}} = 6.08 I_{\mathrm{dm}}$ (68), we can calculate an expected value using simple beam mechanics.

The total moment generated by one half of the axoneme is:

$$M_{ax} = M_{dm}\cos(70) + M_{dm}\cos(30) + M_{dm}\cos(10) + M_{dm}\cos(50) \tag{2.5}$$

$$M_{ax} = 2.84 M_{dm} \tag{2.6}$$

where M_{ax} is the moment over the entire axoneme, and M_{dm} is the moment across an MTD. The cosines represent the geometry and are taken from Hill et al. 2010, Figure 2.11. By plugging in our values for M_{ax} and I_{ax} into the beam equation we can calculate an approximate curvature for the entire cilium.

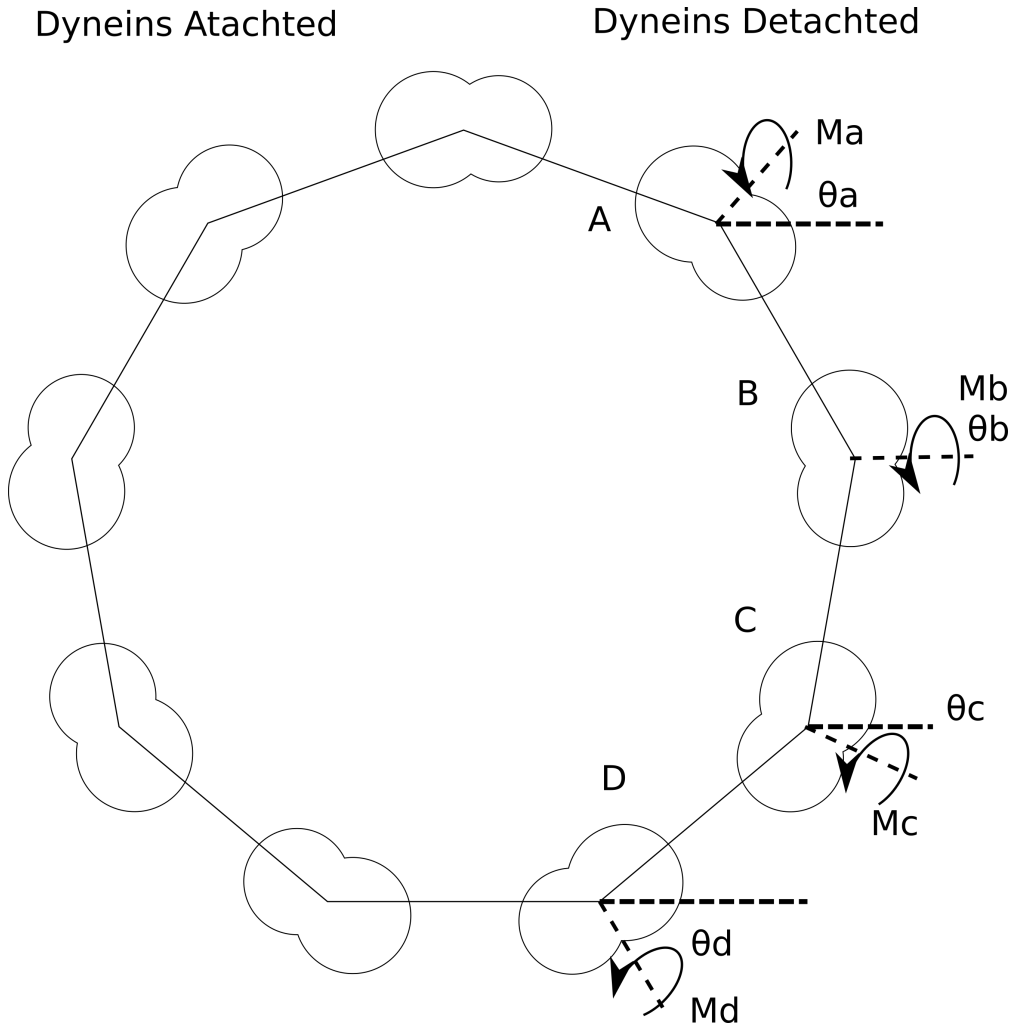

Figure 2.11: A figure showing how the geometry of the microtubule doublet affects the summation of the moments. Note that microtubule B is not perfectly horizontal but that the angle was too small to show in the diagram. The angles were plugged in to equation 2.5.

$$M = -\frac{EI}{R_c} \tag{2.7}$$

$$M_{ax} = -\frac{EI_{ax}}{R_c} \tag{2.8}$$

$$2.84M_{db} = -\frac{6.08EI_{dm}}{R_c} \tag{2.9}$$

$$R_c = -\frac{6.08}{2.84}\frac{EI_{dm}}{M_{dm}} \tag{2.10}$$

$$R_c = 2.14R_{cdm} \tag{2.11}$$

Using our curvature value for a singlet microtubule, $0.80 \pm 0.031/\mu m$, we get the maximum possible curvature generated by the MTD curvature alone is 0.4 $1/\ \mu m$. This is within 20% of the actual maximum curvature of human airway cilia which is 0.5 $1/\ \mu m$, (147).

In reality, we suspect that the sliding model and the surface stress model are working in concert. The surface stress model could help explain for some of the missing force in the cilium. Because on the "passive" side of the cilium the dyneins are deactivated, a majority of them can be detached generating maximum amount of force that our model predicts independent of the dynein duty cycle (60; 143; 68). This could explain the missing force in the cilium (68; 143).

Section 2.7: Conclusions and future work

We have shown that MTDs extracted from human airway cilia have a mean curvature value of $00.80 \pm 0.031/\mu m$. In addition, salt extraction of the outer dynein arms, confirmed with a silver staining gel, significantly reduces the curvature to $0.20 \pm 0.011/\mu m$. We proposed that this curvature is caused by the asymmetric protein binding of the dynein chains on the MTD, and showed using a surface stress argument that this level of curvature was consistent with surface stress changes due to protein binding seen in AFM cantilever experiments. We proposed that because the protein distribution on the MTD is dynamic over the cilia beat, the surface stress could be dynamic as well and contribute to the beat. We proposed a new model of how the cilia beats, which reversed the active and passive sides of the cilium. The former "passive side" now generates the force because of the asymmetric protein binding, and the dynein motors on the former active side balance out the surface energies deactivating the"active side". Using the same geometric arguments that have been used to justify the ability of dynein to generate enough force to bend the cilium, we showed that the forces generated from the surface energies model are capable to generate the observed curvatures of the entire axoneme. We hypothesize the two models work in concert to generate force on both sides of the cilium

simultaneously, potentially addressing the missing force seen in experimental measurements of cilia.

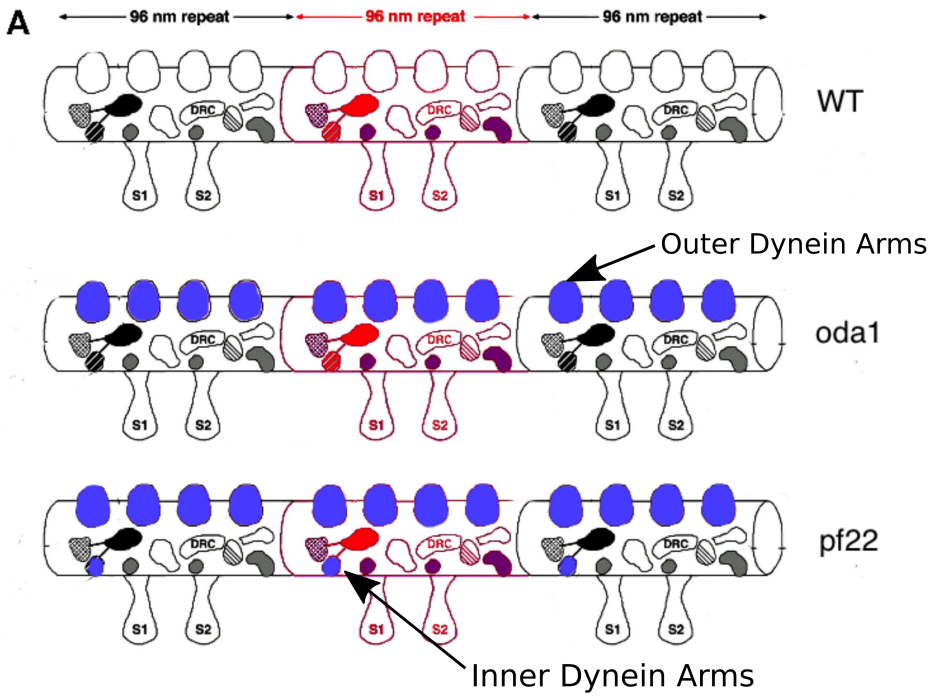

Figure 2.12: This diagram represents the proteins on a *Chlamydomonas* microtubule doublet. Proteins missing in the oda1 and pf22 *Chlamydomonas* mutants are highlighted blue.(66)

More experiments need to be completed to confirm that the MTD curvature is indeed caused by protein binding. The salt extraction step could be damaging the microtubules, which could be reducing the curvature instead of the protein binding. I propose that future experiments use a model organism such as *Chlamydomonas reinhardtii* where there are numerous genetic mutants available. The MTDs from *Chlamydomonas* mutants missing the outer dynein arms, mutant oda1 Figure 2.12, could be compared against wild type, which would allow both samples to undergo the exact same treatment and ensure that differences in curvature was due to protein binding and not a difference in the MTD treatment.

On the theoretical side, the next step is to build a computational model that includes the surface stress effects. Even if the mutants do not show a protein dependent change in curvature, we have shown that the curvature is significant on the scale of the cilium's motion. Whether the curvature of MTDs is static or dynamic, future models of the cilium need take these effects into account.

CHAPTER 3: Biomimetic actuating surface attached posts (ASAP)

Section 3.1: Introduction

In this chapter, I introduce the biomimetic cilia arrays that are the focus of the rest of the thesis. In the first section, I give a brief overview of current biomimetic cilia technology, the different actuation methods, and current applications. I describe the ASAP arrays used in this thesis, their physical properties, and how they were manufactured. I conclude the chapter with a brief discussion of some of the design limitations that are imposed on the system due to surface energy effects. I leave application specific design considerations for later chapters 5, 6.

Section 3.2: Biomimetic cilia arrays overview

3.2.1: Actuation mechanisms

In the last ten years, a large number of biomimetic cilia systems have been created that can operate as pumps and mixers (168; 169; 180; 46), see Figure 3.1. I will keep the overview of actuating cilia brief, and relevant to using cilia as sensors. For more details on using the ASAP artificial cilia as pumps and mixers, see Briana Fiser's (48), Ben Evans (45), or Adam Shields (150) theses.

At their most basic level biomimetic cilia are arrays of posts or flaps that respond to an actuating force. The most straightforward way to classify the artificial cilia systems are by their actuating mechanism. The most common mechanisms is magnetic actuation followed by electro-static actuation and there are some designs that use other actuation mechanisms.

Some of the first artificial cilia where electrostatic actuators. In 1997, Suh created one of the first arrays of biomimetic cilia with enough force to move particles. Suh used standard MEMS techniques to manufacture the arrays out of layers of polyimide with different coefficients of thermal expansion. These arrays were actuated using thermal expansion and electric forces and were capable of manipulating objects much heavier than themselves (162). In 2008, Tooden created 20-100 um electro-static flaps out of polymers and showed that they could be used as mixers (168). On a smaller scale, Lokanathan et al. created electrostatic cilia arrays with lengths between 50-500 nm using cellulose nano-crystalsthat were attached to gold surfaces (104). The negative charge of the cellulose nano-crystals allows the rods to be actuated using electro-static forces.

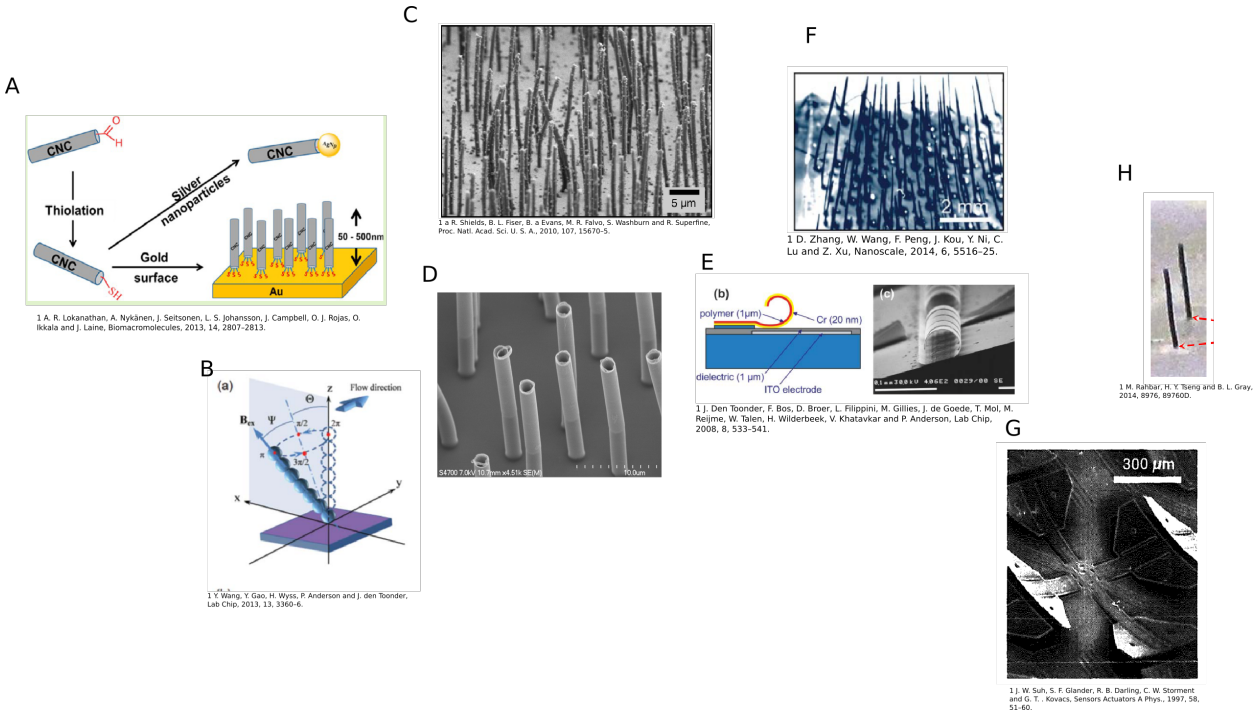

Figure 3.1: An overview of artificial cilia technologies. A) Electro-static responsive cellulose nano-crystals. The rods are 50-500 nm in length and bound to a gold surface (104). B) Self assembled magnetic bead cilia. The beads are 2.5 μm in diameter and the cilia have lengths ranging from 6 μm up to 45 μm in length (180). C) Magnetic nano-particle PDMS composite cilia (151). D) Nickel shell PDMS core artificial cilia. E) Electro-static polymer flaps cilia. The cilia are 20 μm wide and 200 μm long (168). F) PDMS core cilia that are coated with a thin carboxyl graphene film and titanium oxide layer. They are used as a photo-catalyst film where the enhanced mixing from the actuating improves the photocatalytic activity over 3 times. The artificial cilia are on the mm length scale. (196). G) MEMS thermal and electro-statically actuated cilia flaps (162). H) Magnetic nano-particle PDMS composite cilia on the mm scale (133). Images taken from their respective citations.

The most common type of artificial cilia are magnetically driven. Early magnetic systems were created using standard MEMS techniques (102; 77; 76). Ben Evans, from our own lab, developed the first magnetic-PDMS composite cilia by embedding magnetic nano-particles into PDMS (46), and other labs have made similar magnetic polymer composite cilia (133; 197; 25; 73; 47). The other direction for creating magnetic cilia have been using magnetic beads that are either permanently or magnetically linked to create arrays of magnetic responsive cilia (175; 51; 155; 180). The first wires of magnetic particle beads were not created as biomimetic cilia (51; 155), but simple strategies to create magnetic nano wires. Vilfan et al. in 2010, was the first to use these types of structures successfully as artificial cilia and showed that they could generate fluid flow (175). Later, Wang added a polymer coating step that allowed the micro self assembled arrays to remain intact when the magnetic field was removed (180). These bead based cilia are attractive due to their ease of manufacturing.

Other driving forces have been explored. In 2009, Oosten et al. developed artificial cilia actuators that responded to multiple wavelengths of light liquid crystal composites that were ink jet printed (171). These cilia are capable of complex motion by having multiple layers of light sensitive material with different activation wavelengths. By activating different polymers at different times, they are capable of creating complex motions. Liu et al. showed that colloidal polymer films can be used to create artificial cilia. By using different copolymers they manufactured cilia that responded to different signals, pH, light, and temperature (103).

3.2.2: Applications

The vast majority of artificial cilia papers focus on their use as mixers (152; 27; 105; 83; 168) or pumps (152; 3; 73; 169). Shields, from the Superfine lab, showed that magnetically actuated arrays of artificial cilia generated flow above the cilia tips, and created a region of enhanced diffusion below the cilia tips, see Figure 3.2. Shields also showed that the generated flow was similar to the flow generated by a moving boundary condition. These experiments were performed with PDMS nano-composite posts, which were the precursors to the current ASAP arrays.

Since then, there have been numerous experimental and numerical studies on the best beat shapes and cilia distributions to achieve effective pumping or mixing (174; 40; 85; 26; 28; 3). Recent computational work suggests that artificial cilia may be able to control particle distributions in the channel (107; 13; 54). Their modeling suggests that depending on the ratio between the viscous and elastic forces, the artificial arrays will either pull or push out particles of a given size (108; 13; 54).

There has been considerably less work on using artificial cilia arrays for microfluidic devices as sensors.

The work has been focused passive posts that act as flow sensors (20; 21; 87; 65; 56; 128; 35; 36). These systems are passive single rods or array of rods that deflect under fluid flow. The deflection is measured and used to measure the shear stress. They have been shown to operate well in the low Reynolds number regime (20) and in the high Reynolds regime (56); however, all the systems are passive and are not driven arrays. There have not been any papers on using driven arrays of biomimetic cilia as sensors. The closest analogue in the literature are AFM cantilever experiments (94; 172), where driven micro cantilevers response is monitored and used to measure the fluid properties. However, these systems operate at high frequencies, (10^2 -10^4 Hz), which limit their practicality for specimens where the low frequency material properties are of interest, often the case in biological fluids such as mucus or synovial fluid (34; 146). AFM cantilever systems are also difficult to integrate into micro-fluidic systems. Our ASAP arrays are unique as sensors because they are arrays of driven micro-posts rather than passive sensors that operate in the low frequency regime.

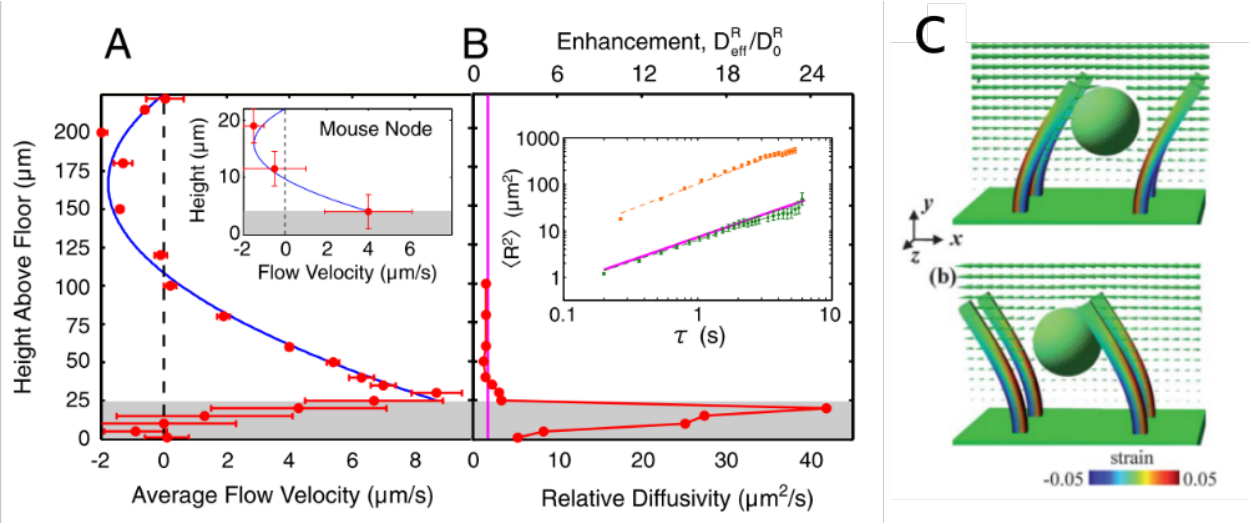

Figure 3.2: A) A plot of the average fluid profile over an array of actuating cilia. Net flow is shown directly over the cilia. Because the channel is closed there is a net back-flow further up in the channel. The flow is a combination of Cuvette flow and Poiseuille flow. Reproduced from (151). B) A plot of the relative diffusivity as a function of height over the cilia arrays. Below the tips of the cilia array diffusion is greatly enhance while above the array the relative diffusifity quickly goes to one. Reproduced from (151). C) A figure showing a computation model of a cilia array with particles. Masoud and Alexeev showed that in addition to moving particles along with the generated fluid flow that, depending on the ratio of the viscous forces to elastic forces, the cilia array will either pull particles into the cilia layer or push them out. Reproduced from (108)

Section 3.3: ASAP overview

The artificial cilia used in thesis this were developed by Briana Fiser (48) to address two issues with magnetically actuated cilia. Magnetic bead cilia have little to no restoration force and collapse without a magnetic field. Magnetic nano-particle PDMS composites couple the magnetic responsiveness with the

material stiffness. As the fraction of magnetic material increases, the stiffness increases as well (48; 45). Briana Fiser addressed this issue by designing a core shell structure using PDMS as the core and nickel as the magnetic shell, separating the magnetic responsiveness and material properties (Fiser et al.; 48). The post arrays used in this thesis have a diameter of 2 μm and a height of 25 μm . The nickel shell reaches approximately half way down the post and is 200 nm thick, Figure 3.3. These dimensions where chosen to maximum the post stability and the actuation force (48).

3.3.1: Manufacturing

The ASAP arrays in this thesis were fabricated either by Rheomics, Inc. (Chapel Hill, NC) or myself using a modified version of the procedure developed by Fiser (48).

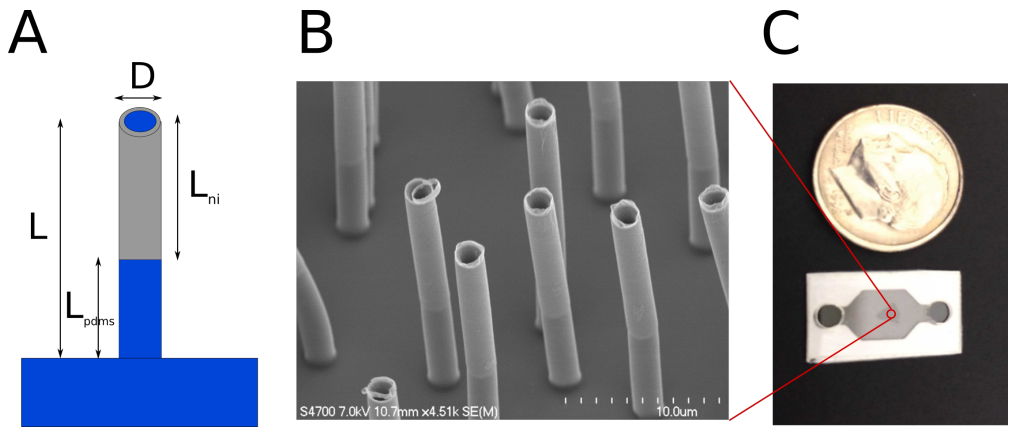

Figure 3.3: A) Cartoon of a single ASAP post. The key parameters for the post design are the total length L, the Nickel shell length L_{ni}, the length of the PDMS section L_{pdms}, and the post diameter D. B) An SEM image of a finished ASAP array. C) A photo of the ASAP arrays mounted in a microfluidic chamber.

The posts are created using a template based molding process, that results in a 200 nm thick nickel shell around a PDMS core, see Figure 3.3. The posts are molded using a track etch polycarbonate membrane, which determines the post height, diameter, and density.

ASAP arrays were made using a template-based process that utilizes a polycarbonate track etched (PCTE) membrane (it4ipTM, S.A., product number # 100M25) as a mold for the core-shell structures. First, the nickel shell of the structure was created by coating one side of the track etched membrane with a 200 nm thick layer of gold that served as the cathode for electro-deposition of nickel into the pores. To prevent nickel deposition on the backside, a 10 nm later of aluminum is sputtered onto the gold layer. Nickel does not deposit well on the aluminum oxide layer because of a mismatch in the crystal structure pacifying the back side of the membrane, while the gold lip inside the pore is still exposed. Both layers were applied using a Kurt Lesker PVD 75 sputter coater in a clean room.

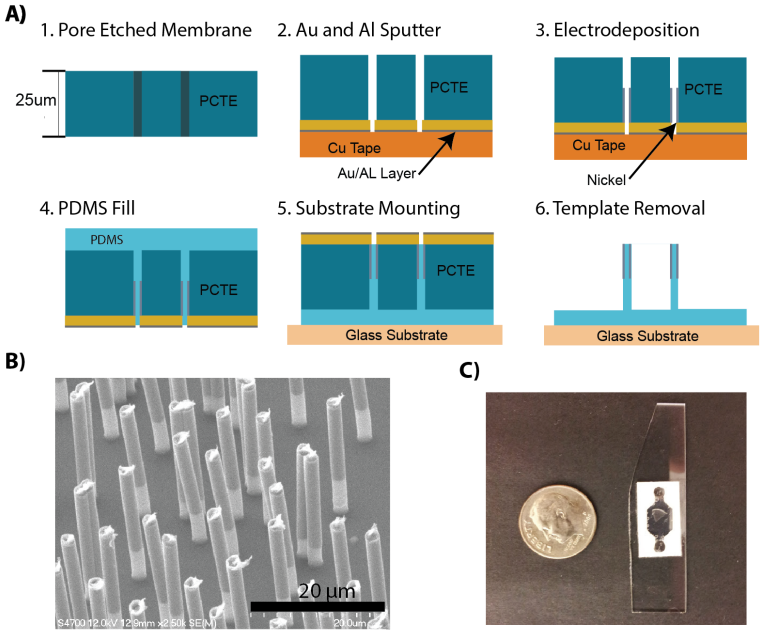

Figure 3.4: A diagram of the manufacturing process. 1) We start with a PCTE membrane with a thickness equivalent to the desired post height, and with pores with the desired diameter and post density. 2) A 200 nm thick gold layer and 10 nm aluminum layer is sputtered onto the back of the template forming a gold lip inside the pores. The entire membrane is mounted on conductive copper tape. 3) The membrane is mounted into an electro deposition cell and nickel is deposited into the pores forming tubes. 4) PDMS at a 10:1 PDMS:Cross-linker ratio is filled into the membrane. 5) After curing the filled membrane is mounted onto a glass substrate using plasma cleaning. 6) The nickel and gold layers are etched away using sodium hydroxide and a nickel compatible gold etchant. The posts are then either used immediately or dried using a critical point dryer or freeze dryer for later use.

The membrane was mounted into an electrodeposition cell using double-sided copper tape to ensure even electrical contact. Electro-deposition was performed in a custom electrolytic cell with an all-sulfate plating bath (60 g/L $NiSO_4*6H_2O$, 30 g/L H_3BO_3, pH 2.9 using H_2SO_4) (48). Nickel tube length is determined by the quantity of nickel deposited. Upon completion, the nickel containing track etched membranes were rinsed with DI water and dried. The core of the structures was made by filling the membrane with PDMS (Dow Corning, Sylgard 184) at a 10:1 base to cross linker ratio. Prior to curing the PDMS, a 22 x 22 mm coverslip (Corning, 2870-22) was pressed into the uncured elastomer to provide a rigid substrate for the array. After curing the PDMS, the gold layer (cathode) was removed using a nickel compatible gold etchant (Aldrich, 651842) and the posts were released by dissolving the polycarbonate template using dichloromethane (ACROS Organics, 610300010). Released posts were then stored in ethanol until they were dried using a critical point drier (Balzers Union, CPD 020). ASAP fabrication is summarized in Figure 3.4.

The procedure above is essentially the same as the procedure developed by Briana Fiser (Fiser et al.; 48), except for the following additions the aluminum pacification layer, the copper tape adhesive, and the chemical etching. Previously, posts were released from the gold layer by mechanical abrasion. These new additions improved the fraction of functional arrays from around 10% to 40-50%. After these developments, Rheomics Inc. began manufacturing the ASAP posts. They have made additional improvements to the manufacturing process, not detailed here, to further improve yields and consistency.

3.3.2: Design limitations

The rest of this thesis will focus on the modeling and use of the ASAP arrays as sensors. In later chapters, we will show that the post sensitivity depends on material properties, which can be adjusted during the manufacturing process. Adjustable parameters include post density, post height, post diamter, nickel-shell length, and nickel-shell thickness. Because of the ease of acquiring PCTE membranes of different thickness, densities, or pore sizes, it is easy to change any of these parameters. Adjusting the nickel length is simply a mater of changing the quantity of nickel deposited during electro deposition, and the shell thickness can be controlled by the thickness of the sputter coated gold layer.

Unfortunately not all values of the parameters produce viable posts. Due to the high surface energy of PDMS in water, there is adhesion causing PDMS to self adhere leading to irreversible collapse of the post arrays. (136). Posts are considered collapsed when they are irreversibly bound to the ground (ground collapse) or each other (lateral collapse).

Roca-Cusachs et al. developed an analytical model of both modes of collapse that we used set bounds on our post properties. Because the posts are not entirely made out of PDMS and the top half is coated

in nickel, these equations will over estimate the collapse criteria. The critical ratio between the post length and diameter for ground collapse is given by:

$$\left(\frac{h}{b}\right)_G = \frac{\pi^{5/3}}{2^{11/3}3^{1/2}}(1-v^2)^{-1/6}\left(\frac{E}{W}\right)^{2/3} b^{2/3} \tag{3.1}$$

where h is the post height, b is the post diameter, s is the inter post spacing, E is the elastic modulus of the material, v is the Poisson's ratio, and W is the work of adhesion. W is 86 mN/m for PDMS in water (136).

For lateral collapse the equation is:

$$\left(\frac{h}{b}\right)_L = \left[\frac{\pi^4 3^3}{2^{11}(1-v^2)}\right]^{1/12}\left(\frac{s}{b}\right)^{1/2}\left(\frac{E}{W}\right)^{1/3} b^{1/3} \tag{3.2}$$

where s is the inter post spacing (136). Using these two equations we calculated the maximum aspect ratios achievable at different post densities, see Figure 3.5.

We are able to create stable posts as long as we remain in the valid design space. From Figure 3.5, we can see that for our post arrays with a diameter of 2 μm , and a post density of 1.5e6 $1/cm^2$, and a height of 23 μm , we are right at the limit for ground collapse. As posts get thicker lateral collapse becomes the primary concern, see Figure 3.5.

The collapse criteria is not an absolute limit, but rather the limit of posts which are stable. Our lab has successfully made posts outside of this valid regime. Fiser routinely made .55 μm diameter and 10 μm tall core shell structures (48), and Ben Evans had similar success with nano-composite cilia (45); however, these posts were highly susceptible to collapse when fluid was added or removed from the posts arrays. Ideally posts will be made that exist inside the valid design space as they are more robust to dynamic environmental conditions.

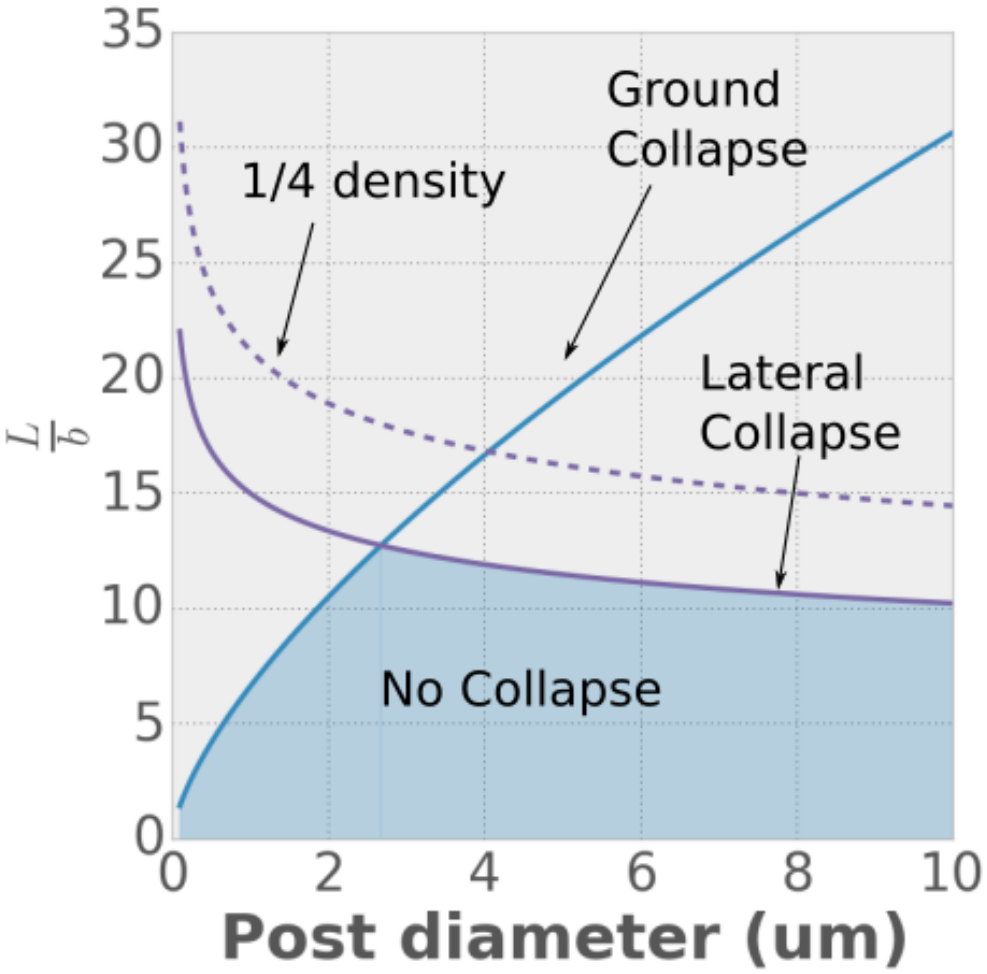

Figure 3.5: This plot shows the maximum aspect ratio before ground collapse occurs, blue, and lateral collapse, purple as a function of the post diameter. The shaded region is the design space of stable posts. The purple dashed line shows how the reducing the post density by a factor of 4 increases the design space.

CHAPTER 4: Modeling ASAP arrays

Section 4.1: Introduction

In this chapter, I will create a model of our ASAP arrays. In the ASAP system we apply a magnetic field which causes the posts to deflect. It is possible to measure the post deflection directly using microscopy and images of the posts, Figure 4.4A; however, it is simpler to measure the posts deflection indirectly by using the intensity of transmitted light through the sample. The nickel portion of the composite rod is opaque and as the posts deflect the nickel blocks more of the transmitted light reducing the intensity. In order to understand the transmitted light signal at all, it is necessary to build a model of the post-fluid-microscope system that takes into account the intensity signal, magnetic response, and the fluid structure interaction.

I will start this chapter by giving an overview of previous modeling work done on biological and biomimetic cilia arrays (section 4.2). Then I will outline the different parts of the model and how they interact with each other (section 4.3). In the following sections, I will then develop the model components (magnetic, optical, and mechanical) separately and compare the results of the entire model to experimental results. The mechanical model will consist of three different models of varying levels of sophistication. I will briefly describe a simple model that neglects the fluid drag forces effects on the post motion. I will then develop an analytical model of the composite post that fully incorporates the effects of the fluid drag and magnetic forcing on the post motion. These analytical models neglect the no slip boundary of the floor benieth the post and are limited to small angle oscillations. I will compare these two models to a finite element model of a single post built in COMSOL that includes these effects. Finally, I will discuss the next steps for a more advanced model and the possibility of introducing post-post interactions.

Section 4.2: Previous modeling work

Both numerical and modeling studies have been done on the flow around post arrays (26; 105; 82; 3; 28; 174; 85). Additionally, there is a considerable body of computational work that focuses on trying to understand the dynamics of biological cilia arrays.(115; 157; 156) These models either assume a prescribed motion of the posts and model the resulting fluid dynamics, or are complex numerical simulations. These types of models are difficult to invert and use to calculate the material properties for a given post response making them unsuitable for measurement applications.

The dynamics of single-filament fluid structure interactions have been studied analytically (189; 188; 44; 5). These models have been used to describe artificial swimmers and fluid shear sensors (42; 20; 21). In general, the dynamics of these systems depend on a dimensionless parameter known as the sperm number (189). The sperm number represents the ratio of the viscous drag forces on the actuator to the internal elastic forces and determines the shape of the post motions:

$$Sp = L\left(\frac{4\pi\omega\eta}{EI}\right) \tag{4.1}$$

where L is the length of the flexible filament, ω is the angular frequency of the motion, η is the viscosity of the fluid, E is the elastic modulus of the filament, and I is the second moment of inertia. At low sperm numbers, $Sp << 1$, the elastic forces dominate and the deflection of the rod is well describe by standard beam mechanics. At large sperm numbers, $Sp >> 1$, the viscous forces dominate and waves form along the filament. The sperm number can be though of as the number of wavelengths that fit within the length of the elastic filament (189).

In multi-post systems, the sperm number is equally important. Computational studies of the fluid flow generated by actuating post arrays show that the nature of the flow depends heavily on the sperm number. In the paper by Alexeev, they show in a computational model that as the post arrays are driven through a sperm number of one, the fluid flow generated by the posts reverses direction (3). Further simulations show that how particles interact with the post arrays and the surrounding fluid depends on sperm number (107; 10).

Section 4.3: Model overview

To date no one has used these models and artificial cilia arrays as a rheometer or sensor for the physical properties of the fluid that they are embedded in. Additionally, the composite nature of our posts requires a new model. We will develop the model in a modular manner, see Figure 4.1, first developing a model for how the light intensity is related to post deflection, then a model for the magnetic force on the posts, and finally we will develop a model for the fluid structure interaction.

The raw experimental output of the ASAP arrays are the transmitted light intensity through the array and the applied magnetic field, dark blue in Figure 4.1.

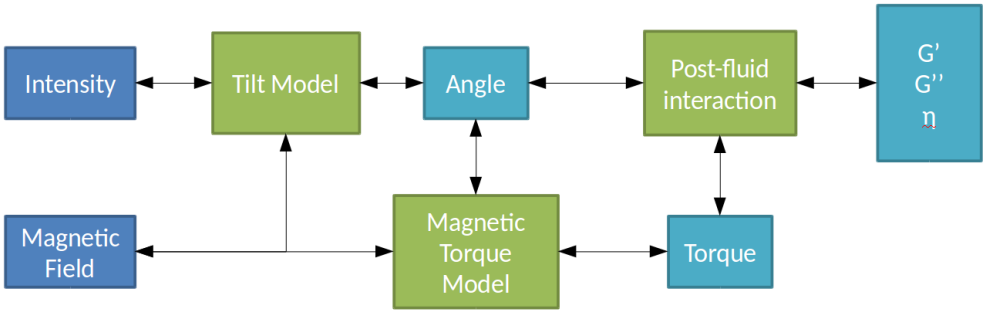

Figure 4.1: Diagram of the different model parts and how they interact with each other. Dark blue represents measured values. Green are the different components of the model, and light blue are calculated values. The intensity is converted into a post angle using the tilt model. The angle and the applied field are then used to calculate the torque on the rod. The angle and the torque signals are used with the fluid interaction model to calculate the fluid properties.

Section 4.4: Tilt model

The intensity of the transmitted light through the posts is measured during the experiment. The goal is to relate the transmitted light intensity to an angle of post deflection. This is done by how the nickel shell blocks light as the post deflects. We model the nickel shell as a solid rectangle with a width, a, and a length, b. The projected length of the nickel, L, can be calculated from the geometry and the angle of the post using simple trig (Figure 4.2).

$$L = b\sin\theta + a\cos\theta = c\sin(\theta+\phi) \tag{4.2}$$

$$c = \sqrt{b^2+a^2} \tag{4.3}$$

$$\phi = \arctan(b,a) \approx 10^o \tag{4.4}$$

where L is the projected length of the nickel, a and b are the long and short sides of the post respectively, and ϕ is an angle correction for the fact that the projected length is the diagonal of the nickel rod.

Experimentally we measure the change in intensity. We will normalize the intensity to the maximum intensity, i.e. when the magnetic field is off. We can then write the normalized change in intensity as:

$$\frac{\Delta I}{I_{off}} = \frac{I_{off}-I_{on}}{I_{off}} = 1 - \frac{I_{on}}{I_{off}} \tag{4.5}$$

where I_{off} is the transmitted intensity with the magnets off and I_{on} is the transmitted intensity with the magnets on (deflected posts). I_{on} is I_{off} minus the area blocked by the posts. Because the posts are not perfectly black due to scattered light and other optical effects there is a constant that represents the contrast ratio. I_{on} is then:

$$I_{on} = I_{off} - CNA(\theta) = I_{off} - CNA(\theta) \tag{4.6}$$

where C is the contrast ratio of the nickel to the PDMS, N is the number of posts in the field of view (which is the density, ρ, times the field of view), and $A(\theta)$ is the area occluded by a post, which depends on the angle of the tilt.

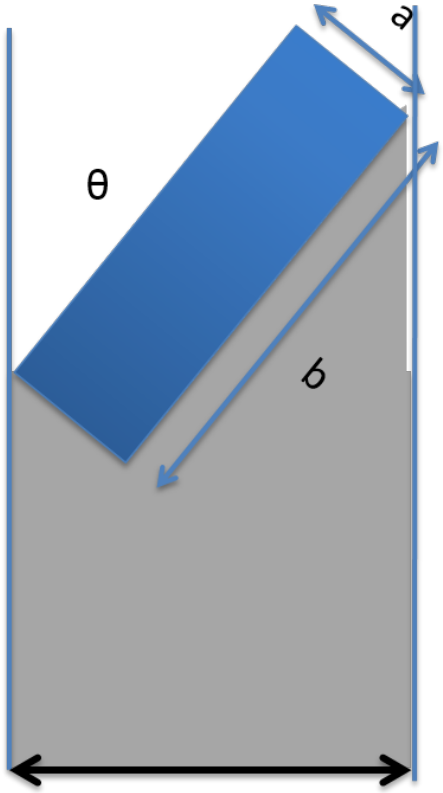

Figure 4.2: Diagram of the tilt model. The nickel portion of the rod is modeled as a solid rectangle with width a and length b. The projected length, L, can then be calculated using trigonometry, eq. 4.2.

Combining equation 4.2, 4.5, and 4.6 we get the following equation for the change in intensity and the post angle:

$$\frac{\Delta I}{I_{off}} = \frac{C\rho(c\sin(\theta+\phi)}{I_{off}} \tag{4.7}$$

The prefactor $C\rho$ is calibrated using an image of the post bent over under a magnetic field. The average projected length of the nickel is measured as well as the change in intensity between the images and is used to calculate the tilt angle, see Figure 4.4A.

For every experiment we preform a tilt test, which is used to convert intensity changes to post deflections by finding the value of $C\rho c$ for a given post array. The tilt test is a ramp of increasing magnetic field applied to the posts. At each point an image is taken. The change in intensity at each step is measured along with the nickel deflection (measured directly from the images). Equation 4.7 is then fitted to the results where $C\rho c$ is used as the fitting parameter (Figure 4.4).

Section 4.5: Magnetic response

Ben Evans, Briana Fiser, and Adam Shields used a permanent magnet to actuate the posts (48; 150; 45). The high magnetic field enabled them to use an energy minimization model for the magnetic forces on the ASAP arrays. In this thesis, I will use an electromagnet to acquire more fine-grain control over the actuation of the posts, but at lower field strengths. In order to model the magnetic forces below and above magnetic saturation, a new magnetic model is needed.

Abbott developed a magnetic model for prolate and oblate spheroids of soft magnetic material (1), above and below saturation. In Abbott's model, the magnetic response of the posts is separated into two regimes. Above saturation the same energy minimization model that Evans, Fiser, and Shields use holds. Below saturation the magnetization is described by the following equation:

$$M = \chi_a H \tag{4.8}$$

$$\chi_a = \text{diag}\left(\frac{\chi}{1+n_x}, \frac{\chi}{1+n_y}, \frac{\chi}{1+n_z}\right) \tag{4.9}$$

where M is the generated moment, χ_a is the magnetic susceptibility that depends on the material and geometry, χ is the materials magnetic susceptibility, and $n_{x,y,z}$ are the geometric demagnetization parameters. If we assume a large value of χ, greater than 10^3, we can simplify χ_a to:

$$\chi_a = \text{diag}\left(\frac{1}{n_a}, \frac{1}{n_r}, \frac{1}{n_r}\right) \tag{4.10}$$

where n_a is the geometric demagnetization factor for the long axis and n_r is the demagnetization factor for the short axis. n_a is determined by the following equation:

$$n_a = \frac{1}{R^2-1}\left(\frac{R}{2\sqrt{R^2-1}}\ln\left(\frac{R+\sqrt{R^2-1}}{R-\sqrt{R^2-1}}\right)-1\right) \tag{4.11}$$

$$R = L_{long}/L_{short} \tag{4.12}$$

We can calculate the angle of the induced moment by expanding the equation 4.8. Doing the calculation gives us the angle of the magnetic moment:

$$\psi = \tan^{-1}\left(\frac{n_a}{n_r}\tan\phi\right) \tag{4.13}$$

where ψ, is the angle between the post and the generated moment, and ϕ is the angle between the post and the magnetic field (Figure 4.3).

Above saturation the equations change. The induced moment is constant, $|M| = m_s$, and the angle of the moment is calculated by minimizing the magnetic energy:

$$e = \frac{1}{2}\mu_0 v(n_r - n_a)m_s^2\sin^2\psi - \mu_0 v m_s|H|cos(\phi-\psi) \tag{4.14}$$

where v is the nickel volume, e is the energy, μ_0 is the permitivity of free space, m_s is the saturation moment, ψ is the angle between the long axis and the induced moment, and ϕ is the angle between the magnetic field and the long axis of the rode. Minimizing this equation gives us the following nonlinear equation for the induced moment angle, which can be solved numerically:

$$(n_r - n_a)m_s\sin(2\psi) = 2|H|\sin(\phi-\psi) \tag{4.15}$$

The saturation magnetic field is determined by the following equation (1):

$$|H|_{sat} = \frac{m_s n_a n_r}{\sqrt{n_a^2 \sin^2\phi + n_r^2 \cos^2\phi}} \tag{4.16}$$

It is now possible to calculate the induced torque using the standard equation:

$$T = \mu_0 v M \times H \tag{4.17}$$

Combining equations 4.17, 4.13, 4.15, and 4.16, and including a remanent magnetic moment along the long axis of the rod, m_{rem}, we get the following equation for the torque on the rod:

$$|\tau_{mag}| = m_{rem}|B|\sin(\phi - \psi) + \begin{cases} \frac{v|n_r - n_a|}{2\mu_0 n_a n_r}|B|^2 \sin(2\phi), |B| < |B|_{sat} \\ \frac{\mu_0 v|n_r - n_a|}{2} m_s^2 \sin(2\psi), |B| \geq |B|_{sat} \end{cases} \tag{4.18}$$

where ψ is calculated using equation 4.15, and equation 4.13.

Section 4.6: Experimental validation of magnetic and tilt Models

To validate the magnetic and tilt models we performed a simple experiment. The posts are subjected to increasing magnetic fields at a constant angle (10 degrees) from horizontal. As the field increased, the angle of the posts was measured using the transmitted intensity and tilt model. The transmitted intensity model is calibrated for a given post array by measuring the percent change in the average image intensity with the magnetic field on and off, while simultaneously directly measuring the post angle by measuring the projected length of the deflected nickel portions for a single magnetic field. This calibration point was used to calculate the change in pre-factor, $C\rho$, in equation 4.7.

Deflections were calculated by solving the torque balance equation using the quasi-static assumption:

$$\tau_{mag} + \tau_{post} = 0 \tag{4.19}$$

where the torque due to bending, τ_{post}, is calculated using an Euler-Bernulli Beam Model. Because the magnetic field applies a pure torque, it is assumed that the PDMS portion of the posts bends with a constant radius of curvature. This has been shown to introduce an error of less than 30% (46).

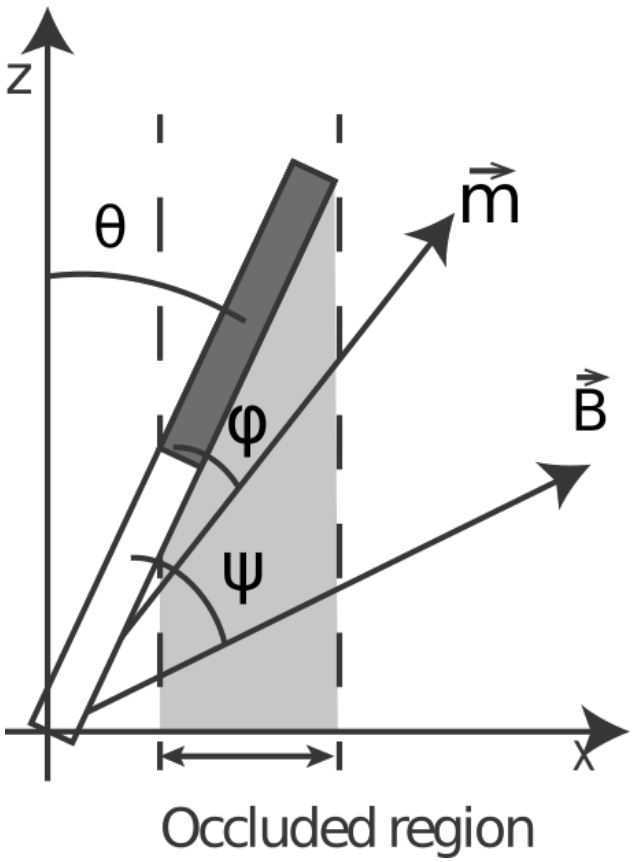

Figure 4.3: The angle of the posts from vertical is θ, ϕ is the angle between the rod and the induced moment, and ψ is the angle between the rod and the applied magnetic field.

The torque is therefore:

$$\tau_{post} = \frac{dU_E}{d\theta} = \frac{\pi E r^4 \theta}{L_{PDMS}} \tag{4.20}$$

where E is the elastic modulus of PDMS, r is the radius of the post and L_{PDMS} is the length of the PDMS portion of the rod. For the geometry of the model we assumed a nickel shell thickness of 200 nm, a nickel shell length $13 \pm 1 \mu m$ and a post diameter of 2 μm. For material properties, the elastic modulus of PDMS was fitted to be $0.85 \pm .07$ MPa and the permanent moment of the rod was fitted to the measured post response (see below). The fitted permanent moment of the nickel shell was $(4 \pm 1) \times 10^{-13}$ Am^2. The predicted deflection of the posts can be seen in Figure 3C.

The experimental deflection vs. field results agree well with the predicted results from the model, see Figure 4.4. The model curve was calculated by numerically solving equation 4.19 using equations 4.18 and 4.20 for the magnetic and post torque. The only parameters that were fitted was the permanent moment term, and the post stiffness. The rest of the model parameters were based off of known and measured values for the posts, including the material properties of nickel, the post dimensions, length of the nickel rods, and volume of the nickel shells. The fitted permanent moment, $2 \times 10^{-13} Am^2$, was consistent with remanence from a previous exposure to a magnetic field, as it was less than the predicted moment generated under the largest applied fields (50 mT). The fitted PDMS elastic modulus of $0.85 \pm .07$ MPa is within the expected range (50).

Prior to experiments ASAP arrays were pulsed with varying magnetic fields over the full range of a typical experiment to test actuation. This initial exposure to the magnetic field likely introduced the permanent magnetic moment. Additionally, because the magnetic susceptibility of a high ratio structure is dominated by the geometry and not by the material properties, the equations for the induced magnetic moment should not change significantly.

Section 4.7: Fluid-structure model of posts

4.7.1: Fluid modeling

To model the fluid-post interaction we will use the low Reynolds number approximation of the Navier-Stokes equations. Previous theses on the ASAP arrays have gone into great depth on the Navier-Stokes equations and their basic solutions applicable to the flow generated by cilia. I will not recreate their work here and will simply refer the reader to their excellent theses (48; 150).

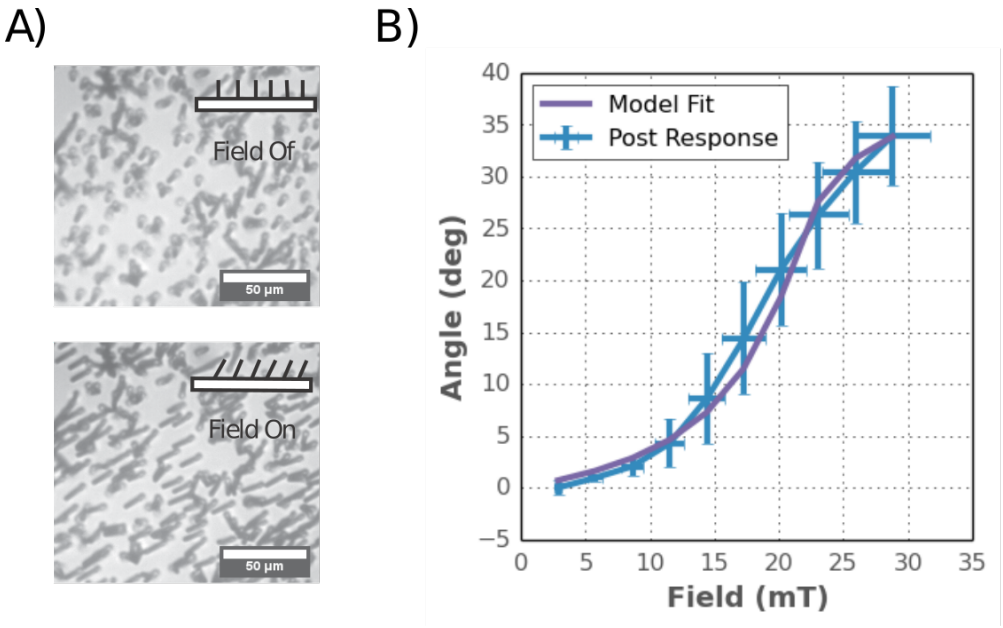

Figure 4.4: A) Sample images of the post arrays with the magnetic field on and magnetic field off, 50 μm Scale Bar. B) Measurements of ASAP deflection compared against the theoretical model, eq. 4.18. The x-axis is the applied magnetic field and the post response in degrees of tilt is plotted on the y axis. The purple line is the deflection predicted by our model with a single-parameter fit. All inputs were determined from independent measurements or known material properties except for the remanent magnetization of the posts.

In this thesis, I will focus on the Oseen Tensor and slender body theory for force on a rod, which we will use to model the hydrodynamic interaction between the post and the fluid. We will start with the Navier-Stokes equation as originally derived by Navier in 1827 for a incompressible Newtonian viscous fluid:

$$\rho\left(\frac{\partial\vec{u}}{\partial t}+\vec{u}\cdot\nabla\vec{u}\right)=-\nabla p+\eta\nabla^2\vec{u}+\rho\vec{F} \tag{4.21}$$

where ρ is the density of the fluid, $\vec{u}$ is the velocity of an infinitesimal fluid unit, p is the pressure, η is the viscosity, and $\vec{F}$ is the applied force.

We will make two assumptions to simplify the problem. The first assumption is that the instantaneous flow is approximately steady state (20; 189), removing the $\frac{\partial\vec{u}}{\partial t}$ term. Additionally, because we are in the low Reynolds number regime, $Re=\rho vl/\eta << 1$, inertial effects are not significant so we can remove the nonlinear inertial term, $\vec{u}\cdot\nabla\vec{u}$. We are now left with the simplified linear Navier-Stokes equation and the conservation of mass equation:

$$-\nabla p(\vec{r}) + \eta \nabla^2 \vec{u}(\vec{r}) = -F \tag{4.22}$$

$$\nabla \vec{u} = 0 \tag{4.23}$$

It is important to note that these equations are now linear, which means that if two solutions f_1 and f_2 exist then $f_1 + f_2$ is also a solution. This enables us to model a slender beam, such as our posts, as a series of point forces known as Stokeslets. A Stokeslet is the solution to equation 4.22 for a point force within the fluid and boundary conditions that vanish at infinity, see Maciej Lisicki's "Four approaches to hydrodynamic Green's functions" for a derivation for how to derive the flow and pressure fields for a Stokeslet (101; 81).

$$p(\vec{r}) = \frac{\vec{F} \cdot vecr}{4\pi r^3} \tag{4.24}$$

$$u(\vec{r}) = \frac{\vec{F}}{8\pi\eta r}\left(\mathbb{I} + \frac{\vec{r}\vec{r}}{r^2}\right) \tag{4.25}$$

where F is the magnitude of the point force, $\mathbb{I}$ is the identity tensor and $\vec{r}$ is the vector from the origin. $u(\vec{r})$ is often known as the Oseen Tensor.

To calculate the force from the fluid on a slender rod or any other slender body, we will integrate a series of Stokeslets along the centerline of the body. The Stokeslets force values will be chosen so that the fluid velocity at the boundary of the rod will equal velocity of the boundary, i.e. no slip boundary conditions. The force of the Stokeslets can then be integrated to calculate the force per unit length on the rod, see "Computing Flows Around Microorganisms: Slender Body Theory and Beyond" for a detailed derivation of this term (121). The end result is that for a slender body, such as our ASAP posts, the force along the posts can be modeled as:

$$\text{Oseen Drag} = \frac{4\pi\eta v}{\ln L/2D} \tag{4.26}$$

where η is the fluid viscosity, v is the velocity of the post, L is the total length of the rod, and D is the diameter. From now on we will call this term the drag term which represents the force of the fluid per unit length on the rod.

4.7.2: Analytical model

In order to model the fluid structure interaction we will expand the model developed by Wiggins in 1998 (189) to include composite posts. In Wiggins' model, the flexible filament is modeled as a slender beam using beam mechanics. The forces on the rod due to the fluid are modeled as an Oseen drag term, see above (189; 20; 173). In our case, instead of a purely elastic beam, we have a composite beam. The nickel portion of the rod is over 3 orders of magnitude stiffer than the PDMS and will be considered as completely rigid.

Therefore, we will use the Wiggins model only on the flexible PDMS portion of the rod. The drag forces and applied magnetic forces on the nickel portion will be included in the model as boundary conditions applied at the end of the PDMS that depend on the motion of the rod and applied magnetic field, Figure 4.5. The motion of the nickel rod is entirely dependent on the motion of the end of the PDMS rod, Figure 4.5.

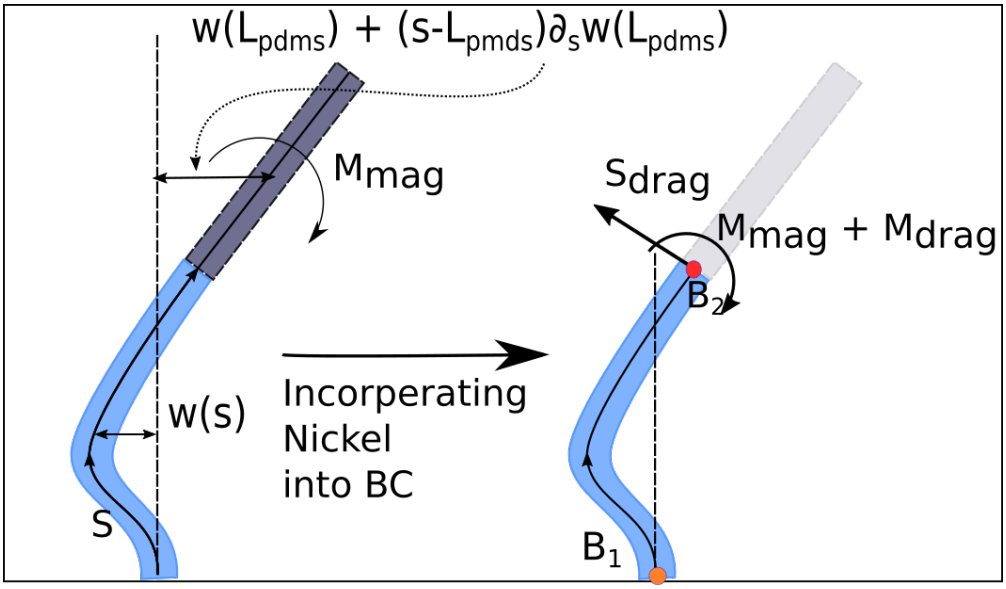

Figure 4.5: Diagram of the full model. The nickel portion of the rod is treated as a rigid and its movement is entirely determined by the boundary conditions at point 2 (red). The angle is determined by the first derivative and the location of the end $w(s)$. The model solves for the PDMS shape using a fluid interaction model developed by Wiggins, (189) s is the length along the arc length.

4.7.3: Equations

We will start using the same equations as Wiggins (189). Assuming that the deflections are small and that the post motion is in the low Reynolds regime where inertia can be neglected, we get the following differential equation for the deflection of the post from vertical as a function of the arc length s:

$$EI\frac{\partial^4 w(s)}{\partial s^4} = \frac{-i4\pi\eta\omega}{\ln(L_{tot}/2D)}w(s) \tag{4.27}$$

$$\frac{s}{L_{PDMS}} = \alpha \tag{4.28}$$

$$EI\frac{\partial^4 w(\alpha)}{\partial \alpha^4} = \frac{-i4\pi\eta\omega L^4}{EI\ln(L_{tot}/2D)}w(\alpha) \tag{4.29}$$

$$\frac{\partial^4 w(\alpha)}{\partial \alpha^4} = \frac{-iSp^4}{\ln(L_{tot}/2D)}w(\alpha) \tag{4.30}$$

where E is the elastic modulus, I is the second moment of inertia, w is the displacement from vertical, which is dependent on s distance along the centerline of the post, η is the viscosity, ω is the frequency of the oscillation, L_{tot} is the total length of the nickel, and D is the post diameter. In the above equations we nondimensionalize the equations using the parameter $\alpha = s/L_{PDMS}$ where L_{PDMS} is the length of the PDMS portion. This allows us to ultimately write the equation in terms of the Sp^4 and a term that represents the ends effects. To put the equation in a standard form, we will sub in k^4 for $\frac{Sp^4}{\ln(L_{tot}/2D)}$:

$$\frac{\partial^4 w(\alpha)}{\partial \alpha^4} = -ik^4 w(\alpha) \tag{4.31}$$

This differential equation has a known solution:

$$w(\alpha) = \sum_{j=1}^{4} c_j e^{i^j z_0 k\alpha} \tag{4.32}$$

$$z_0 = e^{-i\pi/8} \tag{4.33}$$

where c_j are the constants to be determined by the boundary conditions, and z_0 is the fourth root of i. Up until this point the analysis is the same as in Wiggins and the nickel portion of the rod is completely ignored.

Boundary conditions

The nickel portion of the rod is included in the boundary conditions at the PDMS free end. The nickel rod will have forces applied to it through the magnetic field and viscous drag that need to be balanced out by the boundary conditions.

The first two boundary conditions are for the fixed PDMS end. These boundary conditions are simply:

$$w(0) = 0 \tag{4.34}$$

$$\frac{\partial w(0)}{\partial \alpha} = 0 \tag{4.35}$$

The boundary conditions on the nickel end of the PDMS are the applied moment and shear from the nickel portion of the rod. It is in these boundary conditions where the driving magnetic force and the drag terms from the nickel portion of the rod come in. Because the movement of the nickel end of the rod is entirely determined by the function w and its first derivative with respect to α at the end of the PDMS section, we are able to write out these boundary conditions as functions of w (Figure 4.5):

$$\frac{\partial^2 w(1)}{\partial^2 \alpha} = \frac{M_{app} L_p^2}{EI} + \frac{M_{drag} L_p^2}{EI} \tag{4.36}$$

$$\frac{M_{drag} L_p^2}{EI} = \gamma_1 w(1) + \gamma_2 \frac{\partial w(1)}{\partial \alpha} \tag{4.37}$$

$$\frac{\partial^3 w(1)}{\partial^3 \alpha} = \frac{S_{app} L_p^3}{EI} = \gamma_3 w(1) + \gamma_4 \frac{\partial w(1)}{\partial \alpha} \tag{4.38}$$

where M_{app} is the moment at the end of the rod, L_p is the length of the PDMS portion, M_{mag} is the applied magnetic moment, S_{app} is the shear applied at the end of the rod, and $\gamma_{1,2,3,4}$ are constants that represent the drag terms on the nickel portion of the rod that contribute to the moment $\gamma_{1,2}$ and the shear $\gamma_{3,4}$

Determining $\gamma_{1,2,3,4}$

To calculate the drag terms, we will use the same Oseen drag force for a slender rod, and the displacement of the nickel portion of the rod (Figure 4.5). Applying these two terms we get the following equation for the drag force per unit length on the nickel rod:

$$D_{ni} = \frac{i4\pi\omega\eta}{\ln(L_{tot}/2D)} \left(w(L_{PDMS}) + (s - L_{PDMS}) \frac{\partial w(L_{PDMS})}{\partial s} \right) \tag{4.39}$$

$$D_{ni} = \frac{i4\pi\omega\eta}{\ln(L_{tot}/2D)} \left(w(1) + (\alpha - 1) \frac{\partial w(1)}{\partial \alpha} \right) \tag{4.40}$$

where D_{ni} is the drag per unit length along the nickel potion of the rod.

If we substitute the drag term into the equation for the moment boundary condition 4.36, we get the

following equations.

$$\frac{M_{drag}L_{PDMS}^2}{EI} = \frac{i4\pi\omega\eta L_{PDMS}^2}{EI\ln(L_{tot}/2D)} \int_{L_{PDMS}}^{L_{tot}} (s-L_{PDMS})\left[w(L_{PDMS})+(s-L_{PDMS})\frac{\partial w(L_{PDMS})}{\partial s}\right]ds \tag{4.41}$$
$$= ik^4 w(1)\int_1^{L_r}(\alpha-1)d\alpha + ik^4\frac{\partial w(1)}{\partial \alpha}\int_1^{L_r}(\alpha-1)^2 d\alpha$$

by comparison to 4.36 we can now write γ_1, γ_2 as test:

$$\gamma_1 = ik^4\int_1^{L_r}(\alpha-1)d\alpha \tag{4.42}$$
$$\gamma_2 = ik^4\int_1^{L_r}(\alpha-1)^2 d\alpha \tag{4.43}$$

preforming the same analysis on the shear boundary conditions we get:

$$\frac{S_{app}L_p^3}{EI} = \frac{i4\pi\omega\eta L_{PDMS}^3}{EI\ln(L_{tot}/2D)}\int_{L_{PDMS}}^{L_{tot}} w(s)+(s-L_{PDMS})\frac{\partial w(L_{PDMS})}{\partial s}ds \tag{4.44}$$
$$= ik^4 w(1)\int_1^{L_r} d\alpha + ik^4\frac{\partial w(1)}{\partial \alpha}\int_1^{L_r}(\alpha-1)d\alpha \tag{4.45}$$

and γ_3, γ_4 equal:

$$\gamma_3 = ik^4\int_1^{L_r} d\alpha \tag{4.46}$$
$$\gamma_4 = ik^4\int_1^{L_r}(\alpha-1)d\alpha \tag{4.47}$$

Now all that is left is to solve the system of four equations for the four unknowns. This is a trivial task but quite messy. Some general comments about the solution: the term M_{mag} factors out of the solution fully, implying that the beat shape is the same regardless of the magnetic field at a given sperm number and the amplitude of motion is linearly dependent on the applied field. The solutions have a wavelength along the PDMS portion of the rod, k. As k gets large there will be more and more nodes along the PDMS portion of the rod, Figure 4.6.

4.7.4: Computational models

The analytical model above does not include some important parameters. It assumes that the post deflection is small, which is often true of the oscillations, but the oscillations are about an equilibrium deflection. It also neglects to include boundary effects from the floor of the PDMS or post-post interactions. To confirm that we get reasonable results even with these assumptions, we compared our results with a finite element model created in COMSOL. COMSOL is a finite-element simulation package that specializes in multi-physics problems, such as fluid-structure interactions. The computational model enables us to look at the flow generated by a single post or an array as well as the post motion.

The post is modeled as a single post in a box of fluid with zero pressure boundaries in the direction of the beat plane, Figure 8. The post is modeled as two materials with different elastic moduli, mimicking the PDMS and Nickel composite structure. The magnetic force is modeled as a sinusoidal force couple applied to the stiff nickel portion of the rod. The top bottom and sides of the box all are a no-slip boundary condition (Figure 8. For a full description of the COMSOL model see appendix 6.5.

Section 4.8: Model results

The analytical model built here reveals two important factors about our composite ASAP rods. First, the applied moment from the magnetic system factors out of the equation. This means that the beat shape is independent of the applied moment and that the applied field simply determines the magnitude of the beat shape. Second, the beat shape depends entirely on the ratio of the nickel to PDMS portion of the rod and k or the sperm number. Intuitively this makes sense. The Ni/PDMS ratio is proportional to the ratio of the forces on the stiff and flexible portions of the rod while the sperm number represents the ratio of the viscous forces to elastic forces on the elastic portion of the rod.

In Figure 4.6, example beats at a variety of sperm numbers are shown for a composite rod that has a 1:1 L_{ni} to L_{PDMS} ratio. At low sperm numbers, $Sp << 1$, the beat shape is symmetrical. As the sperm number increases, asymmetry in the beat shape begins to develop. At a sperm number of two, a clear asymmetry of the beat shapes develops. One interpretation of the sperm number is the wave length of the deflections along the rod (189). At larger values of the sperm number, i.e. four (Figure 4.6), multiple wavelengths develop in the flexible region of the rod. The number of wavelengths is proportional the sperm number.

In Figure 4.7, the phase between the driving force and the post response, measured as the angle formed by the nickel shell, is plotted against sperm number for a variety of nickel lengths. The amplitude as a function of sperm number is plotted as well. As the length of the nickel increases, the nickel drag dominates and the model approaches the simplified model of constant beat shape, dashed black line. Eventually at

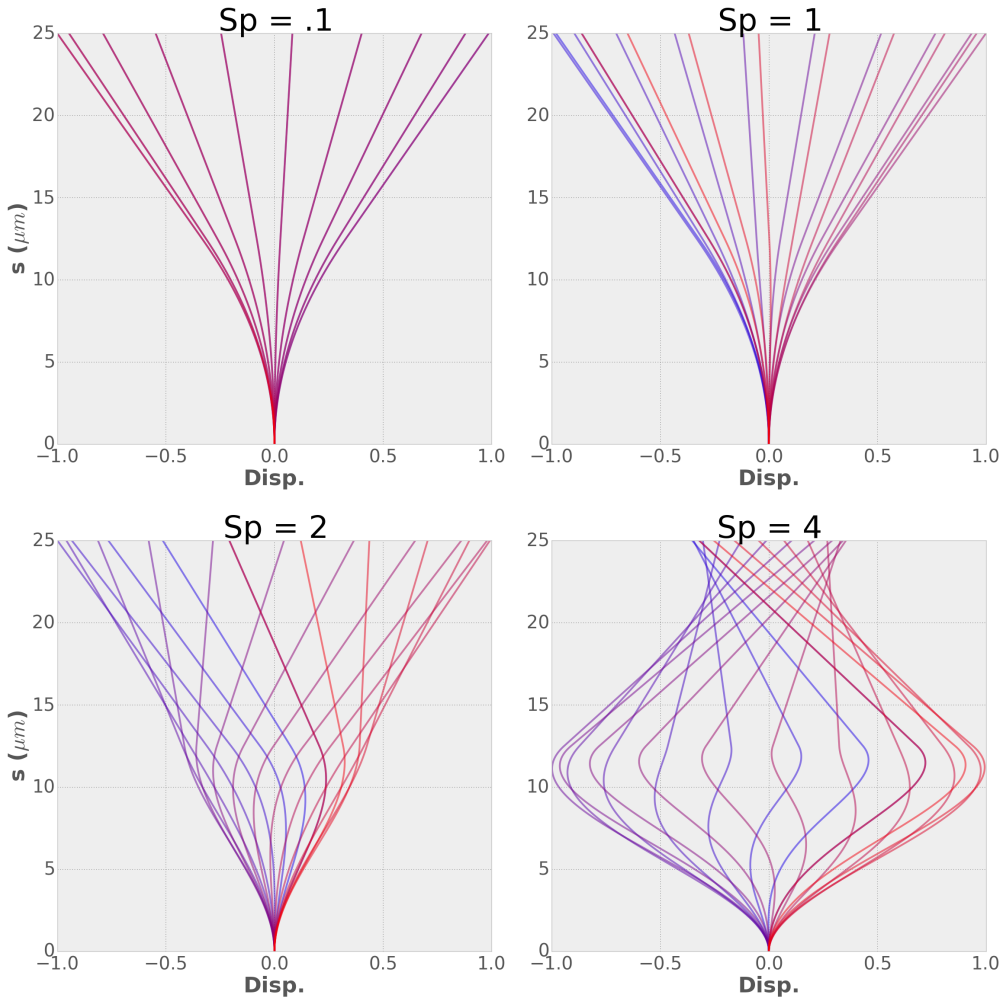

Figure 4.6: Examples of the normalized beat shape according to the analytical model at different sperm numbers. The normalized displacement from vertical is plotted on the x-axis while the distance along the arc length is plotted on the y axis. As the sperm number increases the drag becomes more and more dominant in the post motion. One full cycle of the beat is shown going from blue to read in time. As the sperm number increases the amplitude of the post motion also decreases, see Figure 4.7 B.

larger sperm numbers extremely large curvature begins to develop, causing the elastic forces to increase at a faster rate the drag forces which causes the phase to drop.

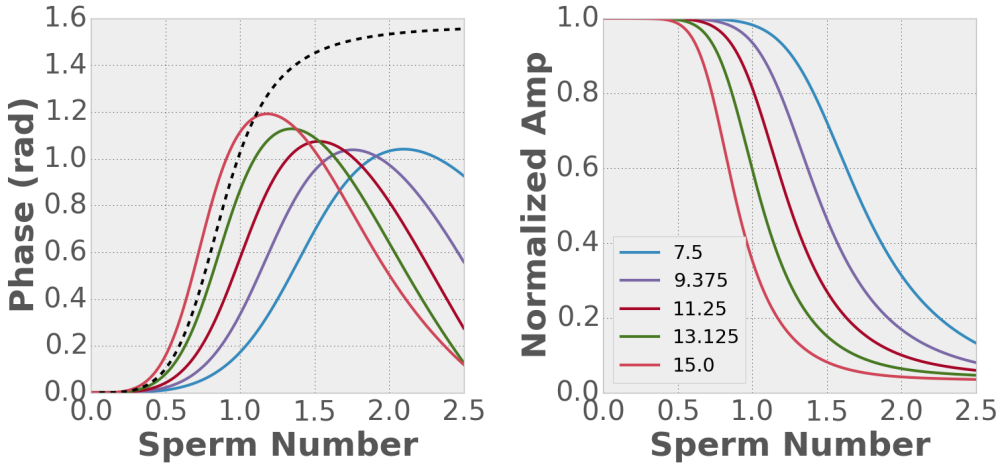

Figure 4.7: Plots of the models predicted post response to a oscillating magnetic field in phase and normalized post response. The left plot is the phase lag in radians plotted against the sperm number for different nickel lengths. The right plot shows the normalized post amplitude as a function of sperm number for the same nickel lengths. The ni-length in microns is varied for the same length of posts. All posts were 25 μm in length total. The black dashed line represents the naive model of the post with a constant beat shape.

At low sperm numbers there is excellent agreement between the analytical model and the COMSOL result, see Figure 4.8. As the sperm number increases, the discrepancy between the two models increases. This is particularly obvious in the predicted phase response of the posts, Figure 4.9. While both the COMSOL model and the analytical model begin decreasing phase as the sperm number increases for large sperm numbers, the analytical model overestimates this change compared to the COMSOL model. This indicates that the analytical model is overestimating the elastic component. The COMSOL model includes the effect of the floor boundary, and the fluid motion, and does not assume that the cross-section does not deform as the post bends. A lower bending rigidity to the posts would result in a larger phase lag as seen in Figure 4.8.

In an array of posts the fluid flow generated by neighboring posts is obviously important. In the later chapters, I will show that it is not necessary to take this effect into account to use the posts as sensors. The COMSOL model however shows that the posts generate significant fluid flow for their neighbors, Figure 4.10. In posts that are separated by 15 μm, the fluid velocity drops by less than 20% between the posts. This suggests that post-post interactions in our dense arrays, average spacing 5-6 μm, are extremely important. Future work should focus on understanding how these post-post interactions effect the analytical model.

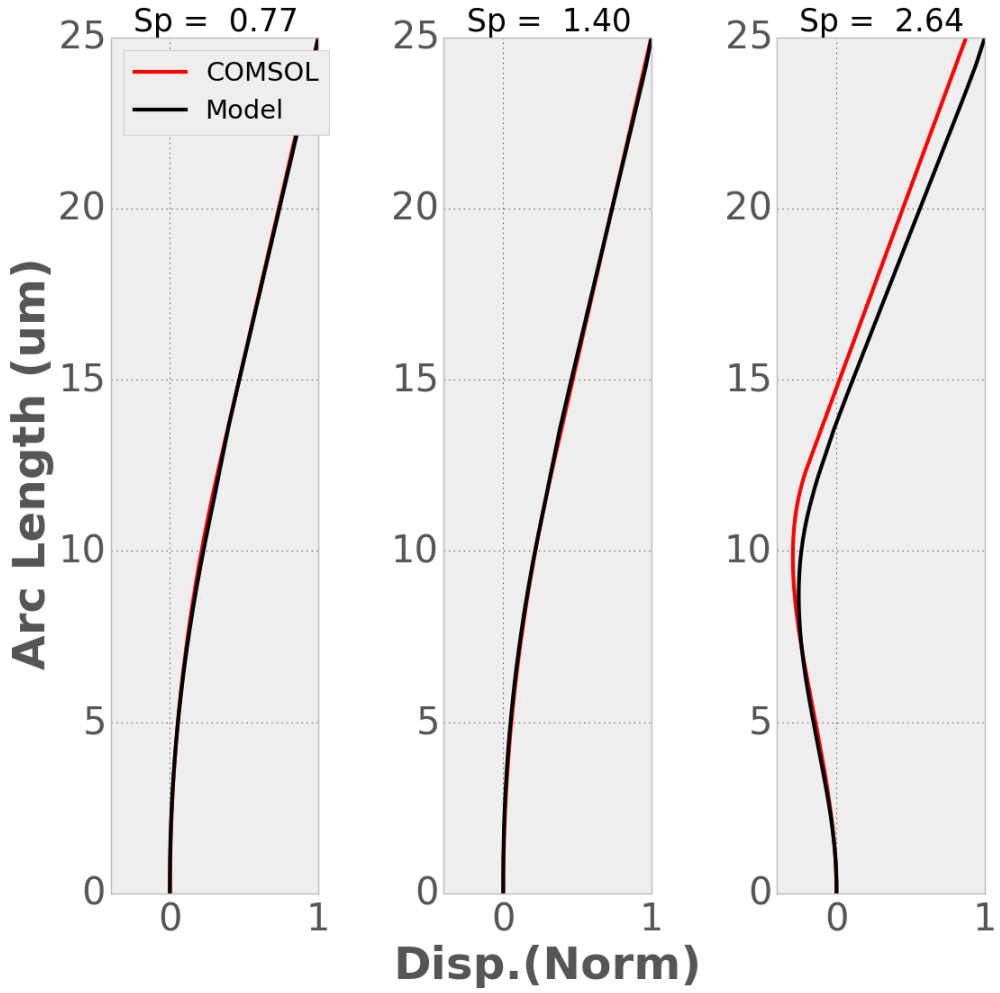

Figure 4.8: Example beat shapes at three different sperm numbers. The normalized displacement, x-axis, is plotted against the position along the rod, y-axis. The COMSOL simulation is in red while the black represents the analytical model. The figure above shows that there is excellent agreement between the two models. At larger sperm numbers, the discrepancy becomes larger.

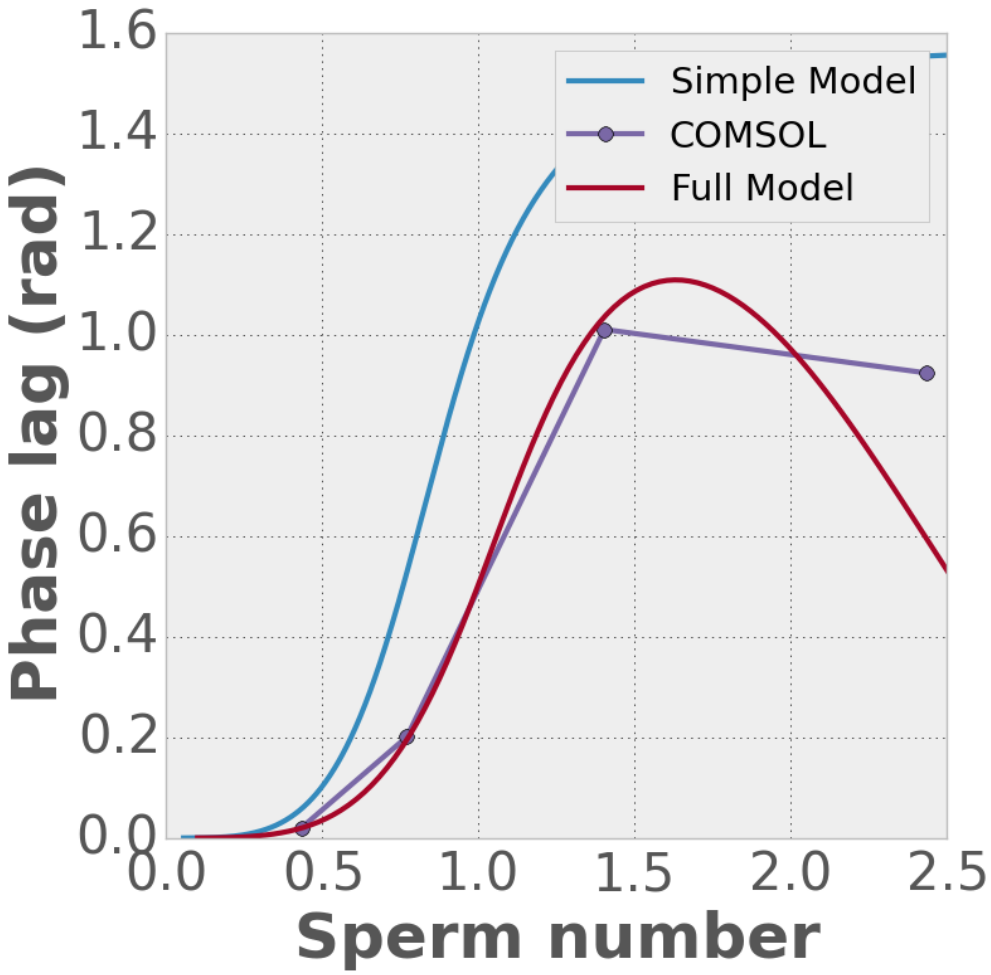

Figure 4.9: Plots of the phase lag of the post response vs sperm number for the naive model, blue, the COMSOL model, purple, and full analytical model, red. Below a sperm number of 1.5 the full analytical model and the COMSOL model give nearly identical predictions for the phase lag of the post response.

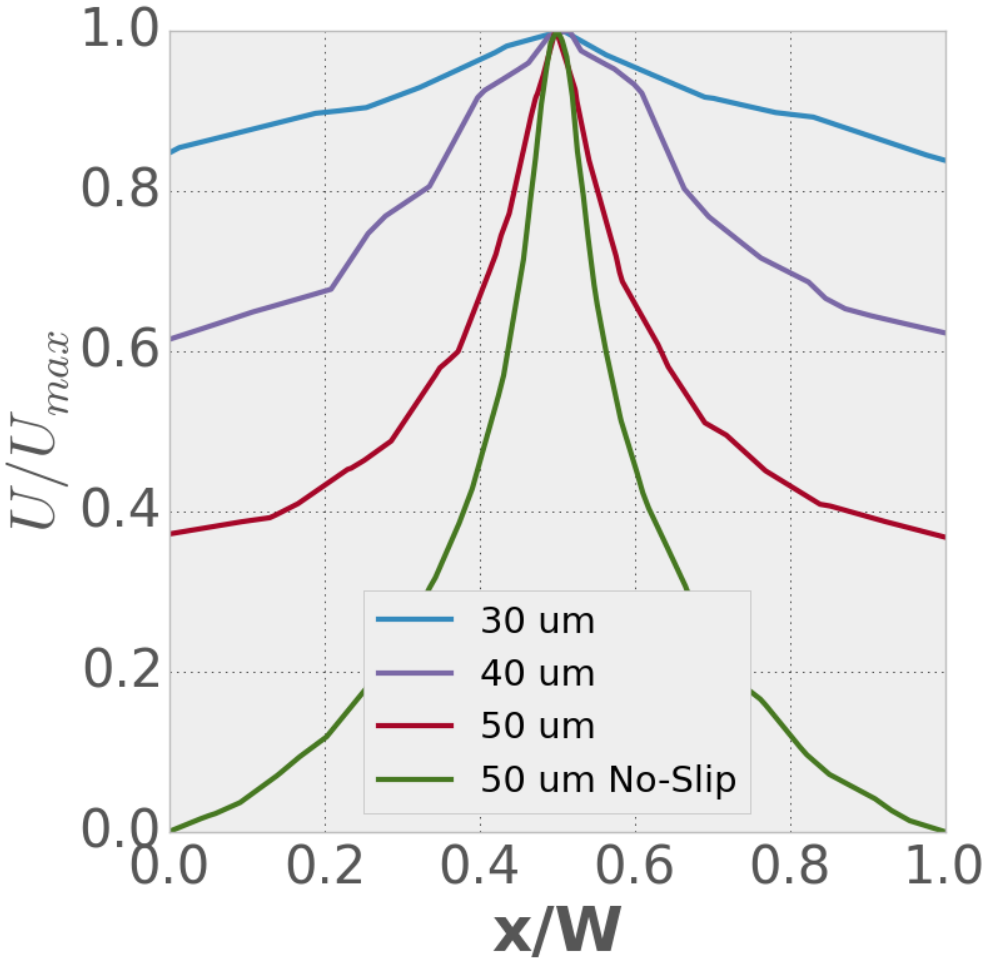

Figure 4.10: A plot of the normalized viscosity as a function distance from the post tip perpendicular to the beat plane. Different box sizes are shown, 30 μm, 40 μm, 50 μm, 50 μm no-slip boundary condition. The slip boundary condition is equivalent to an array of posts with a spacing equal to the simulation box width. The fact that velocity drops off by 20 percent over 30 μm suggests that there are strong post-post interactions.

Section 4.9: Conclusions and future work

In this chapter I developed an analytical model to convert the transmitted intensity signal into a post angle, the magnetic applied magnetic field into a torque, and an analytical model of a single post bending in fluid. The analytical model does not take into consideration the boundary of the floor or nearby posts. As will be shown in the next chapter this model works well as long as the sperm number of the system is below one, chapter 5. At larger sperm numbers the analytical model deviates from the experimental results significantly.

Future work should be using the COMSOL model in conjunction with the analytical tool for investigating the cause of this deviation. Previous modeling work of actuating arrays of posts show that there are significant changes in the flow around the post arrays as they transition through the sperm number of one (13; 108; 3). Particles will either be pulled into the cilia arrays or pushed out depending on the sperm number (13; 108). The flow in the channel reverses directions as the system passes through a sperm number of one (3). The COMSOL model developed in this chapter is an excellent model to investigate how the fluid flow changes between low and high sperm numbers and how this affects the model. Future work with should focus on understanding these effects.

On the analytical side there is the possibility of incorporating multiple posts and boundary conditions in the model. Under prescribed motions other groups have used slender body theory to model arrays of embryonic nodal cilia (158). In the model the nodal cilia have prescribed motions but the fluid flow and forces on individual posts are calculated. Using the current analytical model to calculate beat shapes, a similar model to the nodal cilia could be used as an alternate method to investigate the effects of post-post interactions.

CHAPTER 5: Oscillatory rheology

Section 5.1: Introduction

Rheology, the study of the mechanical properties of fluids, is important in biology and medicine (31; 37; 34). Conventional rheometers use relatively large volumes of material (hundreds of millileters) making studies of precious and novel materials difficult (131). Because of the need for rheometers that use small volumes of sample for biology and medical diagnostics, there has been significant interest in small volume rheology over the last 10 years. Additionally, there is a current push towards lab on a chip technologies that preform numerous tests or entire chemical production lines on a single chip, and there has been an increase in interest in micro-fluidic rheometers that can integrate into these systems (123; 198; 78; 29).

In this chapter, we describe a magnetically actuated micro-post array based rheometer. Quantitative viscosities over a range of three orders of magnitude are determined for samples of less than 20 μL with the aid of the comprehensive analytical model that includes post viscoelasticity, magnetics of the post, optical readout, and fluid structure interactions developed in chapter 4. In addition to sensing, these arrays are multifunction and are capable of pumping or mixing like previous arrays (151; 181; 168; 182; 83). We also show how the model can guide the design of new arrays with different physical parameters to expand the range of measurements.

In the last 10 years, there have been numerous papers on biomimetic cilia arrays and their potential applications for micro-fluidics applications. Like their biological counterparts artificial cilia arrays have been shown to be effective mixers, (151; 168; 83; 105) effective pumps, and can manipulate particle settling(108; 162; 6). These artificial cilia arrays operate in the low Reynolds regime and are typically on the scale of a few microns in diameter and tens of microns tall. Arrays have been created using a variety of techniques including using self assembled micro beads (182), magnetic polymer composites (151; 133), electrostatic and magnetic flaps (162; 196), and core shell structures (Fiser et al.). Considerable numerical and modeling studies have been done as well trying to understand the flow around post arrays (27; 105; 82; 3; 85).

Driven artificial cilia arrays, however, have not been successfully used as a fluid rheometer. We have used our nickel composite arrays as a sensor for the elastic properties of human blood clots (75), Chapter 6, but did not measure the viscous properties of the clot.

In this chapter, we use the model developed in chapter 4. By using high resolution time measurements

(10 kHz-bw) of the transmitted light through the post array, synchronized with the driving magnetic force, we are able to monitor the phase of the post drive to the post response (driven at 1-30 Hz). We show that while the single post model deviates significantly from the experimental behavior at large sperm number, at low sperm numbers we are able to use the model to measure the viscosity of the fluid. Using the model, we show how the post design can be modified to increase the range of fluids that fall into the slow sperm number regime. Our ASAP arrays are easily integrated into microfluidic systems, do not require active flow for rheology measurements, and are capable of being multi-purpose elements in lab on a chip devices.

Section 5.2: Methods

5.2.1: Making flow cells

PDMS channels were made by laser cutting negatives of the channels out of 250 μm transfer adhesive. The channel negatives were then attached to the bottom of a 100 mm petri dish. Micro-fluidic ports (Value plastics B000FP9YDO) were then mounted onto the transfer adhesive. PDMS (Sylgard-184) was mixed at a 10:1 PDMS:crosslinker ratio. The PDMS was poured over the channel negatives and allowed to cure at 80 $^{\circ}C$ overnight. The channels were then cut out of the petri dish using a razor. The channels were plasma cleaned for 30 seconds and coated with a thin layer of Norland optical adhesive and sealed onto the ASAP arrays, which were mounted on an 18×18 mm number one cover slip.

5.2.2: Electromagnet microscope setup

ASAP actuation was performed with an opto-magnetic system as shown in Figure 5.1. The posts were imaged using a 10x, 0.3 NA, Plan DL, Nikon objective mounted model number and a 60 Hz Firefly USB 2.0 camera (FMVU-03MTM-CS). The camera was interchangeable with a Thor Labs amplified photo diode (Thor Labs PDA36A). The diode has a 13 mm^2 detection area and is responsive from 250–1100nm light. The camera was used to take images of the deflected posts for calibration purposes, while the photo diode was used for measuring the deflection during the oscillatory experiments in phase with the magnetic field. A collimated 780 nm high intensity LED from Thor labs (Cat# M780L3), with a polycarbonate diffuser, was used as the light source. The noise level of the camera and LED system was less than 0.03% of the average image intensity. To actuate the posts, an electromagnet consisting of tape-wound, silicon-steel, C-shaped core with a 10 x 10 mm cross-section and a 16 mm gap was used. Magnetomotive force was produced by two magnet coils, with 680 turns each, connected in parallel for a total of 1,380 turns. The magnetic field varies less than 10% within 3 mm of the gap center, confirmed experimentally and with COMSOL simulations.

The electromagnet was driven by a transconductance amplifier. The amplifier and magnets had a combined bandwidth greater than 50Hz. The amplifier magnet combo was able to reproducibly produce a field within the 1% precision of the gauss probe used to measure the signal. The amplifier has a noise level as a function of frequency of approximately $\sqrt{1\text{nA/Hz}}$.

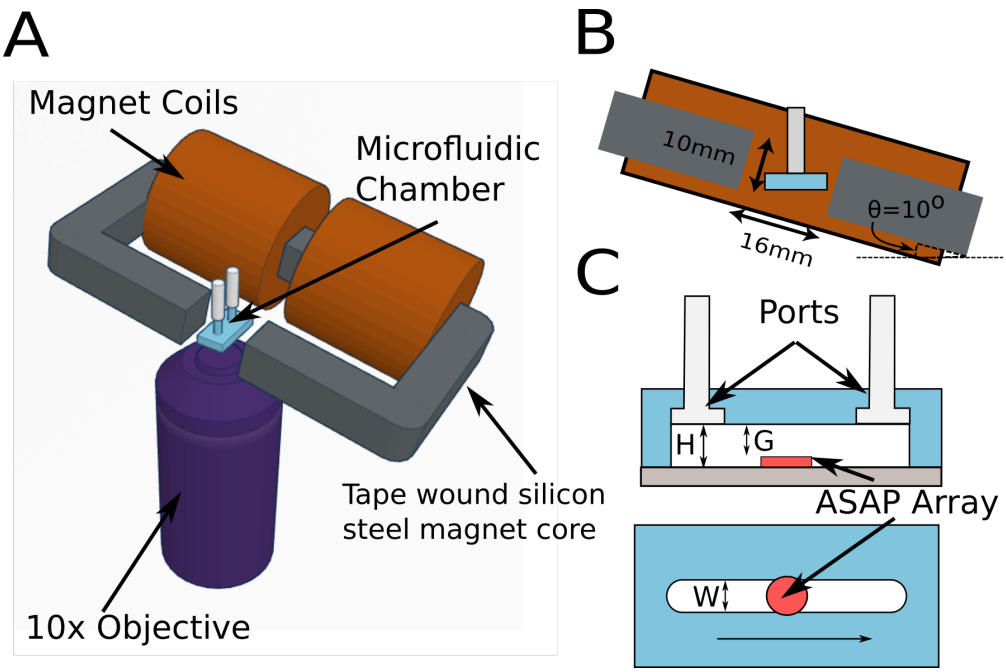

Figure 5.1: (A) Computer model of the experimental setup. The micro-fluidic channel is placed in between the C shaped electromagnet core and is imaged using the microscope. The intensity of the transmitted light from the light source, not shown, is monitored using either a camera or photo diode. B) Frontal view of the microfluidic chamber in between the magnetic field. The face of the electromagnet is 10×10 mm and the gap is 16 mm. The magnetic is tilted at a 10^o angle from the horizontal axis. C) A diagram showing the microfluidic chamber. The chamber has a height of 250 μm . The PDMS base and posts have a total height of 125 μm so that the gap height, G, between the top of the posts and the ceiling of the channel, is 125 μm . The channel is 1 mm in diameter.

5.2.3: ASAP rheology protocol

For an ASAP rheology experiment, the posts are subject to an oscillatory magnetic field. The field is an offset sine wave that goes from zero to a maximum and back to zero, never negative.

In order to calibrate the ASAP post post amplitude in different fluids with different indexes of refraction, a steady state experiment is performed. Because all the materials used are visco-elastic or viscous fluids, over long periods of time, the post deflection is determined entirely by the magnetic and material properties that remain constant. A known magnetic field is applied to the post array, and the posts are allowed to equilibrate. The change in intensity and images taken with the FlyCap camera at equilibrium are used to calibrate the tilt model (eq. 4.7). This allows us to measure accurately the amplitude in different materials.

A frequency sweep is then performed, typically from 1, to 30 Hz in 1 Hz intervals. At each frequency, the phase and amplitude of the post motion and the magnetic field is recorded, using a NI instruments DAQ board, PCI-6713. The magnetic field is read as the current being supplied to the magnetic field, and the intensity is monitored with the photo diode.

Section 5.3: Results

5.3.1: Raw results

The raw output of the experiment is the current as a function of time being delivered to the magnet, and the transmitted intensity through the post arrays as measured by the photo diode, Figure 5.2. The magnetic field can be directly calculated from the current, because the silicon tape wound core has low remanence, < 0.1 mT, and a bandwidth over 200 Hz, well above the maximum drive frequency (30 Hz). Because we drive the magnet below the saturation threshold, there is a strictly linear relationship between magnetic field and current.

Both the applied magnetic field and the transmitted intensity are converted into a post angle deflection and applied torque using the model developed in chapter 4 (Figure 5.2).

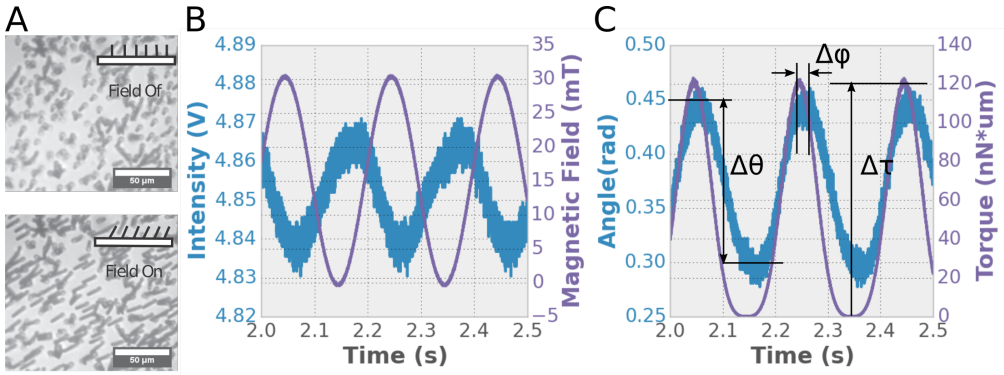

Figure 5.2: A) Example images of the post array with the field on and off. Images like this are used to calibrate the post deflection, measured directly using the images, and the change in intensity. B) Raw ASAP results. The magnetic field and the transmitted intensity are measured simultaneously using a DAQ board. The DAQ board measures the output voltage of the photo diode and the voltage across a 2 Ohm shunt resistor in series with the electromagnet simultaneously. B) The measured post angle and applied torque are calculated using the tilt and magnetic model explained in detail in chapter 4. From these results we get the post amplitude, $\Delta\theta$, torque amplitude, $\Delta\tau$, and the phase, $\Delta\phi$, between the drive signal and the post response.

From the processed results we can measure the change in post amplitude, $\Delta\theta$, the amplitude of the torque motion, $\Delta\tau$, and the phase between the two, $\Delta\phi$. We extract the these parameters by fitting the data with a sinusoid of the from:

$$A\sin(2\pi ft) + B\cos(2\pi ft) \tag{5.1}$$

where f is the drive frequency, t is the time, and A and B are fitting parameters. Because of the fact that the magnetic field goes as the square of the magnetic field, there will be higher frequency components in the drive signal and the response. However, by fitting the data with the sine specifically at the drive frequency we will suppress the higher frequencies from the data.

Because we will work with the model in the complex frequency space, the fitted torque data and post response will be converted into complex numbers:

$$\text{Amp}_{f=f_{mes}} = B + iA \tag{5.2}$$

which is the complex response of the posts at a given frequency.

5.3.2: PDMS calibration

The final step to complete the model is to calculate the material properties of the posts. To do this we will use the post response in water. In water, the PDMS material properties are dominant, so even if the drag model is not completely accurate, we should get a reasonable measure of the post material properties.

The complex elastic modulus of PDMS is calculated from PDMS by solving for the elastic modules in the model equation from chapter 4, using the phase and amplitude of the posts in water. The first derivative of the solution from chapter 4 of the post motion can be related to the post amplitude using the small angle approximation:

$$\left.\frac{\partial w(s,\tau(\omega),Sp)}{\partial s}\right|_{s=L_{pdms}} \approx \theta(\omega) \tag{5.3}$$

where $w(s,\tau,Sp)$ is the solution to the post model from chapter 4 which depends on the position along the rod s, the applied torque τ , and the sperm number Sp. The sperm number depends on the the viscosity η, the frequency f, the elastic modulus of the posts E, and the second moment of inertia I. The experimental results give us $\theta(\omega)$ and $\tau(\omega)$, and I, f, eta are all known. We solve for the sperm number using eq. 5.3 for the post arrays in water. PDMS is a partially cross-linked polymer, and therefore has complex visco elastic

properties and is represented as a complex number. Because the viscosity and frequency are determined, we are able to solve for the complex elastic modulus of the PDMS, see Figure 5.3.

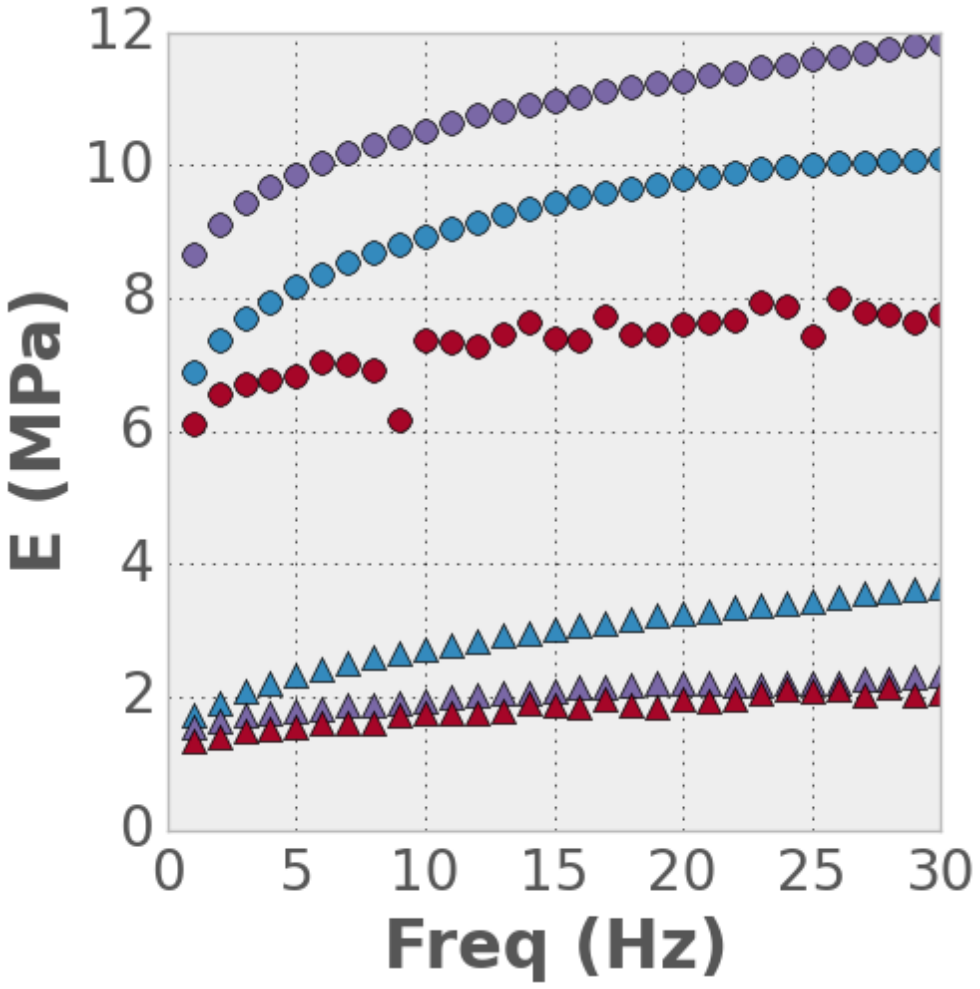

Figure 5.3: Plot of measured elastic modulus of the PDMS posts as a function of the drive frequency. The circles represent the real component of the elastic modulus of the PDMS, while the triangles are the imaginary part. These curves were calculated using equation 5.3 using water as the experimental fluid. The curve from three different ASAP arrays are presented.

The real elastic modulus of the PDMS ranges between 5-10 MPa, while the imaginary component, which is caused by free polymer chains, ranges between 1-3 MPa, Figure 5.3. The PDMS properties are not consistent across arrays and therefore each array needs to be calibrated for each experiment. While the PDMS properties measured are reasonable for PDMS (183; 43; 50), they are on the high end of the expected range and are nearly a factor of 10 higher than the PDMS properties measured in the tilt tests (Figure 4.4). It is likely that there are post-post interactions, and post-wall interactions occurring between the posts that are being included in the PDMS calibration.

5.3.3: Viscosity measurements

The calibrated results are plotted against the analytical model and a constant beat shape model in Figure 5.4. The phase is calculated between the drive and response signal using the fitted PDMS parameters in the model (Figure 5.2). The frequency response of the posts in water, where the drag force is five orders of magnitude below the post stiffness, is used to determine the PDMS properties, see section 5.3.2. The phase lag due to the visco-elastic nature of the PDMS are subtracted out.

In the ASAP system, we start to get strong deviation from the model at a sperm number of one (Figure 5.4). We can use the model to calculate the viscosity of the sample as long as we limit our results to sperm numbers below 1.0 (Figure 5.5). At low viscosity the uncertainty in the PDMS properties of our system becomes dominant and limits the systems accuracy. We get results within 50% of the true viscosity over three orders of magnitude (Figure 5.5).

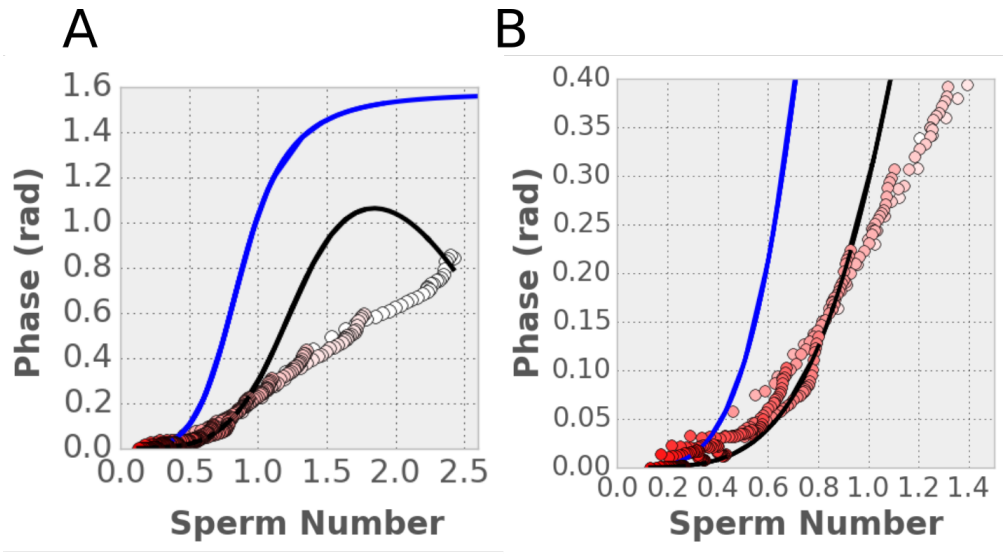

Figure 5.4: A) A plot of the models predicted phase lag between the post response and magnetic drive. The black curve is the full analytical model, while the blue curve is the simplified constant beat shape shape model. The experimental results are plotted as circles. Different viscosity fluids are different color circles going from red, water, to white, Karo, in increasing viscosity. The blue line represents a simple constant shape post motion and is both under representing the phase at low sperm number and over estimating the phase at high sperm number compared to the full model. At a sperm number near one, the full model, black deviates significantly from the experimental Results. B) Zoomed in of the results in the low sperm number range.

Section 5.4: Discussion

The ASAP system and our current model limits the range of viscosities that we can measure. At low viscosities the viscoelastic properties of the PDMS dominate and swamp the signal. At large viscosities

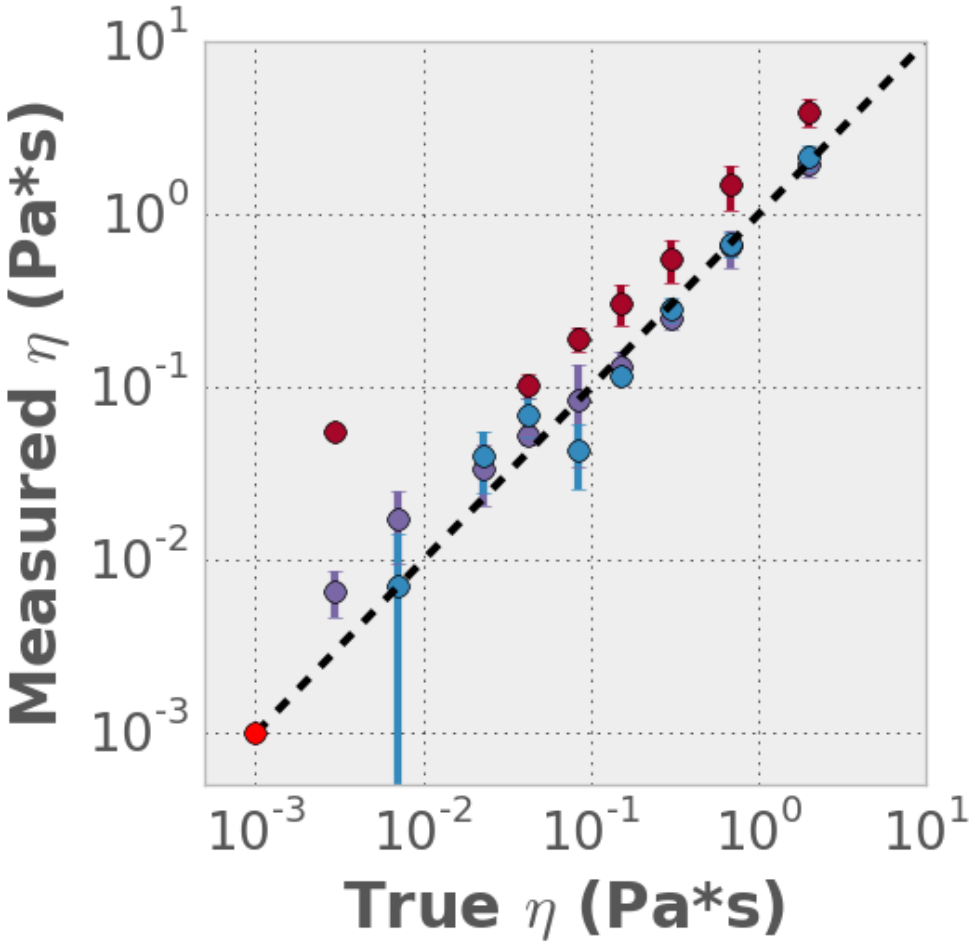

Figure 5.5: Correlation plot between the measured viscosity and true viscosity of sucrose solutions. Different colors represent measurements with different arrays. The true viscosity was measured using a cone and plate rheometer, while the measured viscosity was calculated using the frequency sweep of each sample but only using conditions with a sperm number below one. Water, bright red, was used as the calibration fluid.

the arrays enter the large sperm number, $Sp > 1$. At large sperm numbers our model breaks down and the experimental results deviate. This deviation at a sperm number of one is interesting because, previous computation studies of driven post arrays have shown that a $Sp = 1$ is a critical number. At a sperm number of one the direction of generated flow reverses in the computer simulated post arrays (3). It is intriguing that the deviation from experimental results occurs at this number and suggests that the deviation could be caused by a change in the flow dynamics in the chamber that invalidates the single post model or the calibration that was preformed at low sperm number. Computational work shows that the flow direction reverses as the the sperm number of an array of posts travels through one (3).

It is possible that the PDMS calibration is including post-post interactions. Flow is typically viscosity and frequency independent in the low Reynolds number regime. We calibrate for PDMS properties using the post response in water, which may account for the post-post interactions. These interactions may explain why we measure PDMS properties on the high end of the range. As the posts transition across a sperm number of one, this calibration may become invalid as the flow in the channel fundamentally changes.

The limit of a sperm number of one for our results limits the experimental range of the system, shown in Figure 5.6. It is possible to design the post arrays to bring the sperm number into the valid range for any viscosity. The simplest and most direct way to adjust the post properties is by adjusting the aspect ratio of the PDMS section. The sperm number, equation 4.1, has two geometric parameters, $L_{PMDS}$and I. $I = \frac{\pi r^4}{4}$ for a cylinder, so the sperm number scales linearly with the aspect ratio of the PDMS region to the post radius. At low viscosities, the uncertainty in the PDMS measurement becomes the limiting factor. Uncertainty in the PDMS measurement swamps the phase signal.

The sperm number also depends on the frequency. This gives us a simple way to adjust the design of the ASAP post arrays to enable measurement of higher or lower viscosity samples, see Figure 5.6. For the design of the ASAP arrays, we are limited by ground and lateral collapse (48; 136). The phase accuracy scales with the number of cycles measured, and at low frequencies the only limitation is a practical limit on the experiment time. The maximum frequency we can drive the posts is 200Hz due to the bandwidth of the silicon steel tape wound core.

Section 5.5: ASAP arrays for shear thinning fluids

ASAP arrays could have potential applications in shear thinning fluids such as mucus. Given our experimental setup we can approximate the maximum shear that we can produce. If we model the tip of the post as a 2 μm sphere we can easily use the equation for the shear around a bead derived from the equations for stokes flow around a bead (33).

$$|\dot{\gamma}| = \frac{3v_s}{\sqrt{2}r_s}, \tag{5.4}$$

where r_s is the radius of the sphere, or post in our case, and v_s is the velocity. The velocity at the tip of the post is:

$$v_{tipmax} = 2\pi\theta_{max}L_{post}f \tag{5.5}$$

where f is the drive frequency of the posts, $\theta_{max}$is the max post deflection, and $L_{post}$is the total length of the posts. Combining the equations we get the following equation for the tip shear.

$$|\dot{\gamma}| = \frac{2\pi 3\theta_{max}L_{post}f}{\sqrt{2}r_s} \tag{5.6}$$

Plugging in reasonable a post amplitude of 10 degrees at 30 Hz, we have a shear rate on the order 10^3 $1/s$, which is plenty to induce shear thinning behavior in biological samples such as mucus and blood that have significant shear thinning at shear rates below 10^3 $1/s$.(89; 8)

The actuating post arrays are an interesting potential platform to study mucus because the the ASAP arrays are capable of measuring rheological properties in a way that directly mimics biological cilia in the airway. Rheology of non-homogeneous samples such as mucus can vary as a function of the scale and the actuation mechanism (89; 38).

The current post arrays are not stiff enough to effectively measure mucus at the high ranges of the viscosity found in mucus while remaining in the low sperm number regime. This could be adjusted by changing the aspect ratios of the posts (Figure 5.6). Posts that have twice the diameter and are 3/4 the length of our current ASAP arrays could measure mucus rheology properties while remaining within the one sperm number limit.

Section 5.6: Conclusions and future work

The post arrays have a number of unique advantages. They are easily integrable into micro-fluidic devices and do not require flow reducing the amount of fluid necessary for experiments. The beat shape used for the rheology measurements could be used for pumping as well (3), allowing for a single array to simultaneously

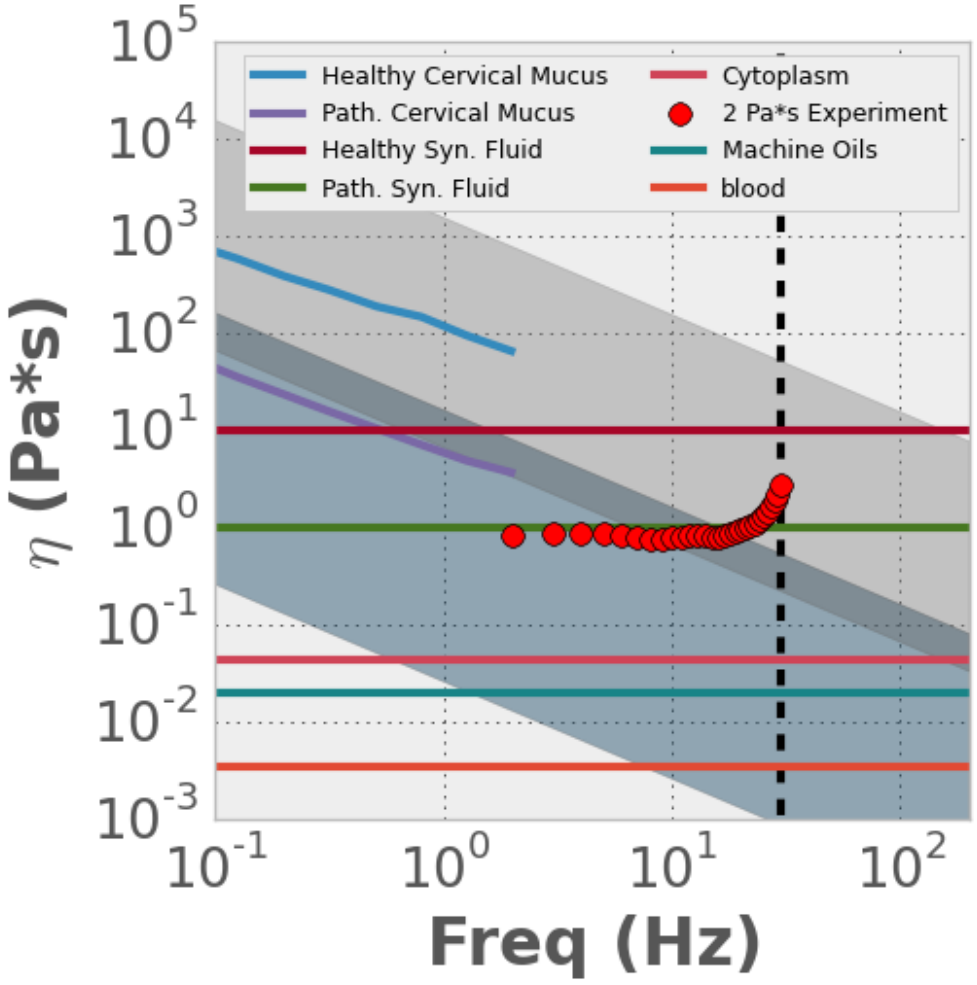

Figure 5.6: Plot showing the experimental range of our current experimental set up, dark gray shaded area, and a proposed alternate design with a 3 um radius and and a nickel shell that is 3/4 the length of the rod, light-gray. Colored lines represent sample fluids that may be of experimental interest using our ASAP system (31; 34; 19; 146; 88; 79). The black dashed line is the frequency limit of our amplifier.

generate fluid flow and measure the rheological properties of the fluid. For mixtures that change the viscosity of their parts as they mix, it could be used as a both a mixer and a measure of the level of mixing. Or the the same element could monitor the viscosity of the system while acting as a pump in a microfluidic system. ASAP post arrays have now been shown to be both effective elastometer (75) and viscometers.

The next step with the post arrays is to apply the ASAP technology to visco-elastic samples. We have performed initial experiments driving the posts in PEG solutions, which show considerable different post behavior than the viscous solutions (Figure 5.7). Despite the large difference in viscosity between the PEG (blue) and the 2.4M sucrose purple, the torque required for both systems is similar. This may be due to increased coupling between the posts due to the visco-elasticity of the PEG solution. In the phase signal, the 2.4M and PEG phase responses cross over in the 20Hz regime, which is unique for that sample. This preliminary experiment suggests that the posts behave differently in visco-elastic materials. As such, further work needs to be done on the model and analysis to effectively use the posts in these materials.

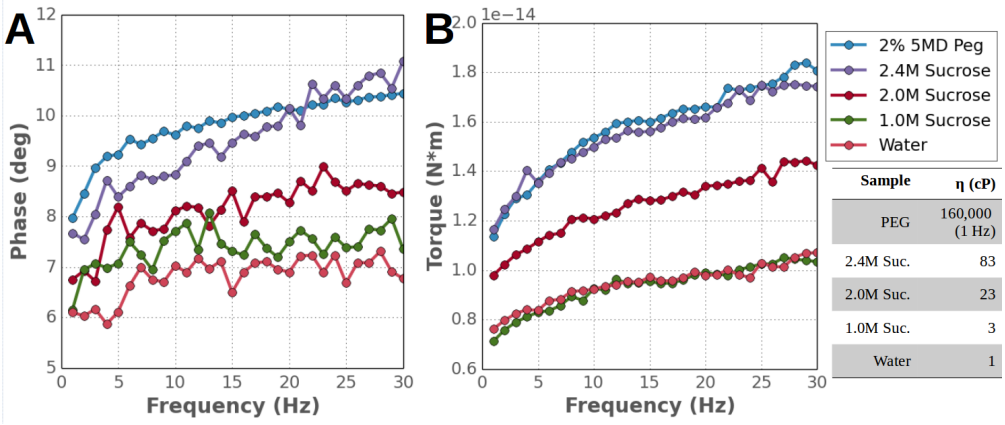

Figure 5.7: (A) The phase difference between the drive force and the post angle as a function of frequency in different materials. Because the posts have an elasticity the phase lag of viscous materials is not 90 degrees. (B) Torque as a function of frequency in different fluids. The amplitude of oscillation was maintained across all frequencies using a feedback loop. As the viscosity of the fluid increases the torque required increases. It is interesting to note that while the PEG and the 2.4M sucrose have similar amplitude responses as the PEG, which is a visco-elastic fluid, despite the dramatically different viscosities. The PEG and the 2.4M sucrose cross-over at 20 Hz which does not happen between any of the Newtonian fluids.

CHAPTER 6: Blood clotting

Section 6.1: Blood diagnostics

Rheology is used throughout industry and academic research to study a wide range of materials, from the mouth-feel of ice cream (167) to the mechanics of individual cells (86; 190). However, typical rheometers require large specimen volumes, extensive preanalytical processing, and highly-trained operators. The last two decades have seen the emergence of micro-rheology, the field of small-volume visco-elastic measurements (178). Micro-rheology has been dominated by micro-bead rheology, but new microfluidic devices and micro-cantilever technologies have also been developed (78; 198; 58; 59; 20; 9; 138). Lab-on-a-chip rheometers simplify data collection and expand the reach of viscoelastic measurements. Potential applications exist in medical diagnostics, process monitoring in manufacturing, and field environments.

Numerous microfluidic systems have been shown to successfully characterize viscoelastic materials. Many rely on a flowing fluid (198; 78), which are not appropriate systems for materials that are primarily elastic. However, these systems have had success in measuring changes in visco-elastic properties of whole blood (78), but are not suitable to measuring the elastic properties of blood clots. Passive (58; 59; 20) and resonant (9; 138; 78) techniques have measured viscoelastic fluids using micro-scaled beams. However, these techniques have very high operating frequencies (10^2–10^4 Hz), limiting their utility when the specimenâĂŹs low-frequency modulus is of interest. In this chapter we demonstrate qualitative elastometry using an array of ASAP arrays. In this chapter, I show that by monitoring the post-motion while controlling the applied torque, we can measure the elastic properties of a blood clot as it forms. The ASAPs are magnetically actuated, and their tilt angle is detected by optical transmission. The physical dimensions and number of posts per unit area is tightly controlled to allow consistent results across different ASAP elements. Aside from the micro-posts themselves, the system has no moving parts or fluid pumps.

ASAP technology could enable elastic measurements in a wide range of natural and synthetic materials. Here we focus on the application of ASAP to the *in-vitro* testing of blood coagulation and specifically on a novel micro-fluidic implementation of a viscoelastic hemostatic assay (VHA), Figure 6.1. VHAs are a type of *in vitro* diagnostic test for blood coagulation that measures over time the stiffness of a blood clot as it forms(or clotting) inside a chamber. It has been shown that VHAs such as thromboelastography (TEG) can guide transfusion therapy (160; 159) and may diagnose other acute bleeding conditions such as trauma-

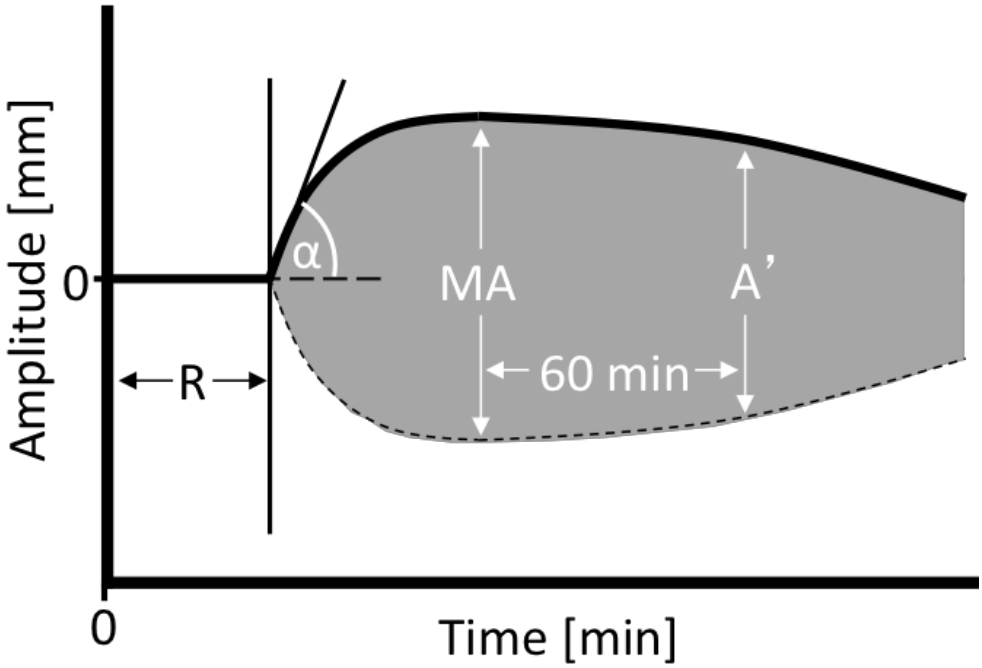

Figure 6.1: A thromboelastography (TEG) test qualitatively reports the life-cycle of a clot as a tuning fork-shaped curve. In addition, it reports quantitative parameters regarding coagulation kinetics and clot stability, such as the time to begin forming a clot (R), the clotting rate (α), clot stiffness or maximum amplitude (MA), and clot lysis or dissolution (AâĂŹ).

induced coagulopathy (106; 90; 80; 24; 127). VHAs are distinct from traditional coagulation tests, which measure the kinetic activity of the pro-coagulant cascade, often in platelet poor plasma. By contrast, VHAs measure clot initiation, formation, mechanical stability, and lysis in whole blood. The result is a global view of a patient's overall hemostatic function, from which clinical insight can be gained, as shown in both preclinical (90; 106) and clinical studies (80; 24; 127; 80).

Trauma centers increasingly use treatment algorithms that include hemostasis testing based on elastometry (144). These algorithms improve survival (74) and reduce costs by limiting blood product use (160; 159; 166). Surgical suites see similar benefits (187). While VHAs provide valuable clinical insight, they suffer from the typical issues that affect rheometers. In the clinic VHAs suffer from standardization, portability and usability issues (129). In the scientific community, VHAs use large volumes of blood (up to 1 mL), which make non-terminal studies on mice difficult. Ultrasound based methods for measuring clot properties are available but, like conventional VHAs, use large volumes of blood (400 μL or more) (52; 177; 109). Clot elasticity can be measured in smaller volumes (150 μL) using acoustic spectroscopy with optical vibrometry (RASOV), but the technique currently does not perform kinetic measurements such as clotting time(194). Here we report on a novel technique for measuring the time dependent elastic properties of micro-liter quantities (20 μL) of material and demonstrate its utility as a blood coagulation diagnostic

tool.

Section 6.2: Methods

6.2.1: Experimental setup

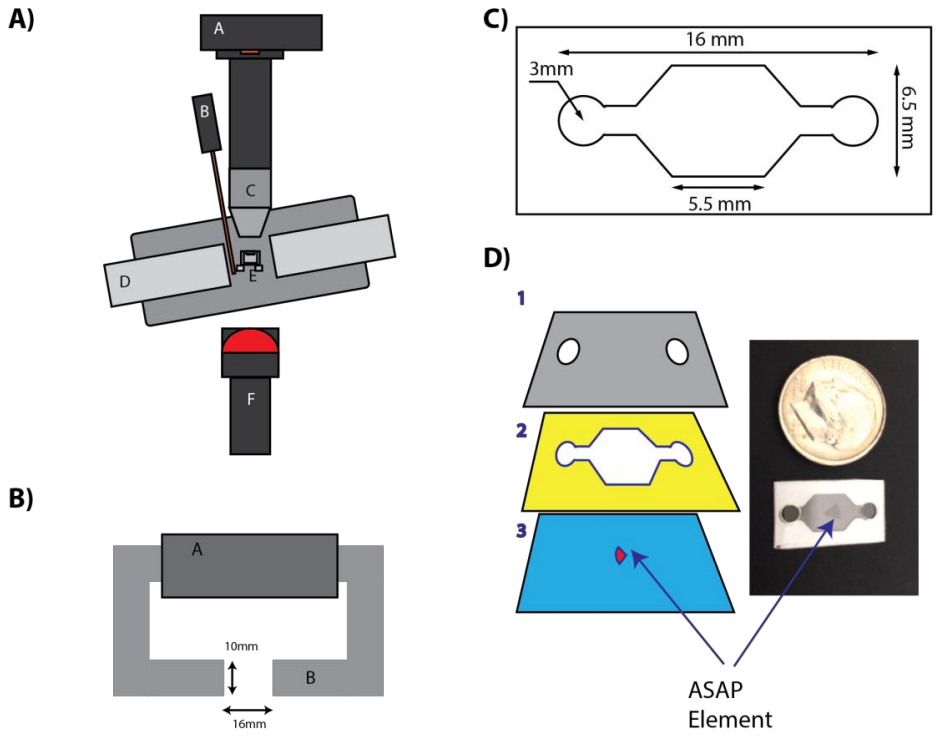

Figure 6.2: A) Diagram of the experimental setup, where: A is the 120 fps Pulnix camera; B is a gauss probe; C is a 10x Plan Nikon lens; D is the soft iron electromagnet; E is the heated holder for the ASAP element; and F is the diffuse near-infrared LED. B) Top down view of the electromagnet. A is the magnetic coil, and B is a silicon steel tape wound core. The gap is 16 mm wide and the faces are 10 by 10 mm. C) Diagram of the microfluidic chamber used for the blood experiments. The entire channel is 200 μm tall. D) A schematic showing the layers used in constructing the micro-fluidic chamber, where: 1 is a mylar top with air vents cut out; 2 is an adhesive spacer that defines the chamber dimensions; 3 is a #1 18x18mm coverslip with the post array mounted in the center. These layers are adhered to produce the final device as shown in the bottom-right.

ASAP actuation was performed with an opto-magnetic system as shown in Figure 6.2. The posts were imaged using a 10x, 0.3 NA, Plan DL, Nikon objective mounted 160 mm from a Pulnix TM-6710CL (648x484 pixels) camera, capable of up to 120 frames per second. A collimated 780nm high intensity LED from Thor labs (Cat# M780L3), with a polycarbonate diffuser, was used as the light source. The noise level of the camera and LED system was less than 0.03% of the average image intensity. To actuate the posts, an electromagnet consisting of a soft iron C-shaped core with a 10 x 10 mm cross-section and a 16 mm gap was constructed. Magnetomotive force was produced by two magnet coils, each with 680 turns, connected

in parallel for a total of 1,380 turns. The magnetic field varies less than 10% within 3mm of the gap center, confirmed experimentally and with COMSOL simulations. The electromagnet was driven by a transconductance amplifier (49). The amplifier and magnets had a combined bandwidth greater than 50Hz. The amplifier magnet combo was able to reproducibly produce a field within the 1% precision of the gauss probe used to measure the signal. The amplifier has a noise level as a function of frequency of approximately $1\ \sqrt{nA/Hz}$.

The transconductance amplifier was driven by a NI-Instruments PCI-6713 analog output board with 12-bit resolution over the range -5 to 5 V and 1 MS/s update rate, using custom software written in MATLAB. The output DAQ has a reported absolute accuracy of 7 mV. The dominate uncertainty, by an order of magnitude, in the magnetic field is in the uncertainty in registering the ASAP array with respect to the magnetic field.

6.2.2: Blood sample preparation

Human venous blood was collected from healthy consenting volunteers using butterfly needles (BD Vacutainer, BD Safety-Lok, Cat # 367283BD, Franklin Lakes, NJ) and stored in 4.5 mL citrated tubes (BD Vacutainer, Buffered Cit. Na., Cat # 366415), and kept at 22 ℃.ÂăBlood sample procurement protocols were approved by IRB of theÂăUniversity of North Carolina at Chapel Hill (IRB # 12-1592). Blood samples were used within 24 hours of collection and run as split specimens on the ASAP system and a TEG 5000 analyzer (Haemonetics, Inc). For the dilution experiments, isotonic saline (0.90% w/v NaCl) was added to the blood and mixed by gently inverting the tube.Âă Streptokinase, purchased from Sigma-Aldrich (product # S3134-10KU), was diluted to a final concentration of 9.6 U/ml for the high dose lysis experiment (Figure 6.3, blue circles) and 1.2 U/mL for the low dose lysis experiment (Figure 6.3, green squares). Immediately prior to data collection, all specimens were re-calcified by adding 1 μL of 0.2M CaCl2 per 17 μL of specimen volume. A 20 μL droplet of blood was pipetted onto the opening of the micro-fluidic device, and the blood wicked into the channel. The specimen volumes for the ASAP and TEG systems were 20 μL and 360 μL, respectively. The TEG was run according to standard operating procedures.

6.2.3: SEM sample prep

Clotted specimens for SEM imaging were harvested from micro-fluidic devices approximately 45 minutes after the initialization of clot formation. At that time, the top half of the flow cell was removed to expose the clot and the ASAP array. The sample was then fixed by adding 4μL of 0.2% glutaraldehyde directly onto the array and incubating at 37 ℃and 100% humidity for 30 minutes. The water in the sample was

serially diluted in mixtures of increasing ethanol-to-phosphate buffered saline, ending in 100% ethanol. The sample was critical point dried, then sputter coated with 7nm of 80:20, Au:Pd before imaging in a Hitachi S-4700 scanning electron microscope (SEM).

6.2.4: ASAP actuation and analysis

An initial field of 10 mT was applied to the posts, and the post response was measured. The magnet was then turned off, and the posts returned to their initial upright position. This on/off pulsing was repeated. As the blood clot formed and restricted the post-motion, the deflection of the post would decrease if the applied field were held constant. Instead, we used discrete-time proportional feedback control of the magnetic field to maintain constant post deflection during the magnet-on periods throughout clot formation. The feedback maintained a constant ratio of mean image brightness between the magnet-on and magnet-off conditions by controlling the magnet drive current. The set point was determined (as described above) by the initial response of the posts. The gain was set to maximize responsiveness without inducing instability. The use of the ratio of the two most recent magnet-off and magnet-on image intensities made the system insensitive to slow changes in overall image intensity (which can be induced by increasing turbidity during clotting). This assumed that the overall intensity is proportional to the product rather than the sum of the contributions of the post deflection and the overall clot intensity. We hypothesized that the nickel posts acted like a shutter below the blood clot, blocking a percentage of the light depending on their deflection (Figure 5.2), which was consistent with the multiplicative assumption.

The field required to maintain the post deflection was a measure of the mechanical resistance of the post/clot system. Because the mechanical properties of the posts remained constant over the course of the experiment (see Figure 6.3 blue curve) the change in applied field represented a change in the clot stiffness. The maximum applied magnetic field is similar to the maximum amplitude measurement in a TEG system.

As a reference instrument, a TEG 5000 Thromboelastograph Hemostasis Analyzer from Haemonetics was used. Blood samples were run on the TEG according to standard operating procedures provided by Haemonetics.

Section 6.3: Results

In the system described above, a force is applied to the blood by the posts through an applied magnetic field. Converting this applied field to an applied force requires a model of the magnetic response of the posts, which was developed in chapter 4.

The torque on the posts is calculated using the model of axial symmetric soft magnetic bodies described

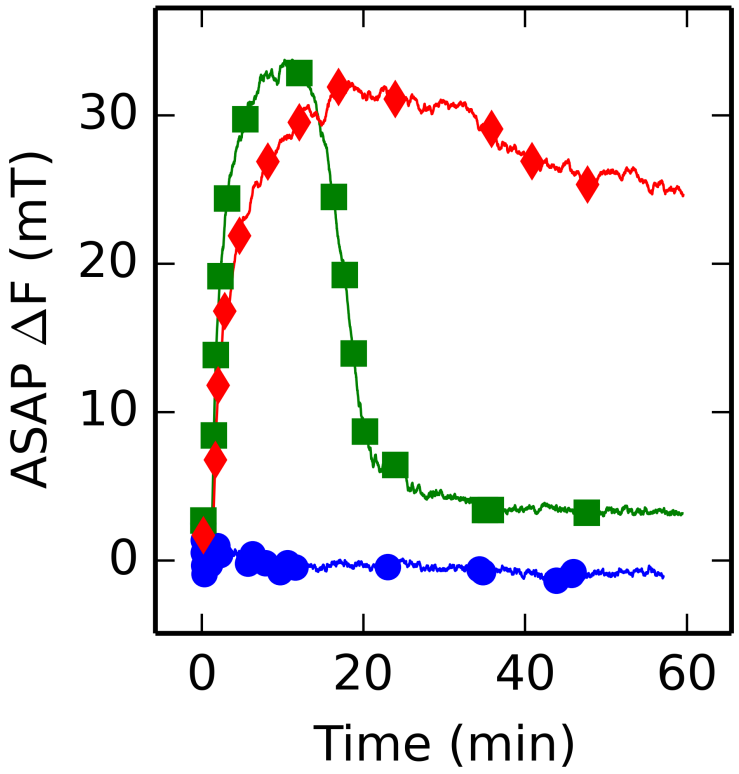

Figure 6.3: Coagulation measurements performed by ASAP arrays. Results are reported as magnetic field (mT), which is related to clot stiffness through equation 4.18. Three specimens are shown: normal blood (red diamonds), blood spiked with a low streptokinase concentration (green squares), and blood spiked with a high streptokinase concentration (blue circles). Streptokinase interference provides a model of clot lysis. In low dose, the clot forms normally before collapsing. In high dose, the clot never forms, resulting in a flat curve.

in Abbott et al. (1). According to this model, as long as the magnetic susceptibility is large, $X >> 1$, the induced moment is dominated by the geometry of the post. COMSOL modeling and experiments on the magnet setup suggests that the gradient terms in the post region are negligible. Using the Abbott model without the gradient term, the torque on the magnetic posts is described using the model developed in chapter 4.

Assuming the absence of a surrounding material (such as blood), deflections were calculated numerically using the quasi-static assumption and solving the torque balance equation between magnetic and deflection torque contributions, eq. 4.17. Because the magnetic field applies a pure torque, it is assumed that the PDMS portion of the posts bends with a constant radius of curvature. This has been shown to introduce an error of less than 30% (46). For material properties, the elastic modulus of PDMS was fitted to be $0.85 \pm .07$ MPa (50) and the permanent moment of the rod was fitted to the measured post response (see below). The fitted permanent moment of the nickel shell was $(4 \pm 1) \times 10^{-13} Am^2$. The predicted deflection of the posts can be seen in Figure 4.4.

6.3.1: Demonstration of ASAP as a VHA

In a standard VHA measurement, clot stiffness vs. time is plotted, and the clotting time, clot stiffness, and lysis are extracted from the curve shape. In TEG, a cup and bob style rheometer, the clot stiffness is plotted as the amplitude of rotation of the inner bob over time for a constant cup rotation amplitude. In the ASAP system, the magnetic field is pulsed on and off, and the post deflection is monitored. As the clot forms around the posts, the posts deform the clot as they deflect. Feedback is used to maintain a constant post deflection by increasing the magnetic field. The blood clot experiences shear, compressive, and tensile stress because of the post-motion. The readout of the ASAP system is the required magnetic field as a function of time. We studied the ASAP systemâĂŹs ability to detect coagulation and lysis of normal whole blood, with and without streptokinase, a known mimic for hyperfibrinolysis (90) (Figure 6.3). The forming clot restricts the post motion such that the feedback loop increases the applied field to maintain a constant deflection. The normal blood shows a sudden increase in the applied field, indicating the clotting time (called R time in TEG). As expected, normal blood does not show lysis over the course of 30 minutes, in contrast with blood dosed with streptokinase. At low streptokinase concentration, the clot forms normally, but subsequently breaks down, as shown by the drop in applied field. We note that this demonstrates that ASAP is a reversible elastometer: it can measure both increases and decreases in stiffness. Blood with high-dose streptokinase never clots, as indicated by the unchanged applied field over the course of the experiment, and as confirmed by TEG.

ASAP system noise is 0.1 mT, calculated by subtracting a smoothed curve (moving average with a one minute window) from the raw data, and taking the standard deviation of the resulting signal. The maximum error signal seen in the feedback loop is 0.3%. The two largest limitations on the devices precision are the applied field, and post material properties. Posts have variations in magnetic response are up to 20% between post arrays (Figure 4.4) and are the single largest limitation on the instruments precision. We suspect that the main source of variability in ASAP properties is the geometry of the nickel shell, which could be made more consistent by implementing the electro-deposition process in a higher-quality system.

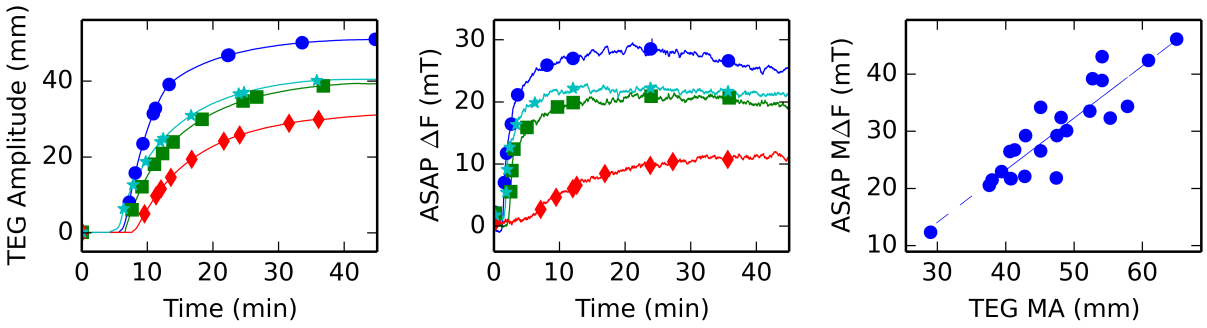

Figure 6.4: Serial dilutions of blood were used to modify clot stiffness and compare the Haemonetics TEG 5000 with ASAP measurements using split specimens. A) Output of TEG on representative blood samples: normal blood (blue circles), 33% dilution (cyan stars), 50% dilution (green squares), and 66% dilution (red diamonds). Note the noiseless curves, which are the result of intense smoothing by the TEG software. B) ASAP results for the same four specimens show the same features seen in TEG: as dilution increases, clotting time are rate are slightly reduced, while clot stiffness is dramatically reduced. No smoothing was applied to the ASAP results. C) ASAP and TEG systems show excellent correlation ($r = 0.91$). Clot stiffness is plotted on the x-axis in TEG maximum amplitude and on the y-axis in terms of ASAP maximum applied field. The consistency across platforms is surprising given that the ASAP system has a much higher surface area to volume ration than TEG.

To compare ASAP and TEG measurements, we performed serial dilutions of normal blood with saline. In both ASAP and TEG systems (Figure 6.4), clot stiffness varies with dilution as expected. The primary effect of increasing dilution is a drop in maximum clot stiffness, along with slightly delayed clotting initiation and a slower clotting rate (90). All of these features are apparent in both the ASAP and TEG results. Additional dilution results are summarized in the correlation plot shown in Figure 6.4. The samples were a collection of diluted specimens and whole blood specimens from multiple draws. The R value of the linear fit is 0.91, indicating excellent agreement between the two systems.

Section 6.4: Discussion

6.4.1: Comparing ASAP and TEG

Figure 6.4 shows that the broad features of clot stiffness over time are identified by both the ASAP and TEG systems. Both produce the expected result for serial dilution of blood: the maximum clot stiffness decreases as the saline concentration increases (90). The TEG curves are essentially noiseless, while ASAP data show acceptable but noticeable noise. This comparison is misleading because the TEG software uses an unknown smoothing algorithm that is easily confounded by vibration or other physical disturbance. We have elected to report ASAP output in raw data format. The rotation period of the TEG instrument is about 10 seconds. The ASAP data are sampled at a rate of 1 Hz and assuming TEG samples once every half rotation or every 5 seconds, then significant smoothing of the ASAP curves should be possible while maintaining adequate time resolution. Finally, the clotting rate in the ASAP system is considerably faster than in the TEG system. The faster clotting rate could have numerous causes, shear from the posts, differences in the scale of the measurement (micro vs. macro), and or differences in the surface to volume ratio of the between the sample chamber in the two devices. Surfaces are well known to initiate the clotting cascade, even though the mechanism is not well understood (176). The two devices, ASAP and TEG, have a well-correlated measurement of stiffness ($r = 0.91$). This agreement is surprising: ASAPs are 2 μm in diameter and deflect on the order of 1-5 μm. At this scale ASAPs might well detect heterogeneities in fibrin cross-linking density or platelet concentration. We hypothesize that ASAP measurement correlates with the bulk measurement because of the large number of posts over which the measurement is performed, since a 1 mm^2 patch of posts has roughly 14,000 posts. To provide a context for relative length scales in the ASAP system, we show an SEM image of a clot formed around the posts in Figure 6.5. TEG has a well known dependence on hematocrit, as the red blood cell concentration increases the clot stiffness decreases (19; 12). While the ASAP system correlates well with TEG in this dilution study, it is conceivable that because of the micro-structure of the device the hematocrit dependence would differ between the devices.

6.4.2: Applications of ASAP elastometry

In Figure 6.6 A, we can see that the transmitted intensity is not constant during the entire experiment. This is most likely caused by platelet aggregation and scattering caused by the blood fibers. Transmitted light intensity has often been used as a method of measuring both platelet aggregation (96) and fiber formation (120). In part Figure 6.6 B, you can see that the increase in intensity comes just before the increase in force. This makes sense as ASAP posts are most likely interacting with the clot fibers. The platelet aggregation

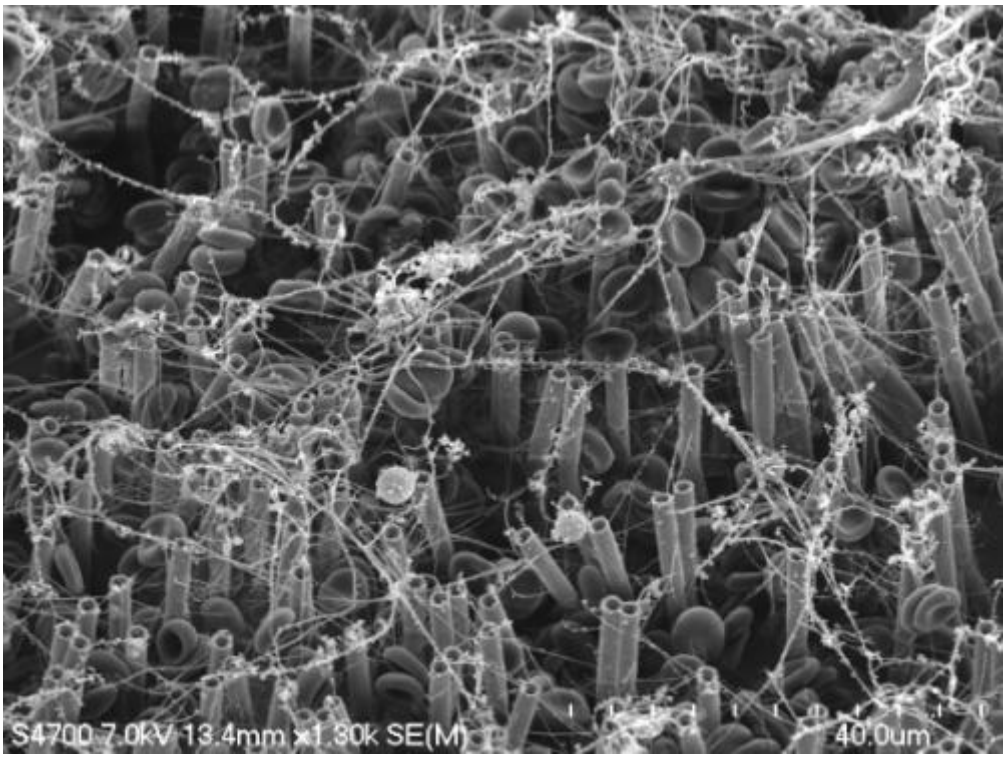

Figure 6.5: Scanning electron micro-graph (SEM) of a clot formed on the ASAP posts. The long strands are fibrin and biconcave discs are red blood cells. The fact that all the key products of clot formation are visible on the posts supports the notion that ASAP and TEG systems are measuring fundamentally similar phenomena, despite their differences in geometry and length scales.

that proceeds the clot formation does not change the resistance of the blood. Future work on the ASAP arrays could use the combined signals of light intensity and force to get better separation between clotting disorders that occur due to platelet malfunction, or poor fibrin formation.

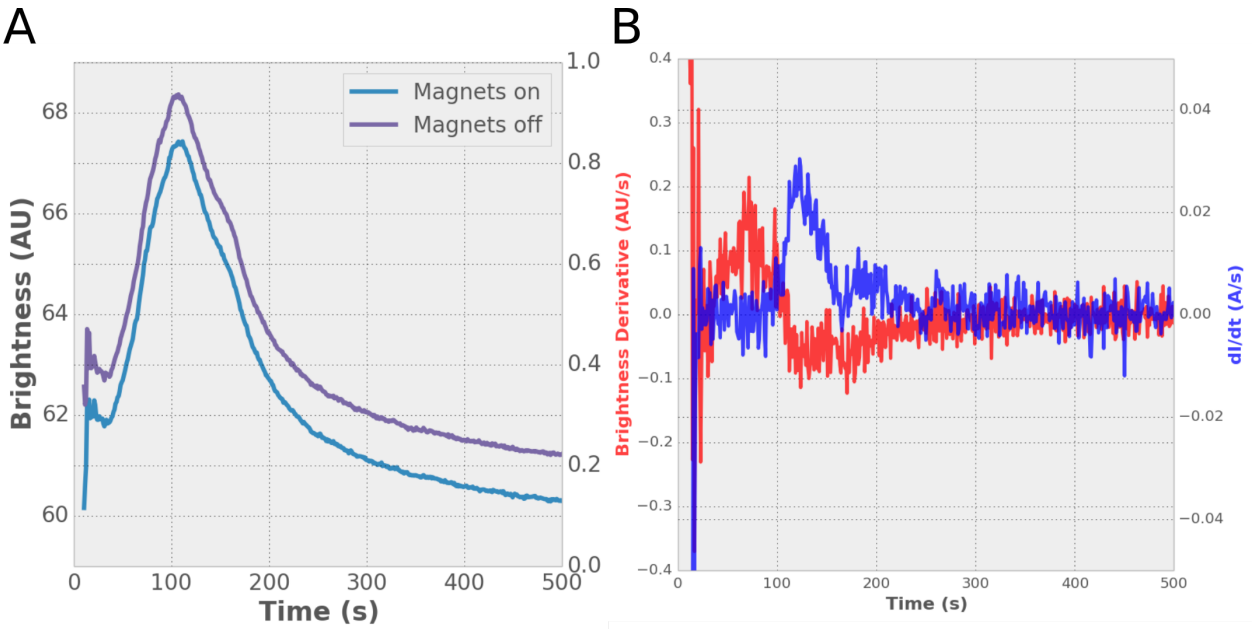

Figure 6.6: A) Plot of the intensity as a function of time with the magnetics on and the magnets off for a single experiment. As platelets aggregate the brightness transmitted through the sample increases and begins to decrease during the fiber formation. B) Plot of the rate in change in the brightness vs the rate in change of the applied current, magnetic field, to the ASAP arrays. You can see that the large increase in brightness precedes the force rapidly increases.

Section 6.5: Conclusions and future work

We have demonstrated the design and use of a post-array elastometer that operates on micro-liter quantities of blood. The postsâĂŹ behavior under an applied magnetic field could be described by our magneto-mechanical modeling. We demonstrated that the ASAP posts measured the elasticity of a blood clot over time, and that the maximum amplitude correlated well with a commercial blood elastomer (TEG). We also showed demonstration curves that indicate that clot lysis and clotting kinetics could be measured on the ASAP arrays. The ASAP array system uses dramatically less blood, 20 μL vs. 360 μL per test, making the system applicable for small animal studies, where conventional blood elastometry is currently impractical, such as experiments that require multiple tests and time course studies in mice. The ASAP device has the potential to be made into a compact portable point of care device for trauma or critical care. Finally, the ASAP element of the device is currently mounted in a small micro-fluidic chamber that could easily be integrated into more complex micro-fluidic devices that perform sample preprocessing. Micro-fluidic devices

have had recent success in reducing volumes in numerous blood applications, such as devices that perform panels of tests (93), separate blood components (39; 30; 153; 119), or mimic blood vasculature for the study of thrombus formation (137; 95; 170; 118). The ASAP technology presented here could be combined with many of these technologies to perform panels of tests on a single device, and/or preprocessing of the blood sample prior to testing.

Additionally future work with the ASAP system may enable the system to be used as a platelet aggregometer and thrombo-elastograph simultaneously. The intensity signal (Figure 6.6) appears to be showing the onset of platelet aggregation. Additional experiments need to be performed, but it is a well known fact that as platelets aggregate, they increase the transmitted intensity of blood by reducing scattering which has been used in devices to measure platelet aggregation (96).

Platelet aggregation is mediated by shear and platelet aggregation in response to shear is currently being explored as another diagnostic of a persons' ability to form clots (96; 110) Using the same equation, equation 5.6 for the shear generated that was used in chapter 5, we can calculate the amount of shear that the ASAP system is capable of. Unfortunately, the shear rates of 1×10^3 1/s are a factor of four below the threshold of 4000 1/s required to to activate platelets (96). The shear rate depends linearly on the post aspect ratio and frequency, equation 5.6. Future work should focus on developing alternate posts that are capable of shear activating platelets. A single device and test that can accurately asses platelet functionality and clot strength independent of each other could improve the diagnosis of clotting disorders.

Cilia methods

Growing Primary Airway Cilia

Human bronchial epithelial cells (HBE), primary passage, acquired from the UNC Cystic Fibrosis Center Tissue Procurement and Cell Culture Core, were seeded on Collagen IV (Sigma C-7521) Millicells at a density of 1.2-2.4 million in 5 ml of BEGM media per 60 mm diameter Millicell. The media was replaced from the basal side of the cells three times a week. The primary cells were grown until they were confluent and were well-ciliated. Cells were washed with PBS every time the media was replaced to prevent mucus buildup.

Cilia Axoneme Isolation

Cells were harvested for cilia axonemes once the culture reached confluence and cells were well-ciliated, i.e. greater than 70% of cells being ciliated.

Two 60 mm Millicells were used in for a single extraction. Cell inserts were washed with room temperature sterile PBS twice. The PBS in each was allowed to sit on the cells for 5 minutes at 37 ℃, to help release the mucus. 1.5 mL of deciliation buffer (10 mM Tris, 50 mM NaCL, 10 mM CaCl2-H2O, 1mM EDTA, 7 mM BME, .1% Triton X-100, pH-7.5) was made with 8 μL of protease inhibitor cocktail (PIC) (Sigma-Aldrich P8340) to prevent axoneme degradation. 300 μL of deciliation buffer was added to each cell insert and the cells were rocked gently for 1 minute by hand. The deciliation buffer was removed and put into 1.5 mL centrifuge tubes, one insert per tube. The inserts were washed one more time with deciliation buffer. The centrifuge tubes were then spun at 500 RCF for 1 min to remove cellular debris. The supernatant was decanted into a new tube, and the pellet was discarded. The supernatant was spun at 12,000 RCF, at 4 ℃, to pellet the cilia axonemes. The supernatant was discarded and the pellet was resuspended in 500 μL of resuspension buffer (50 mM K-Cl, 20 mM Tris-HCl, 5 mM Mg-SO4, 0.05 mM EDTA, 1mM DTT pH-8). 8 μL of protease inhibitor cocktail (Sigma-Aldrich P8340) was added to the resuspension buffer to prevent axoneme degradation. 25 μL of 10% Triton X-100 was added to the resuspension buffer, and the axonemes were incubated on ice for 15 min.

The axoneme solution was split between three tubes: 10% went into a single tube to be used for protein determination, and the remaining solution was split between the last two tubes. All three tubes were centrifuged at 12,000 RCF for 5 minutes, and the supernatant was removed.

The protein determination tube was resuspended in 30 μL of 0.5% SDS Solution. The axonemes in SDS solution were then run through a Pierce BCA Protein Assay (Thermo Scientific) according to the kit instructions to determine the protein content of the extraction. A typical extraction yields a final protein concentration on the order of 50 $\mu g/mL$. The isolated axonemes were confirmed to be functional by mixing

the axoneme solution 1:1 with the reactivation buffer. The axonemes were then monitored under an optical microscope for beating and then discarded.

The remaining two samples were further processed to separate the microtubule doublets from the structure.

Micro-tubule Isolation

One of the remaining tubes was suspended in 100 μL/insert of resuspension buffer without PIC and the other second insert was resuspended in μL/insert of salt extraction buffer (.5 M K-Cl, 20 mM Tris-HCL, 5 mM Mg-SO_4, 0.05 mM EDTA, 10 mM ATP). The salt extraction buffer removed the outer dynein arm proteins (62). The samples were then held at 4 ℃for 30 minutes. Typically, the protein determination was run during this time. The tubes were then pelleted at 12,000 RCF for 5 min and the supernatant discarded. Samples used for a silver staining gel, were frozen at -80 ℃until ready to be used. Each pellet was resuspended in 50 μL/insert of resuspension buffer, and 50 μL/insert of reactivation buffer (400 mM potassium acetate, 20 mM Tris-HCl, 6 mM $MgSO_4$, 1mM DTT, 10 mM ATP, pH - 7.8). Trypsin was added to the insert in proportion to protein quantity. In a typical experiment the goal was to add trypsin to the solution at a 1:200, trypsin : axoneme ratio. This protocol is based off of the Summers and Gibbons sliding protocols. (164). After 30 minutes on ice, an equal amount of soybean trypsin inhibitor was added to stop cilia axoneme digestion. Axonemes were then ready to be imaged and analyzed.

AFM Sample Prep

1/2 by 1/2 cm mica squares were attached to glass slides. A fresh surface of mica was prepared by cleaving the top layer off using scotch tape. Slides were then coated with poly-L-lysine by adding 30 μL of 1 mg/mL poly-L-lysine and waiting 30 seconds and rinsing with water. The surface was dried using a nitrogen air stream. 20-30 μL of microtubule samples were placed the slide and allowed to settle for 1-5 minutes before rinsing off with deionized water. Sample were allowed to air dry before imaging.

Image Analysis

AFM images were analyzed for curvature using a three point method with coarse graining as previously described in (11). Images were subdivided into 1 by 1 μm squares. In each square, if there was an microtubule doublet, the average curvature over the area was taken by circumscribing a circle to three points on the microtubule. One point on the microtubule in the center of the square and the two ends where the microtubule intersected the boundaries of the square. Microtubules that crossed or intersected another microtubule in

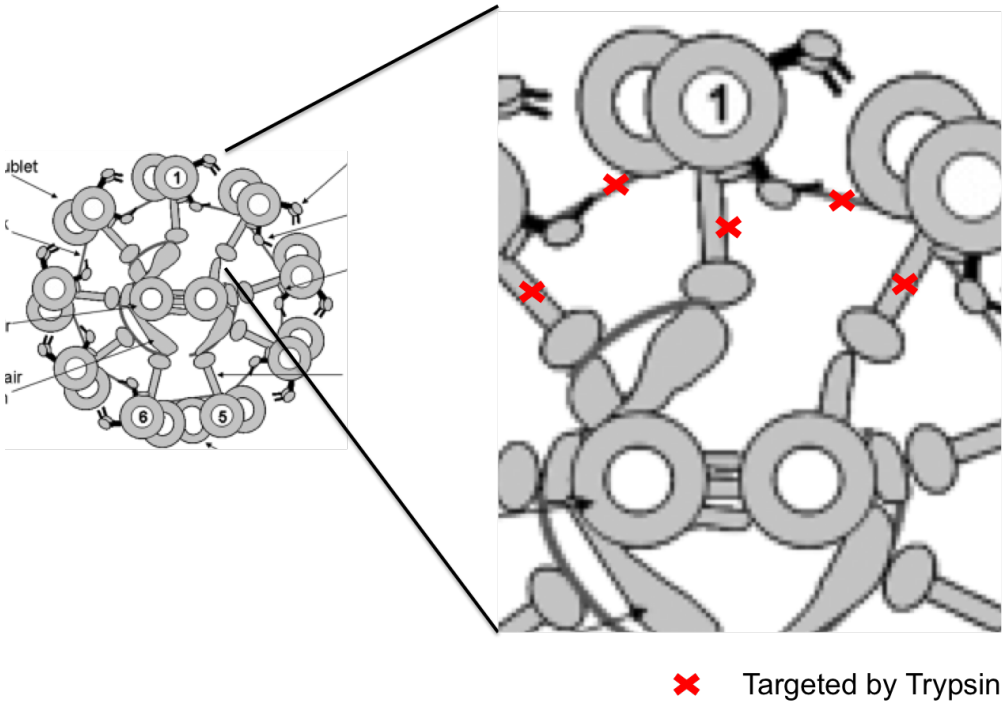

Figure 7: Diagram of a cross section of the cilia axoneme. A zoom in shows the protein targets of the trypsin. Trypsin preferentially attacks the radial spokes and nexin links between the microtubule doublets(164). Figure source (99)

the square region were not included. The data analysis was performed by hand, using a MATlab script to help with the data acquisition.

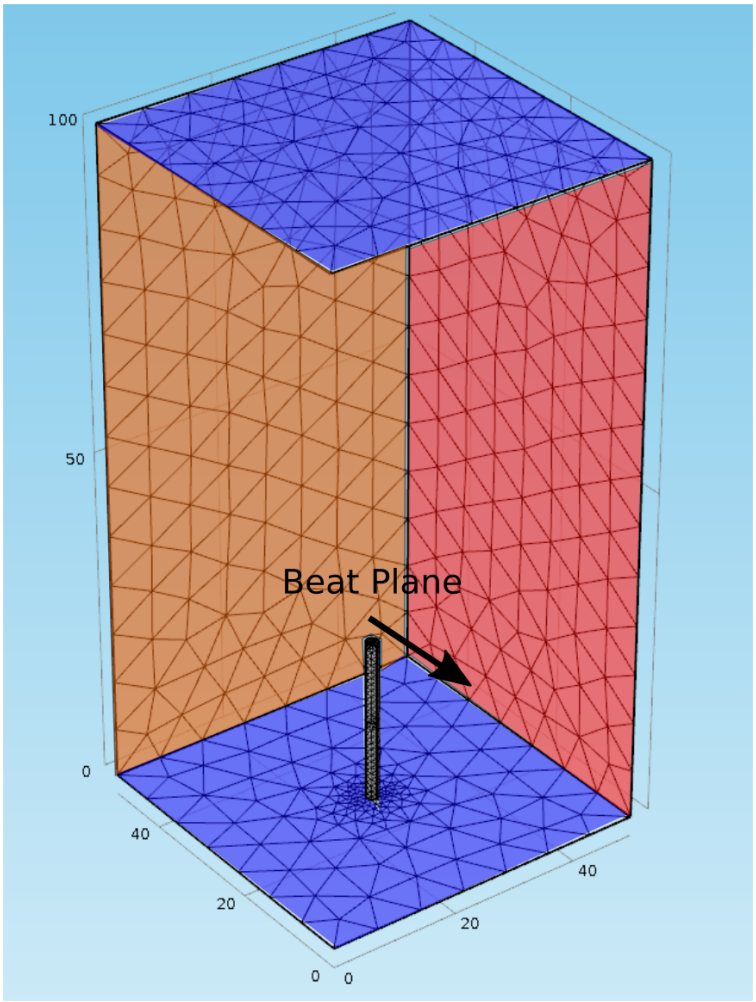

Figure 8: The COMSOL model showing the mesh and geometry of the COMSOL model. The model has no slip boundary conditions on the top and bottom, blue, while the left and right sides can have either no-slip or slip boundary conditions, red. The surfaces perpendicular to the plane of the post motion, orange, have zero pressure boundary condition.

The mesh was an automatically generated triangular mesh. The mesh size was reduced until further reductions of the mesh results in changes of the results of less than 1%. The maximum element size was 5.5 μm, while the minimum element size was 0.4 μm. The mesh was deformed with the post movement to maintain mesh quality and was smoothed using Hyper-elastic mesh smoothing.

The fluid structure interaction was solved using the direct fully-coupled PARDISO solver in COMSOL. Time stepping was performed using the backward differentiation formula (BDF) method with strict steps, and a maximum step size of 0.001 seconds. The boundary conditions on the posts were specified to be fluid structure interactions, with a fixed boundary condition on the base. The boundaries perpendicular to the plane of the post motion were 0 pressure, which allowed the post to generate flow. The top and bottom

of the channel were modeled as no-slip boundary conditions, while the sides of the channel (parallel to the plane of post motion) were, depending on the simulation modeled, as no-slip boundary conditions or slip boundary conditions. The slip boundary conditions in the plane of the post motion and the 0 pressure boundary conditions modeled an infinite array of posts.

Because of the scale of the system the fluid motion was calculated using the low Reynolds approximation to the Naiver Stokes equations, i.e. Stokes Flow. The solid mechanics equations used the quasi-static approximation because they were over four orders of magnitude smaller than the elastic and drag forces.

The elastic portion of the rod was modeled as an elastic material with an elastic modulus of 1.5 MPa and a Poisson ratio of .51. The nickel portion was modeled as an elastic material with an elastic modulus of 1GPa, and a Poisson ratio of .51. The magnetic force was modeled as a force couple applied at both ends of the nickel portion of the rod parallel to the end surface. The force couple varied sinusoidally according to the function:

$$F = \frac{F}{2} - \frac{F}{2}\cos(2\pi f t) \tag{1}$$

where F is the magnitude of the force couple, and f is the frequency of the driving force oscillation. The force was determined by calculation from the known applied field in our magnetic system, the length of the nickel shell and nickel volume using the magnetic model, eq. 4.18. The calculated force along with the PDMS properties gave deflections in the same range as our experiments.

REFERENCES

Abbott, J. J., Ergeneman, O., Kummer, M. P., Hirt, A. M., and Nelson, B. J. (2007). Modeling Magnetic Torque and Force for Controlled Manipulation of Soft-Magnetic Bodies. *IEEE Transactions on Robotics*, 23(6):1247–1252.

Afzelius, B. (2004). Cilia-related diseases. *The Journal of pathology*, 204(4):470–477.

Alexeev, A., Yeomans, J. M., and Balazs, A. C. (2008). Designing synthetic, pumping cilia that switch the flow direction in microchannels. *Langmuir*, 24(21):12102–12106.

Ansari, M. Z. and Cho, C. (2008). A Study on increasing sensitivity of rectangular microcantilevers used in biosensors. *Sensors*, 8(11):7530–7544.

Avron, J. E., Gat, O., and Kenneth, O. (2004). Optimal swimming at low reynolds numbers. *Physical Review Letters*, 93(18):1–4.

Ballard, M., Mills, Z. G., Beckworth, S., and Alexeev, A. (2014). Enhancing nanoparticle deposition using actuated synthetic cilia. *Microfluidics and Nanofluidics*, 17(2):317–324.

Bandyopadhyay, P. R. and Hansen, J. C. (2013). Breakup and then makeup: a predictive model of how cilia self-regulate hardness for posture control. *Scientific Reports*, pages 1–10.

BaÅ§kurt, O. K. (2003). Pathophysiological Significance of Blood Rheology. *Turkish Journal of Medical Sciences*, 33(6):347–355.

Belmiloud, N., Dufour, I., Colin, A., and Nicu, L. (2008). Rheological behavior probed by vibrating microcantilevers. *Applied Physics Letters*, 92(4):041907.

Bhattacharya, A., Buxton, G. a., Usta, O. B., and Balazs, A. C. (2012). Propulsion and trapping of microparticles by active cilia arrays. *Langmuir*, 28(6):3217–3226.

Bicek, A. D. A. A., Tüzel, E., Kroll, D. D. D. M., and Odde, D. J. D. D. (2007). Analysis of Microtubule Curvature. *Methods in cell biology*, 83:237–68.

Bochsen, L., Johansson, P. I., Kristensen, A. T., Daugaard, G., and Ostrowski, S. R. (2011). The influence of platelets, plasma and red blood cells on functional haemostatic assays. *Blood coagulation & fibrinolysis : an international journal in haemostasis and thrombosis*, 22(3):167–75.

Branscomb, J. and Alexeev, A. (2010). Designing ciliated surfaces that regulate deposition of solid particles. *Soft Matter*, 6(17):4066.

Brokaw, C. (1985). Computer Simulation of Flagellar Movement:: VI. Simple Curvature-Controlled Models Are Incompletely Specified. *Biophysical journal*, 48(October):633–642.

Brokaw, C. (2000). Stochastic simulation of processive and oscillatory sliding using a two-headed model for axonemal dynein. *Cell motility and the cytoskeleton*, 47(2):108–119.

Brokaw, C. (2005). Computer simulation of flagellar movement IX. Oscillation and symmetry breaking in a model for short flagella and nodal cilia. *Cell motility and the cytoskeleton*, 60(1):35–47.

Brokaw, C. C. J. (2001). Simulating the effects of fluid viscosity on the behaviour of sperm flagella. *Mathematical methods in the applied sciences*, 24(17-18):1351–1365.

Brokaw, C. J. (1975). Molecular mechanism for oscillation in flagella and muscle. *Proceedings of the National Academy of Sciences of the United States of America*, 72(8):3102–3106.

Brooks, A. C., Guillaumin, J., Cooper, E. S., and Couto, C. G. (2014). Effects of hematocrit and red blood cell-independent viscosity on canine thromboelastographic tracings. *Transfusion*, 54(3):727–34.

Brucker, C., Bauer, D., Chaves, H., Bruecker, C., and Brücker, C. (2007). Dynamic response of micro-pillar sensors measuring fluctuating wall-shear-stress. *Experiments in Fluids*, 42(5):737–749.

Brücker, C., Spatz, J., and Schröder, W. (2005). Feasability study of wall shear stress imaging using microstructured surfaces with flexible micropillars. *Experiments in Fluids*, 39(2):464–474.

Buchapudi, K. R., Huang, X., Yang, X., Ji, H.-F., and Thundat, T. (2011). Microcantilever biosensors for chemicals and bioorganisms. *The Analyst*, 136(8):1539–56.

Burgess, S. A., Walker, M. L., Sakakibara, H., Knight, P. J., and Oiwa, K. (2003). Dynein structure and power stroke. *Nature*, 421(6924):715–8.

Carroll, R. C., Craft, R. M., Langdon, R. J., Clanton, C. R., Snider, C. C., Wellons, D. D., Dakin, P. A., Lawson, C. M., Enderson, B. L., and Kurek, S. J. (2009). Early evaluation of acute traumatic coagulopathy by thrombelastography. *Transl Res*, 154(1):34–39.

Chen, C.-Y., Cheng, L.-Y., Hsu, C.-C., and Mani, K. (2015). Microscale flow propulsion through bioinspired and magnetically actuated artificial cilia. *Biomicrofluidics*, 9(3):034105.

Chen, C. Y., Lin, C. Y., and Hu, Y. T. (2014a). Inducing 3D vortical flow patterns with 2D asymmetric actuation of artificial cilia for high-performance active micromixing. *Experiments in Fluids*, 55(7):1–9.

Chen, Y., Li, P., Huang, P.-H., Xie, Y., Mai, J. D., Wang, L., Nguyen, N.-T., and Huang, T. J. (2014b). Rare cell isolation and analysis in microfluidics. *Lab on a chip*, pages 626–645.

Cheng-Yi Lin, Chia-Yun Chen, Ya-Ting Hu, and Chia-Yuan Chen (2013). Fluid dynamics analysis of magnetically actuated ciliated nano/micro structures for flow mixing and propulsion applications. In *The 8th Annual IEEE International Conference on Nano/Micro Engineered and Molecular Systems*, volume 1, pages 590–593.

Choi, S. and Park, J. K. (2010). Microfluidic rheometer for characterization of protein unfolding and aggregation in microflows. *Small*, 6(12):1306–1310.

Chung, K. H., Choi, Y. H., Yang, J.-H., Park, C. W., Kim, W.-J., Ah, C. S., and Sung, G. Y. (2012). Magnetically-actuated blood filter unit attachable to pre-made biochips. *Lab on a chip*, 12(18):3272–6.

Cindio, B. D., Gabriele, D., Catapano, G., Fata, P., and Hackel, R. (2007). The blood rheology in renal pathology. pages 156–163.

Costello, D. (1973). A new theory on the mechanics of ciliary and flagellar motility. II. Theoretical considerations. *The Biological bulletin*, 145(2):292–309.

Cribb, J. a., Meehan, T. D., Shah, S. M., Skinner, K., and Superfine, R. (2010). Cylinders vs. spheres: biofluid shear thinning in driven nanoparticle transport. *Annals of biomedical engineering*, 38(11):3311–22.

Critchfield, A. S., Yao, G., Jaishankar, A., Friedlander, R. S., Lieleg, O., Doyle, P. S., McKinley, G., House, M., and Ribbeck, K. (2013). Cervical mucus properties stratify risk for preterm birth. *PloS one*, 8(8):e69528.

Dagamseh, a. M. K., Bruinink, C. M., Wiegerink, R. J., Lammerink, T. S. J., Droogendijk, H., and Krijnen, G. J. M. (2013). Interfacing of differential-capacitive biomimetic hair flow-sensors for optimal sensitivity. *Journal of Micromechanics and Microengineering*, 23(3):035010.

Dagamseh, A. M. K., Wiegerink, R. J., Lammerink, T. S. J., and Krijnen, G. J. M. (2012). Towards a high-resolution flow camera using artificial hair sensor arrays for flow pattern observations. *Bioinspiration & biomimetics*, 7(4):046009.

DemiroÇğlu, H. (1997). The Importance of Erythrocyte Aggregation in Blood Rheology : Considerations on the Pathophysiology of Thrombotic Disorders. *Blood*.

DePuit, R. J. and Squires, T. M. (2012). Micro-macro-discrepancies in nonlinear microrheology: I. Quantifying mechanisms in a suspension of Brownian ellipsoids. *Journal of physics. Condensed matter : an Institute of Physics journal*, 24(46):464106.

Dimov, I. K., Basabe-Desmonts, L., Garcia-Cordero, J. L., Ross, B. M., Park, Y., Ricco, A. J., and Lee, L. P. (2011). Stand-alone self-powered integrated microfluidic blood analysis system (SIMBAS). *Lab on a chip*, 11(5):845–50.

Ding, Y., Nawroth, J., McFall-Ngai, M., and Kanso, E. (2013). Mixing and transport by ciliary carpets: a numerical study. *arXiv preprint arXiv:1312.2511*, (2007):1–16.

Downing, K. H. and Sui, H. (2007). Structural insights into microtubule doublet interactions in axonemes. *Current opinion in structural biology*, 17(2):253–9.

Dreyfus, R., Baudry, J., Roper, M. L., Fermigier, M., Stone, H. a., and Bibette, J. (2005). Microscopic artificial swimmers. *Nature*, 437(7060):862–865.

Du, P., Cheng, C., Lu, H., and Zhang, X. (2012). COMPLEX MODULUS OF PDMS AND ITS APPLICATION IN CELLULAR FORCE MEASUREMES. *rsc.org*, pages 674–676.

Espinosa-Garcia, J., Lauga, E., and Zenit, R. (2013). Fluid elasticity increases the locomotion of flexible swimmers. *Physics of Fluids*, 25(3):031701.

Evans, B. A. (2008). *Design , Fabrication , and Actuation of Biomimetic Cilia.* PhD thesis.

Evans, B. A., Shields, A. R., Carroll, R. L., Washburn, S., Falvo, M. R., and Superfine, R. (2007). Magnetically actuated nanorod arrays as biomimetic cilia. *Nano letters*, 7(5):1428–34.

Fahrni, F., Prins, M. W. J., and van Ijzendoorn, L. J. (2009). Micro-fluidic actuation using magnetic artificial cilia. *Lab on a chip*, 9(23):3413–3421.

Fiser, B., Shields, A., Michael, F., and Superfine, R. Highly responsive core-shell microactuator arrays for use in viscous and viscoelastic fluids. *Journal of Micromechanics and Microengineering*.

Fiser, B. L. (2012). *The Design , Fabrication , and Magnetic Actuation of a Microactuator to Accomplish Propulsion and Large Deflection in Viscous and Elastic Environments ().* Doctoral dissertation, University of North Carolina.

Fisher, J. K., Cribb, J., Desai, K. V., Vicci, L., Wilde, B., Keller, K., Taylor, R. M., Haase, J., Bloom, K., O'Brien, E. T., and Superfine, R. (2006). Thin-foil magnetic force system for high-numerical-aperture microscopy. *The Review of scientific instruments*, 77(2):nihms8302.

Fuard, D., Tzvetkova-Chevolleau, T., Decossas, S., Tracqui, P., and Schiavone, P. (2008). Optimization of poly-di-methyl-siloxane (PDMS) substrates for studying cellular adhesion and motility. *Microelectronic Engineering*, 85(5-6):1289–1293.

Furst, E. M., Suzuki, C., Fermigier, M., and Gast, A. P. (1998). Permanently-linked monodisperse paramagnetic chains. *Langmuir*, 14(26):7334–7336.

Furuhashi, M., Ura, N., Hasegawa, K., Yoshida, H., Tsuchihashi, K., Miura, T., and Shimamoto, K. (2002). Sonoclot coagulation analysis: new bedside monitoring for determination of the appropriate heparin dose during haemodialysis. *Nephrology, dialysis, transplantation : official publication of the European Dialysis and Transplant Association - European Renal Association*, 17(8):1457–62.

Gagnon, C., White, D., Cosson, J., Huitorel, P., Eddé, B., Desbruyères, E., Paturle-Lafanechère, L., Multigner, L., Job, D., and Cibert, C. (1996). The polyglutamylated lateral chain of alpha-tubulin plays a key role in flagellar motility. *Journal of cell science*, 109 (Pt 6:1545–53.

Ghosh, R., Buxton, G. a., Usta, O. B., Balazs, A. C., and Alexeev, A. (2010). Designing oscillating cilia that capture or release microscopic particles. *Langmuir*, 26(4):2963–2968.

Gibbons, I. R. (1981). Cilia and flagella of eukaryotes. *The Journal of cell biology*, 91(3 Pt 2):107s–124s.

Gnanamanickam, E. P., Nottebrock, B., Große, S., Sullivan, J. P., and Schröder, W. (2013). Measurement of turbulent wall shear-stress using micro-pillars. *Measurement Science and Technology*, 24:124002.

Godin, M., Tabard-Cossa, V., Miyahara, Y., Monga, T., Williams, P. J., Beaulieu, L. Y., Bruce Lennox, R., and Grutter, P. (2010). Cantilever-based sensing: the origin of surface stress and optimization strategies. *Nanotechnology*, 21(7):75501.

Grosse, S., Schroder, W., and Brucker, C. (2006). Nano-newton drag sensor based on flexible micro-pillars. *Measurement Science & Technology*, 17(10):2689–2697.

Große, S., Soodt, T., and Schröder, W. (2008). Dynamic calibration technique for the micro-pillar shear-stress sensor MPS 3. *Measurement Science and Technology*, 19(10):105201.

Hamasaki, T., Holwill, M. E., Barkalow, K., and Satir, P. (1995). Mechanochemical aspects of axonemal dynein activity studied by in vitro microtubule translocation. *Biophysical journal*, 69(6):2569–79.

Hard, R., Blaustein, K., and Scarcello, L. (1992). Reactivation of outer-arm-depleted lung axonemes: evidence for functional differences between inner and outer dynein arms in situ. *Cell motility and the cytoskeleton*, 21(3):199–209.

Hastie, a. T., Dicker, D. T., Hingley, S. T., Kueppers, F., Higgins, M. L., and Weinbaum, G. (1986). Isolation of cilia from porcine tracheal epithelium and extraction of dynein arms. *Cell motility and the cytoskeleton*, 6(1):25–34.

Hawkins, T., Mirigian, M., Selcuk Yasar, M., and Ross, J. L. (2010). Mechanics of microtubules. *Journal of biomechanics*, 43(1):23–30.

Heintz, N., Omran, H., and Ibanez-Tallon, I. (2003). To beat or not to beat: roles of cilia in development and disease. *Human Molecular Genetics*, 12(90001):27R–35.

Herzog, H., Klein, A., Bleckmann, H., Holik, P., Schmitz, S., Siebke, G., Tätzner, S., Lacher, M., and Steltenkamp, S. (2015). ¡i¿μ¡/i¿ -biomimetic flow-sensorsâĂŤintroducing light-guiding PDMS structures into MEMS. *Bioinspiration & Biomimetics*, 10(3):36001.

Heuser, T., Raytchev, M., Krell, J., Porter, M. E., and Nicastro, D. (2009). The dynein regulatory complex is the nexin link and a major regulatory node in cilia and flagella. *The Journal of cell biology*, 187(6):921–33.

Hilfinger, a. and Jülicher, F. (2008). The chirality of ciliary beats. *Physical biology*, 5(1):016003.

Hill, D. B., Swaminathan, V., Estes, A., Cribb, J., Brien, E. T. O., Davis, W., Superfine, R., O'Brien, E. T., and Davis, C. W. (2010). Force generation and dynamics of individual cilia under external loading. *Biophysical journal*, 98(1):57–66.

Hinchcliffe, E. H. and Linck, R. W. (1998). Two proteins isolated from sea urchin sperm flagella: structural components common to the stable microtubules of axonemes and centrioles. *Journal of cell science*, 111 (Pt 5:585–95.

Hines, M. and Blum, J. J. (1984). On the contribution of moment-bearing links to bending and twisting in a three-dimensional sliding filament model. *Biophysical journal*, 46(5):559–565.

Holcomb-Wygle, D. L., Schmitz, K. a., and Lindemann, C. B. (1999). Flagellar arrest behavior predicted by the Geometric Clutch model is confirmed experimentally by micromanipulation experiments on reactivated bull sperm. *Cell motility and the cytoskeleton*, 44(3):177–89.

Höök, P. and Vallee, R. B. (2006). The dynein family at a glance. *Journal of cell science*, 119(Pt 21):4369–71.

Hussong, J., Schorr, N., Belardi, J., Prucker, O., Rühe, J., and Westerweel, J. (2011). Experimental investigation of the flow induced by artificial cilia. *Lab on a chip*, 11(12):2017–2022.

Johansson, P. I., Stissing, T., Bochsen, L., and Ostrowski, S. R. (2009). Thrombelastography and tromboelastometry in assessing coagulopathy in trauma. *Scand J Trauma Resusc Emerg Med*, 17:45.

Judith, R. M., Fisher, J. K., Spero, R. C., Fiser, B. L., Turner, A., Oberhardt, B., Taylor, R. M., Falvo, M. R., and Superfine, R. (2015). Micro-elastometry on whole blood clots using actuated surface-attached posts (ASAPs). *Lab Chip*, 15(5):1385–93.

Judy, J. and Muller, R. (1997). Magnetically actuated, addressable microstructures. *Journal of Microelectromechanical Systems*, 6(3):249–256.

Judy, J. W., Muller, R. S., and Zappe, H. H. (1995). Magnetic microactuation of polysilicon flexure structures. *Journal of Microelectromechanical Systems*, 4(4):162–169.

Jun Kang, Y., Lee, S.-J. J., and Kang, Y. J. (2013). Blood viscoelasticity measurement using steady and transient flow controls of blood in a microfluidic analogue of Wheastone-bridge channel. *Biomicrofluidics*, 7(5):54122.

Kalwarczyk, T., ZiÈľbacz, N., Bielejewska, A., Zaboklicka, E., Koynov, K., SzymaÅĎski, J., Wilk, A., Patkowski, A., GapiÅĎski, J., Butt, H. J., and HoÅĆyst, R. (2011). Comparative analysis of viscosity of complex liquids and cytoplasm of mammalian cells at the nanoscale. *Nano Letters*, 11(5):2157–2163.

Kashuk, J. L., Moore, E. E., Sabel, A., Barnett, C., Haenel, J., Le, T., Pezold, M., Lawrence, J., Biffl, W. L., Cothren, C. C., and Johnson, J. L. (2009). Rapid thrombelastography (r-TEG) identifies hypercoagulability and predicts thromboembolic events in surgical patients. *Surgery*, 146(4):764–72; discussion 772–4.

Keller, J. B. and Rubinow, S. I. (1976). Slender-body theory for slow viscous flow. *Journal of Fluid Mechanics*, 75(04):705.

Khaderi, S. N., Den Toonder, J. M. J., and Onck, P. R. (2012). Magnetically actuated artificial cilia: The effect of fluid inertia. *Langmuir*, 28(20):7921–7937.

Khatavkar, V. V., Anderson, P. D., den Toonder, J. M. J., and Meijer, H. E. H. (2007). Active micromixer based on artificial cilia. *Physics of Fluids*, 19(8).

King, S. M. (2010). Axonemal dyneins winch the cilium. *Nature structural & molecular biology*, 17(6):673–4.

Kokot, G., Vilfan, M., Osterman, N., Vilfan, A., Kavčič, B., Poberaj, I., and Babič, D. (2011). Measurement of fluid flow generated by artificial cilia. *Biomicrofluidics*, 5(3):244–258.

Kollmannsberger, P. and Fabry, B. (2011). Linear and Nonlinear Rheology of Living Cells. *Annual Review of Materials Research*, 41(1):75–97.

Krijnen, G., Lammerink, T., Wiegerink, R., and Casas, J. (2007). Cricket Inspired Flow-Sensor Arrays. *2007 IEEE Sensors*, pages 539–546.

Kuntner, J., Stangl, G., and Jakoby, B. (2005). Characterizing the rheological behavior of oil-based liquids: Microacoustic sensors versus rotational viscometers. *IEEE Sensors Journal*, 5(5):850–856.

Lai, S., Wang, Y., Wirtz, D., and Hanes, J. (2009). Micro-and macrorheology of mucus. *Advanced drug delivery reviews*, 61(2):86–100.

Larsen, O. H., Fenger-Eriksen, C., Christiansen, K., Ingerslev, J., Sørensen, B., and Sorensen, B. (2011). Diagnostic performance and therapeutic consequence of thromboelastometry activated by kaolin versus a panel of specific reagents. *Anesthesiology*, 115(2):294–302.

Lauga, E. and Powers, T. R. (2009). The hydrodynamics of swimming microorganisms. *Reports on Progress in Physics*, 72(9):096601.

Lechtreck, K. F. and Witman, G. B. (2007). Chlamydomonas reinhardtii hydin is a central pair protein required for flagellar motility. *Journal of Cell Biology*, 176(4):473–482.

Lee, B. S., Lee, Y. U., Kim, H.-S., Kim, T.-H., Park, J., Lee, J.-G., Kim, J., Kim, H., Lee, W. G., and Cho, Y.-K. (2011). Fully integrated lab-on-a-disc for simultaneous analysis of biochemistry and immunoassay from whole blood. *Lab on a chip*, 11(1):70–8.

Lemaire, E., Caillard, B., Youssry, M., and Dufour, I. (2013). High-frequency viscoelastic measurements of fluids based on microcantilever sensing: New modeling and experimental issues. *Sensors and Actuators a-Physical*, 201:230–240.

Li, M., Hotaling, N. a., Ku, D. N., and Forest, C. R. (2014). Microfluidic thrombosis under multiple shear rates and antiplatelet therapy doses. *PloS one*, 9(1):e82493.

Li, M., Ku, D. N., and Forest, C. R. (2012). Microfluidic system for simultaneous optical measurement of platelet aggregation at multiple shear rates in whole blood. *Lab on a chip*, 12(7):1355–62.

Lindemann, C. (2011). Experimental Evidence for the Geometric Clutch Hypothesis. *Current topics in developmental biology*, 95:1–31.

Lindemann, C. B. (2002). Geometric Clutch model version 3: the role of the inner and outer arm dyneins in the ciliary beat. *Cell motility and the cytoskeleton*, 52(4):242–54.

Lindemann, C. B. (2007). The geometric clutch as a working hypothesis for future research on cilia and flagella. *Annals of the New York Academy of Sciences*, 1101:477–93.

Lindemann, C. B. and Lesich, K. a. (2010). Flagellar and ciliary beating: the proven and the possible. *Journal of cell science*, 123(Pt 4):519–28.

Lisicki, M. (2013). Four approaches to hydrodynamic Green's functions – the Oseen tensors. *arXiv.org*, (7):5.

Liu, C. (1998). Development of surface micromachined magnetic actuators using electroplated permalloy. *Mechatronics*, 8(5):613–633.

Liu, F., Ramachandran, D., and Urban, M. W. (2010). Colloidal films that mimic cilia. *Advanced Functional Materials*, 20(18):3163–3167.

Lokanathan, A. R., Nykänen, A., Seitsonen, J., Johansson, L. S., Campbell, J., Rojas, O. J., Ikkala, O., and Laine, J. (2013). Cilia-mimetic hairy surfaces based on end-immobilized nanocellulose colloidal rods. *Biomacromolecules*, 14(8):2807–2813.

Lukens, S., Yang, X., and Fauci, L. (2010). Using Lagrangian coherent structures to analyze fluid mixing by cilia. *Chaos*, 20(1).

Martini, W. Z., Cortez, D. S., Dubick, M. A., Park, M. S., and Holcomb, J. B. (2008). Thrombelastography is better than PT, aPTT, and activated clotting time in detecting clinically relevant clotting abnormalities after hypothermia, hemorrhagic shock and resuscitation in pigs. *J Trauma*, 65(3):535–543.

Masoud, H. and Alexeev, A. (2011a). Harnessing synthetic cilia to regulate motion of microparticles. *Soft Matter*, 7(19):8702.

Masoud, H. and Alexeev, A. (2011b). Harnessing synthetic cilia to regulate motion of microparticles. *Soft Matter*, 7(19):8702.

Mauldin, F. W., Viola, F., Hamer, T. C., Ahmed, E. M., Crawford, S. B., Haverstick, D. M., Lawrence, M. B., and Walker, W. F. (2010). Adaptive force sonorheometry for assessment of whole blood coagulation. *Clinica chimica acta; international journal of clinical chemistry*, 411(9-10):638–44.

Michelson, A. D. (2004). Platelet function testing in cardiovascular diseases. *Circulation*, 110(19):E489–E493.

Miki-Noumura, T. (1979). Conformational change in the outer doublet microtubules from sea urchin sperm flagella. *The Journal of Cell Biology*, 81(2):355–360.

Miki-Noumura, T. and Kamiya, R. (1976). Shape of microtubules in solutions. *Experimental Cell Research*, 97(2):451–453.

Mirkhalaf, M., Dastjerdi, a. K., and Barthelat, F. (2014). Overcoming the brittleness of glass through bio-inspiration and micro-architecture. *Nature communications*, 5:3166.

Mitchell, D. R. (2007). The evolution of eukaryotic cilia and flagella as motile and sensory organelles. *Advances in experimental medicine and biology*, 607:130–40.

Mitran, S. M. (2007). Metachronal wave formation in a model of pulmonary cilia. *Computers & structures*, 85(11-14):763–774.

Moulin, A., O'Shea, S., and Welland, M. (2000). Microcantilever-based biosensors. *Ultramicroscopy*, 82(1-4):23–31.

Moulin, A. M., O'Shea, S. J., Badley, R. A., Doyle, P., and Welland, M. E. (1999). Measuring Surface-Induced Conformational Changes in Proteins. *Langmuir*, 15(26):8776–8779.

Muthard, R. W. and Diamond, S. L. (2013). Side view thrombosis microfluidic device with controllable wall shear rate and transthrombus pressure gradient. *Lab on a chip*, 13(10):1883–91.

Nam, J., Lim, H., Kim, D., Jung, H., and Shin, S. (2012). Continuous separation of microparticles in a microfluidic channel via the elasto-inertial effect of non-Newtonian fluid. *Lab on a chip*, 12(7):1347–54.

Neeves, K. B., Onasoga, A. a., and Wufsus, A. R. (2013). The use of microfluidics in hemostasis: clinical diagnostics and biomimetic models of vascular injury. *Current opinion in hematology*, 20(5):417–23.

Nguyen, H., Cortez, R., and Fauci, L. (2014). Computing Flows Around Microorganisms: Slender-Body Theory and Beyond. *The American Mathematical Monthly*, 121(9):810–823.

Nguyen, N.-T. and Wu, Z. (2005). MicromixersâĂŤa review. *Journal of Micromechanics and Microengineering*, 15(2):R1–R16.

Nguyen, N.-T., Yap, Y.-F., and Sumargo, A. (2008). Microfluidic rheometer based on hydrodynamic focusing. *Measurement Science and Technology*, 19(8):085405.

Nicastro, D., McIntosh, J. R., and Baumeister, W. (2005). 3D structure of eukaryotic flagella in a quiescent state revealed by cryo-electron tomography. *Proceedings of the National Academy of Sciences of the United States of America*, 102(44):15889–94.

Nicastro, D., Schwartz, C., Pierson, J., Gaudette, R., Porter, M. E. M., and McIntosh, J. R. (2006). The molecular architecture of axonemes revealed by cryoelectron tomography. *Science*, 313(5789):944–8.

Omoto, C. K. and Kung, C. (1980). Rotation and twist of the central-pair microtubules in the cilia of Paramecium. *Journal of Cell Biology*, 87(41):33–46.

Ostrowski, S. R., Sorensen, A. M., Larsen, C. F., and Johansson, P. I. (2011). Thrombelastography and biomarker profiles in acute coagulopathy of trauma: a prospective study. *Scand J Trauma Resusc Emerg Med*, 19:64.

Parcell, J., Aydemir, N., Devaraj, H., Travas-Sejdic, J., Williams, D. E., and Aw, K. C. (2013). A novel air flow sensor from printed PEDOT micro-hairs. *Smart Materials and Structures*, 22(11):112001.

Person, C., Affairs, R., and Gmbh, T. I. (2011). Rotem FDA Aproval. Technical report.

Pigino, G., Bui, K. H., Maheshwari, A., Lupetti, P., Diener, D., and Ishikawa, T. (2011). Cryoelectron tomography of radial spokes in cilia and flagella. *The Journal of cell biology*, 195(4):673–87.

Pipe, C. J. and McKinley, G. H. (2009). Microfluidic rheometry. *Mechanics Research Communications*, 36:110–120.

Purcell, E, M. (1977). Life at Low Reynolds Number. 45(June 1976):3–11.

Rahbar, M., Tseng, H. Y., and Gray, B. L. (2014). High-aspect ratio magnetic nanocomposite polymer cilium. 8976:89760D.

Raiteri, R. and Butt, H.-J. (1995). Measuring Electrochemically Induced Surface Stress with an Atomic Force Microscope. *The Journal of Physical Chemistry*, 99(43):15728–15732.

Raiteri, R., Grattarola, M., Butt, H.-J., and Skládal, P. (2001). Micromechanical cantilever-based biosensors. *Sensors and Actuators B: Chemical*, 79(2-3):115–126.

Roca-Cusachs, P., Rico, F., Martínez, E., Toset, J., Farré, R., and Navajas, D. (2005). Stability of microfabricated high aspect ratio structures in poly(dimethylsiloxane). *Langmuir : the ACS journal of surfaces and colloids*, 21(12):5542–8.

Runyon, M. K., Johnson-Kerner, B. L., and Ismagilov, R. F. (2004). Minimal functional model of hemostasis in a biomimetic microfluidic system. *Angewandte Chemie (International ed. in English)*, 43(12):1531–6.

Sader, J. J. (1998). Frequency response of cantilever beams immersed in viscous fluids with applications to the atomic force microscope. *Journal of Applied Physics*, 84(July):64.

Satir, P. (1965). STUDIES ON CILIA : II. Examination of the Distal Region of the Ciliary Shaft and the Role of the Filaments in Motility. *The Journal of cell biology*, 26(3):805–34.

Satir, P. (2012). The new biology of cilia: Review and annotation of a symposium. *Developmental dynamics : an official publication of the American Association of Anatomists*, 241(2):426–30.

Satir, P. and Christensen, S. T. (2007). Overview of structure and function of mammalian cilia. *Annual review of physiology*, 69:377–400.

Satir, P. and Christensen, S. T. (2008). Structure and function of mammalian cilia. *Histochemistry and cell biology*, 129(6):687–93.

Schmitz, K. a., Holcomb-Wygle, D. L., Oberski, D. J., and Lindemann, C. B. (2000). Measurement of the force produced by an intact bull sperm flagellum in isometric arrest and estimation of the dynein stall force. *Biophysical journal*, 79(1):468–78.

Schochl, H., Maegele, M., Solomon, C., Gorlinger, K., and Voelckel, W. (2012). Early and individualized goal-directed therapy for trauma-induced coagulopathy. *Scand J Trauma Resusc Emerg Med*, 20:15.

Schomburg, W. K., Fahrenberg, J., Maas, D., and R, R. (1993). Active valves and pumps for microfluidics. *Journal of Micromechanics and Microengineering*, 3:216–218.

Schurz, J. (1996). Rheology of synovial fluids and substitute polymers. *Journal Of Macromolecular Science-Pure And Applied Chemistry*, A33(9):1249–1262.

Sears, P. R., Thompson, K., Knowles, M. R., and Davis, C. W. (2013). Human airway ciliary dynamics. *American journal of physiology. Lung cellular and molecular physiology*, 304(3):L170–83.

Seetharam, R. N. and Satir, P. (2005). High speed sliding of axonemal microtubules produced by outer arm dynein. *Cell motility and the cytoskeleton*, 60(2):96–103.

Shapiro, O. H., Fernandez, V. I., Garren, M., Guasto, J. S., Debaillon-Vesque, F. P., Kramarsky-Winter, E., Vardi, A., and Stocker, R. (2014). Vortical ciliary flows actively enhance mass transport in reef corals. *Proceedings of the National Academy of Sciences*, 111(37):13391–13396.

Shields, A. (2010). *Biomimetic Cilia Arrays - Fabrication , Magnetic Actuation , and Driven Fluid Transport Phenomena by*. PhD thesis, University of North Carolina at Chapel Hill.

Shields, a. R., Fiser, B. L., Evans, B. a., Falvo, M. R., Washburn, S., and Superfine, R. (2010). Biomimetic cilia arrays generate simultaneous pumping and mixing regimes. *Proceedings of the National Academy of Sciences of the United States of America*, 107(36):15670–5.

Shields, C. L., Bianciotto, C. G., Jabbour, P., Griffin, G. C., Ramasubramanian, A., Rosenwasser, R., and Shields, J. a. (2011). Intra-arterial chemotherapy for retinoblastoma: report No. 2, treatment complications. *Archives of ophthalmology*, 129(11):1407–15.

Shim, J. S. and Ahn, C. H. (2012). An on-chip whole blood/plasma separator using hetero-packed beads at the inlet of a microchannel. *Lab on a chip*, 12(5):863–6.

Shingyoji, C., Higuchi, H., Yoshimura, M., Katayama, E., and Yanagida, T. (1998). Dynein arms are oscillating force generators. *Nature*, 393(6686):711–4.

Singh, H., Laibinis, P. E., and Hatton, T. A. (2005). Synthesis of flexible magnetic nanowires of permanently linked core-shell magnetic beads tethered to a glass surface patterned by microcontact printing. *Nano letters*, 5(11):2149–54.

Smith, D. J., Blake, J. R., and Gaffney, E. A. (2008a). Fluid mechanics of nodal flow due to embryonic primary cilia. *Journal of the Royal Society, Interface / the Royal Society*, 5(22):567–73.

Smith, D. J., Gaffney, E. a., and Blake, J. R. (2008b). Modelling mucociliary clearance. *Respiratory physiology & neurobiology*, 163(1-3):178–88.

Smith, D. J., Smith, a. a., and Blake, J. R. (2011). Mathematical embryology: The fluid mechanics of nodal cilia.

Spalding, G. J., Hartrumpf, M., Sierig, T., Oesberg, N., Kirschke, C. G., and Albes, J. M. (2007). Cost reduction of perioperative coagulation management in cardiac surgery: value of "bedside" thrombelastography (ROTEM). *Eur J Cardiothorac Surg*, 31(6):1052–1057.

Spiess, B. D., Gillies, B. S., Chandler, W., and Verrier, E. (1995). Changes in transfusion therapy and reexploration rate after institution of a blood management program in cardiac surgical patients. *J Cardiothorac Vasc Anesth*, 9(2):168–173.

Stachowiak, J. C., Yue, M., Castelino, K., Chakraborty, A., and Majumdar, A. (2006). Chemomechanics of surface stresses induced by DNA hybridization. *Langmuir : the ACS journal of surfaces and colloids*, 22(1):263–8.

Suh, J. W., Glander, S. F., Darling, R. B., Storment, C. W., and Kovacs, G. T. (1997). Organic thermal and electrostatic ciliary microactuator array for object manipulation. *Sensors and Actuators A: Physical*, 58(1):51–60.

Sui, H. and Downing, K. H. (2006). Molecular architecture of axonemal microtubule doublets revealed by cryo-electron tomography. *Nature*, 442(7101):475–8.

Summers, K. E. and Gibbons, I. R. (1973). Effects of trypsin digestion on flagellar structures and their relationship to motility. *The Journal of cell biology*, 58(3):618–29.

Takasaki, Y. and Miki-Noumura, T. (1982). Shape of the ciliary doublet microtubule in solution. *Journal of molecular biology*, 158(2):317–24.

Theusinger, O. M., Spahn, D. R., and Ganter, M. T. (2009). Transfusion in trauma: why and how should we change our current practice? *Curr Opin Anaesthesiol*, 22(2):305–312.

Toker, O. S., Karaman, S., Yuksel, F., Dogan, M., Kayacier, A., and Yilmaz, M. T. (2012). Temperature Dependency of Steady, Dynamic, and Creep-Recovery Rheological Properties of Ice Cream Mix. *Food and Bioprocess Technology*, 6(11):2974–2985.

Toonder, J. D., Bos, F., Broer, D., Filippini, L., Gillies, M., de Goede, J., Mol, T., Reijme, M., Talen, W., Wilderbeek, H., Khatavkar, V., and Anderson, P. (2008). Artificial cilia for active micro-fluidic mixing. *Lab on a chip*, 8(4):533–541.

Toonder, J. M. J. D. and Onck, P. R. (2013). Microfluidic manipulation with artificial/bioinspired cilia. *Trends in Biotechnology*, 31(2):85–91.

Tsai, M., Kita, A., Leach, J., Rounsevell, R., Huang, J. N., Moake, J., Ware, R. E., Fletcher, D. A., and Lam, W. A. (2012). In vitro modeling of the microvascular occlusion and thrombosis that occur in hematologic diseases using microfluidic technology. *The Journal of clinical investigation*, 122(1):408–18.

van Oosten, C. L., Bastiaansen, C. W. M., and Broer, D. J. (2009). Printed artificial cilia from liquid-crystal network actuators modularly driven by light. *Nature materials*, 8(8):677–682.

Vancura, C., Dufour, I., Heinrich, S. M., Josse, F., Hierlemann, A., and Vančura, C. (2008). Analysis of resonating microcantilevers operating in a viscous liquid environment. *Sensors and Actuators A: Physical*, 141(1):43–51.

Venier, P., Maggs, a. C., Carlier, M. F., and Pantaloni, D. (1994). Analysis of microtubule rigidity using hydrodynamic flow and thermal fluctuations. *The Journal of biological chemistry*, 269(18):13353–60.

Vilfan, M., Kokot, G., Vilfan, A., Osterman, N., Kavčič, B., Poberaj, I., and Babič, D. (2012). Analysis of fluid flow around a beating artificial cilium. *Beilstein Journal of Nanotechnology*, 3(1):163–171.

Vilfan, M., Potocnik, A., Kavcic, B., Osterman, N., Poberaj, I., Vilfan, A., and Babic, D. (2010). Self-assembled artificial cilia. *Proceedings of the National Academy of Sciences of the United States of America*, 107(5):1844–1847.

Vogler, E. and Siedlecki, C. (2009). Contact activation of blood-plasma coagulation. *Biomaterials*, 30(10):1857–1869.

Voleisis, a., Kazys, R., Mazeika, L., Sliteris, R., Voleisiene, B., and Grybauskas, P. (2002). Ultrasonic method for the whole blood coagulation analysis. *Ultrasonics*, 40(1-8):101–7.

Waigh, T. a. (2005). Microrheology of complex fluids. *Reports on Progress in Physics*, 68(3):685–742.

Wang, J. and Chen, Y. (2015). Oil âĂŞ water separation capability of superhydrophobic fabrics fabricated via combining polydopamine adhesion with lotus-leaf-like structure. 42614:1–6.

Wang, Y., Gao, Y., Wyss, H., Anderson, P., and den Toonder, J. (2013a). Out of the cleanroom, self-assembled magnetic artificial cilia. *Lab on a chip*, 13(17):3360–6.

Wang, Y., Gao, Y., Wyss, H. M., Anderson, P. D., and den Toonder, J. M. J. (2014). Artificial cilia fabricated using magnetic fiber drawing generate substantial fluid flow. *Microfluidics and Nanofluidics*, 18(2):167–174.

Wang, Y. Y., Lai, S. K., Ensign, L. M., Zhong, W., Cone, R., and Hanes, J. (2013b). The microstructure and bulk rheology of human cervicovaginal mucus are remarkably resistant to changes in pH. *Biomacromolecules*.

Wang, Z. (2011). Polydimethylsiloxane Mechanical Properties Measured by Macroscopic Compression and Nanoindentation Techniques. Technical report.

Ward, K. and Fan, Z. H. (2015). Mixing in microfluidic devices and enhancement methods. *Journal of Micromechanics and Microengineering*, 25(9):094001.

Wargo, M. J. and Smith, E. F. (2003). Asymmetry of the central apparatus defines the location of active microtubule sliding in Chlamydomonas flagella. *Proceedings of the National Academy of Sciences of the United States of America*, 100(1):137–42.

Weibel, D. and Whitesides, G. (2006). Applications of microfluidics in chemical biology. *Current Opinion in Chemical Biology*, 10(6):584–591.

Westbrook, A. J., Olsen, J., Bailey, M., Bates, J., Scully, M., and Salamonsen, R. F. (2009). Protocol based on thromboelastograph (TEG) out-performs physician preference using laboratory coagulation tests to guide blood replacement during and after cardiac surgery: a pilot study. *Heart Lung Circ*, 18(4):277–288.

Wiggins, C. H. and Goldstein, R. E. (1997). Flexive and Propulsive Dynamics of Elastica at Low Reynolds Numbers. 2(3):4.

Wiggins, C. H., Riveline, D., Ott, a., and Goldstein, R. E. (1998). Trapping and wiggling: elastohydrodynamics of driven microfilaments. *Biophysical journal*, 74(2 Pt 1):1043–1060.

Wirtz, D. (2009). Particle-tracking microrheology of living cells: principles and applications. *Annual review of biophysics*, 38:301–26.

Witman, G. B., Plummer, J., and Sander, G. (1978). Chlamydomonas flagellar mutants lacking radial spokes and central tubules. Structure, composition, and function of specific axonemal components. *Journal of Cell Biology*, 76(3):729–747.

Woolley, D. M. (2010). Flagellar oscillation: a commentary on proposed mechanisms. *Biological reviews of the Cambridge Philosophical Society*, 85(3):453–70.

Wu, G., Ji, H., Hansen, K., Thundat, T., Datar, R., Cote, R., Hagan, M. F., Chakraborty, a. K., and Majumdar, a. (2001). Origin of nanomechanical cantilever motion generated from biomolecular interactions. *Proceedings of the National Academy of Sciences of the United States of America*, 98(4):1560–4.

Wu, G., Krebs, C. R., Lin, F.-C. C., Wolberg, A. S., and Oldenburg, A. L. (2013). High sensitivity microelastometry: applications in blood coagulopathy. *Annals of biomedical engineering*, 41(10):2120–9.

Young, E. W. K. and Beebe, D. J. (2010). Fundamentals of microfluidic cell culture in controlled microenvironments. *Chemical Society Reviews*, 39(3):1036.

Zhang, D., Wang, W., Peng, F., Kou, J., Ni, Y., Lu, C., and Xu, Z. (2014). A bio-inspired inner-motile photocatalyst film: a magnetically actuated artificial cilia photocatalyst. *Nanoscale*, 6(10):5516–25.

Zhou, B., Xu, W., Syed, A. A., Chau, Y., Chen, L., Chew, B., Yassine, O., Wu, X., Gao, Y., Zhang, J., Xiao, X., Kosel, J., Zhang, X.-X., Yao, Z., and Wen, W. (2015). Design and fabrication of magnetically functionalized flexible micropillar arrays for rapid and controllable microfluidic mixing. *Lab on a chip*, 15(9):2125–32.

Zilz, J., Schäfer, C., Wagner, C., Poole, R. J., Alves, M. a., and Lindner, A. (2014). Serpentine channels: micro-rheometers for fluid relaxation times. *Lab on a chip*, 14(2):351–8.

Zobel, C. R. (1973). EFFECT OF SOLUTION COMPOSITION AND PROTEOLYSIS ON THE CONFORMATION OF AXONEMAL COMPONENTS. *The Journal of Cell Biology*, 59(3):573–594.